ABSTRACT

BOUFARSAN, MUNIRAH AHMED. Investigation of Proximity Coupled Patch Antenna with a Fixed Feed for Adaptable mm-Wave Antenna-in-Package Design. (Under the direction of Dr. Jacob J. Adams).

The mm-wave band (30 GHz - 300 GHz) provides larger bandwidths, has a smaller wavelength, and higher resolution compared to lower microwave and radio frequencies. Thus, it enables many applications such as wireless communication technologies, radar sensors, mm-wave imaging, and fifth-generation wireless telecommunication standard (5G). The large bandwidth provides better data transfer rates that make the mm-wave crucial for wireless communication technologies and the fifth-generation wireless telecommunication standard (5G).

However, the path loss is proportional to the carrier frequency square and is considerably higher at mm-wave frequencies. Nevertheless, the small wavelengths of mmWave frequencies enable large numbers of antenna elements to fit in the same space as a single microwave or RF antenna to provide high gains that can compensate for the isotropic path loss. Additionally, the small wavelength at these frequencies (10 mm to 1 mm) allows integration of integrated circuits (ICs) with antennas within a single package, as the antenna form-factor reduces.

Mm-wave antennas are application-specific because of their fractional bandwidth and polarization limitations comparing to their coupled ICs. Thus, the antennas need to be designed and modified based on the application requirements (operating frequency, bandwidth, gain, and polarization). A general-purpose IC that can be coupled easily to different antennas would be an ideal configuration to achieve low-cost and high-performance. We propose an antenna in package (AiP), where the antennas are fabricated as a separate component mounted on the package of fixed RFIC chip. This approach gives the flexibility to changing only the antenna lid for different

operating frequencies and polarization while using the same fixed feed line fabricated on the RFIC chip.

However, there are several challenges associated with implementing this proposed AiP. This dissertation studies the antenna's behavior when it is coupled to a fixed feed line and the limitations imposed on the antenna by the feed line's fixed dimensions frequency and polarization specifications. First, this work presents a simplified analysis that can be used to design such an antenna (in this case, a proximity coupled patch antenna). That provides quick estimates of its dimensions based on given specifications of frequency and polarization—followed by a study determining the antenna design's limitations imposed by the thin feed line's fixed dimensions on frequency, bandwidth, gain polarization specifications. Finally, we explore the ability and boundaries of integrating antenna array on a fixed package over a wide frequency band and desired polarization. These studies allow for optimizing the AiP from the first design step and better understand the implementation of embedded antennas mounted on top of a fixed RFIC chip to support the various antenna and package solutions.

Investigation of Proximity Coupled Patch Antenna with a Fixed Feed for Adaptable mm-Wave Antenna-in-Package Design

by
Munirah A A A A Boufarsan

A dissertation submitted to the Graduate Faculty of
North Carolina State University
in partial fulfillment of the
requirements for the degree of
Doctor of Philosophy

Electrical Engineering

Raleigh, North Carolina
2021

APPROVED BY:

Dr. Jacob J. Adams Chair of Advisory Committee	Dr. Brian A. Floyd
Dr. Paul D. Franzon	Dr. Muhammad Shahzad

DEDICATION

I dedicate this dissertation to my family. To my parents, who sported me and encouraged me to achieve my dream. Also, to my sisters and brother, who always supported me. And to my best friend "Dana," who always be in my side and draw the smile on my face.

BIOGRAPHY

Munirah Boufarsan was born in Kuwait. She received her bachelor's degree in Electronics and Communication Engineering from Kuwait University, Kuwait in 2005, and two master's degrees in RF and electronic engineering. One master's degree from Kuwait University, Kuwait, in 2009. Another master's degree from Carnegie Mellon University, Pittsburgh, PA, the USA, in 2014. She started her doctoral study at NC State University in August 2014.

She worked a full job as a teaching assistant at Kuwait University from December 2005 to February 2011.

Munirah's primary research of interest is the mm-wave antenna in package and patch antenna design.

ACKNOWLEDGMENTS

I would express my gratitude to my advisor, Prof. Jacob J. Adams, for giving me opportunities to grow and succeed and continually remind me that I have to finish and graduate. To push me to do research, ask questions, test my hypothesis with simple tests, and publish. For mentoring me when I got stuck in analysis and for providing resources on how to move forward. For wisdom on writing and anecdotes on success.

I sincerely express my gratitude to all of my committee members, Prof. Floyd, Prof. Franzon, and Prof. Ozturk, for their suggestions, which helped improve my research quality. I am also grateful to Prof. Shahzad for agreeing to be part of my committee.

My thanks to all my colleagues at the antenna and electromagnetics lab (AEL): Binbin Yang, Meng Wang, Clifford Muchler, Vivek Bharambe, Kurt Schab, Shruti Srivastava, Danyang Huang, Bill Zhou, Yongduk Oh, Joe Dusenbury, Matt Berry, Brandon Sluss, Jaewoo Kim, Neal Kordsmeier, thanks to all of you for being there and helping me with your inputs and comments on my research work.

My thanks to my special MRC friends: Dr. Deeksha Lal, Dr. Kirti, Dr. Vikas, Dr. Vishwa and Sandeep. Thanks to all of you for being supportive and helpful during my PhD. study period.

My thanks to my special friend in NC: Mariam Almutawa, Zainab Alnoamani, Dr. Sarah Rajab, Dr. Asmaa Alrshuad, Aisha Almathkor, Mariam Ameer, and Dr. Heba.

TABLE OF CONTENTS

LIST OF TABLES

LIST OF FIGURES

CHAPTER 1: Introduction

The millimeter-wave (mm-wave) spectrum, defined to be in the range of 30 GHz to 300 GHz, has attracted numerous applications such as wireless communication technologies, radar sensors, mm-wave imaging, and fifth-generation wireless telecommunication standard (5G) [1]-[15]. The mm-wave has a large bandwidth, a small wavelength, and higher resolution than lower microwave and radio frequencies.

Due to the abundance of available bandwidth in the mm-wave spectrum, this spectrum supports higher data rates. The large bandwidth gives better data transfer rates, enabling quickly about the order of several Gbps or more when using the microwave frequencies [16]. High data rates make high-quality video streaming, real-time gaming, and other bandwidth-intensive applications a reality. This advantage of mm-wave has significantly played a role in wireless communication technologies and fifth-generation wireless telecommunication standard (5G). Also, mm-wave can enable all-weather radar and sensing because of its unique characteristic that it penetrates through the fog, rain, and cloud.

Moreover, mm-wave has a small wavelength (1- 10 mm), so the components and the antennas at mm-wave are small. Thus, the integrated circuits (ICs) and the antennas can be integrated within a single package, reducing the chip's physical size and the antenna form-factor. Besides, the mm-waves effortlessly pass through common clothing materials and reflect from the body and any concealed items. This unique characteristic can be used in the imaging system where the reflected waves can be focused, and then the system will reveal the hidden object's size, shape, and orientation [17]. The mm-waves have a high resolution because it has a small wavelength (1 - 10 mm). Generally, the diffraction limits resolution to spot sizes of $\lambda/2$ or more extensive, but at millimeter wavelength, the resolution spot sizes less than 10 mm are easily achievable. Thus, the mm-wave helps imaging systems applications such as explosive detective and body scan at the airport [17].

Although the available bandwidth and mmWave frequencies' resolution is promising, the path loss at these frequencies is high. The path loss is proportional to the square of the link distance and carrier frequency. Thus, the mmWave spectrum has considerable path loss. Nevertheless, small wavelengths of mm-wave frequencies enable large numbers of antenna elements to be implemented in the same form factor to provide high gains that can compensate for the isotropic path loss. As a result, arrays are necessary to overcome a large amount of path loss and achieve the required gain essential for high data rates.

Because of the short wavelength at mmWave frequencies, antenna designs can be integrated with the ICs. Several approaches are used to combine mm-wave antennas with their IC components in a single package. Antenna-in-package (AiP) is one of the approaches where the antenna is fabricated as a separate component mounted on the package with an integrated mm-wave circuit. Packages with embedded antennas reduce the interconnect loss and prevent the requirement for developing the mm-wave interconnect and antenna solutions. Also, it gives the flexibility to fabricate the antenna on a low permittivity substrate [18], [19]. As a result, the AiP solution provides high radiation efficiency, making AiP a great solution to integrate the antenna with ICs within a single package.

One commonly used planar antenna suitable for AiP design is the electromagnetically coupled (EMC) microstrip antenna, also called proximity coupled patch antennas (PCPA). This antenna is popular for mm-wave applications because it does not require complicated fabrication processes and produces moderate gain at the broadside [21]. High-performing millimeter-wave devices require efficient low-profile antennas to ensure reliable and interference-free communications.

This dissertation aims to provide flexibility in various antenna requirements (operating frequency, bandwidth, directivity, and polarization) without making any changes in the designed chip (RFIC). We will use the AiP technique because the antenna is fabricated as a separate component mounted on the package. For example, **Figure** 1.1 shows an illustration of an AiP, where integrated proximity coupled patch antennas (PCPA) is added on the top of a fixed thin feed line that is fabricated on a standard packaging chip. Antenna 1 can be designed at operating frequency f_{o1}, and if design requirements change and a lower frequency of operation at f_{o2} are needed, it can be replaced by Antenna 2. In the same manner, antennas can also be designed for different polarization (circular or linear). Therefore, low-cost and high-performance mm-wave devices can be achieved. While using the same fixed feed line is fabricated on an RFIC chip for different operating frequencies and polarization by changing the antenna lid only. This is important for low-cost mm-wave applications where requirements of gain, bandwidth, polarization, and frequency can vary. However, fixing the feed line and only changing the antenna lid is challenging. In this dissertation, we study the limitations that we have faced during our investigation of changing the antenna lid and fixing the RFIC chip.

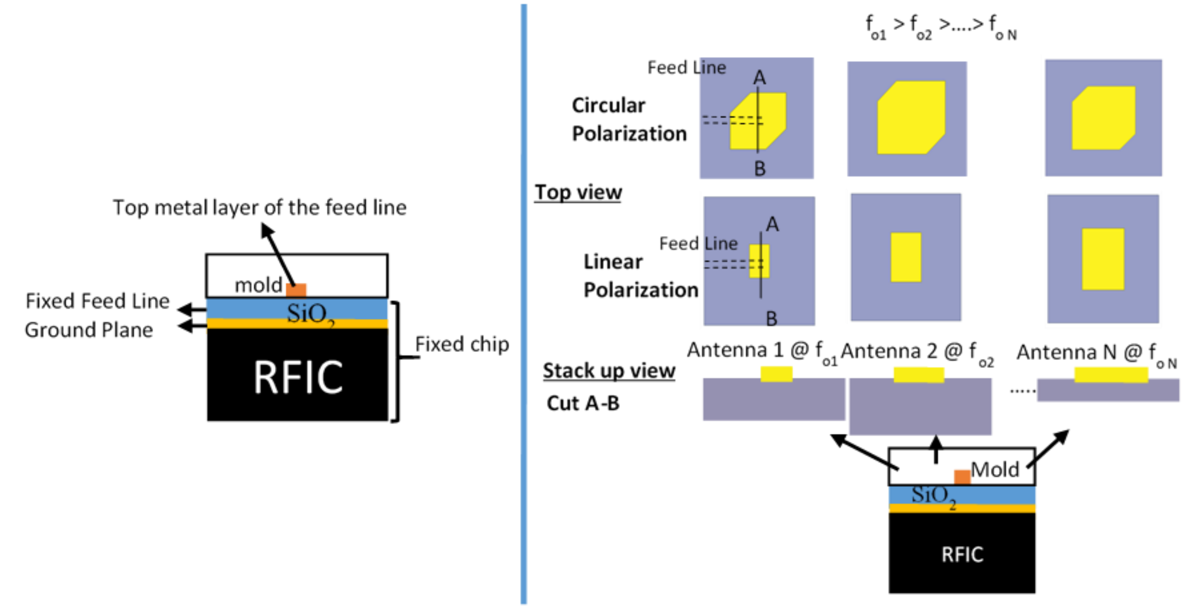

a. Stack up view of mm-wave antenna-in-package

b. Stack up view of lid antenna

Figure 1.1 Drawing illustrates the AiP technique and the proposed proximity coupled antenna.

To achieve our main target, we need to meet the following objectives:

Objective 1: Present a simplified analysis for adaptable PC patch antennas that can be used for the described AiP applications to estimate the dimension of the fixed feed antenna (width W, length L, and substrate height h) for a desired operating frequency and different polarization. This analysis provides quick estimates of the antenna dimensions required for resonant frequency and specific polarization and gives an intuitive understanding of the PCPA's behavior.

Objective 2: Determine the adaptable antenna design's limitations imposed by the thin feed line's fixed dimensions on frequency, bandwidth, gain, and polarization specifications.

Objective 3: Investigate the methods to overcome the limitations we have by coupling the adaptable PC patch antennas to the thin fixed feed line.

Objective 4: Clarify the ability and limitations of implementing an antenna array in a fixed package over the verity of operation frequencies and desired polarization (linear or circular).

This document is organized as the following:

Chapter 2 provides a brief overview of mm-wave applications and some techniques used to integrate the antennas with integrated circuits (ICs) such as AiP, antenna-on-chip, and antenna on board. This chapter also introduces some analysis models provided by researchers to study the EMC patch antenna. At the end of this chapter, a short overview of the mm-wave phased array is given.

Chapter 3 discusses the design and simulation results of a linearly polarized fixed-feed patch antenna at different operating frequencies. The dimensions of the antenna lid and substrate parameters are changed to study its effects on the design. This study allows us to predict the range of the operating frequencies achieved by coupling to the fixed feed line.

Chapter 4 studies a circularly polarized fixed-fed patch antenna at different designed frequencies. We investigate the ability of proximity coupled fixed thin fed line to various circularly polarized antennas operating at different frequencies. Also, we present the limitations of this antenna lid design fabricated on a fixed RFIC chip.

Chapter 5 investigates the effect of changing the feed line design on creating linear or circular polarization at various operating frequencies. We study the impact of changing the feed line design on the behavior of the antenna's dimensions at different operating frequencies and polarization. We then use this study's results to investigate if we can overcome the coupling patch antenna's limitations to a fixed feed line.

Chapter 6 proposes design considerations for circularly or linearly polarized phased antenna array elements using the fixed-feeding structure. We explore the ability to design linearly or circularly polarized phased array coupled to fixed feed lines fabricated on a fixed RFIC chip for different operating frequencies. We also study the beam steering's performance of the phased array coupled to a fixed feed line.

Chapter 7 summarizes the main contribution of the dissertation and the scope of future work.

The analyses in this dissertation are validated by using electromagnetic (EM) simulation (HFSS).

CHAPTER 2: Mm- Wave Proximity Coupled Patch Antenna-in-Package

2.1 Introduction

Mm-Wave has a small wavelength so that the integrated circuits (ICs) and the antennas can be integrated within a single package, reducing the antenna form-factor. The small wavelength at these frequencies (10 mm to 1 mm) allows integration of integrated circuits (ICs) with antennas within a single package or chip, as the antenna form-factor reduces. Several approaches to integrate mm-wave antennas with their IC components, including antenna-on-chip (AoC), antenna-on-board AoB, and antenna-in-package (AiP).

Antenna-on-chip (AoC) involves implementing the antenna directly on the same RFIC chip, so the antenna is integrated on Si material. Thus, this approach is more reliable and has low cost. However, Si material has low resistivity and high permittivity, which increases loss in the substrate. As a result, AoC has low radiation efficiency. Some techniques are used to improve the AoC efficiency [21], such as:

- Substrate Thinning by less than $\lambda_g/4$ cuts off all surface wave modes except TM_0. This technique will reduce the low resistivity substrate's loss due to surface wave modes' existence [22].
- The proton implantation approach is used to increase the resistivity of the Si substrate [23].
- The micromachining technique is used to remove silicon substrate in areas where AoC produces a high field strength [24].
- The superstrate layer of high permittivity is implemented on top of the antenna substrate. The superstrate layer acts as a desirable part of the antenna and a

protective layer [25]. This technique, which is called superstrate focusing, improves the antenna's efficiency and directivity.

Unfortunately, these techniques are different from the mainstream high-volume processing techniques. Thus, the cost of AoC will increase, which will reduce the reliability of the whole system.

Reference [26] describes a front-end receiver with an on-chip antenna for V-band broadband wireless applications. This chip consists of a low-noise amplifier (LNA), dual-gate mixer, voltage-controlled oscillator (VCO), and folded slot antenna. The folded slot antenna‘s dimensions are W=10 µm and L=900 µm. The antenna provides 7 GHz bandwidth for V-band. The area of this chip occupies a 1.6 x 2 mm^2 active area. The measured antenna gain at 50 GHz is -4.9 dBi, which is low gain. The die microphotograph of the V-band receiver front-end with the on-chip antenna is shown in **Figure** 2.1.

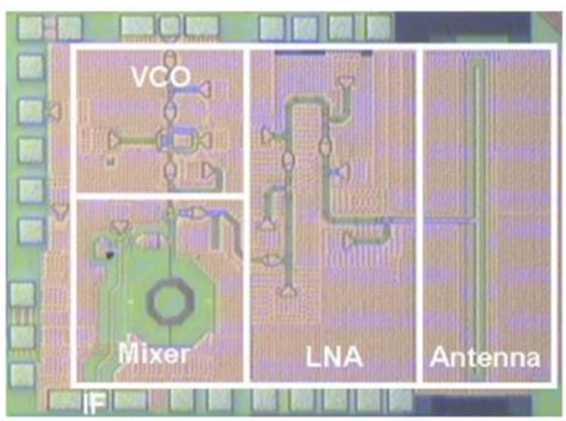

Figure 2.1 Example of AoC: Die micro photographic of the V-band receiver front-end [26].

In addition to AoC, **antenna on-board (AoB)** is another option to integrate the antenna within a single package. In this technique, antennas are directly implemented on the application printed circuit board (PCB). It saves silicon area and avoids the extra cost related to expensive packaging processes. This approach has the lowest price and the advantage of separate design ICs and antennas. PCBs with low loss, such as FR-4, Duroid, etc. [27] – [29], help reduce the material loss and improve the antenna's radiation efficiency. However, the main challenge in this approach is the routing of electrical signals. This interconnection between the antenna and the integrated circuits (ICs) causes more loss, especially in high-frequency applications where the wavelength is short (1- 10 mm). The interconnection between the antenna and the ICs is long at high frequency, where the wavelength is short. The loss is proportional to the distance between the antenna and the ICs. Also, this approach consumes ample space. Paper [30] presents an example of the AoB technique. This paper introduces a 32-element phased array centered at 64 GHz using multiple SiGe chips on a single printed circuit board. The arrays can be scanned to ±50° in the azimuth.

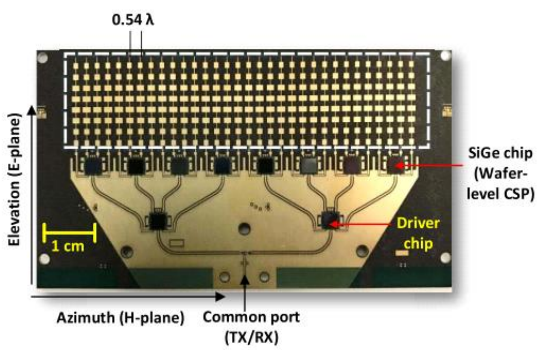

a. 64-GHz 32-element phased array with four-channel SiGe chips.

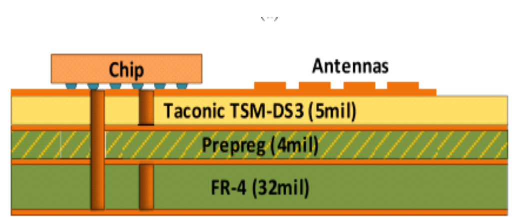

b. Details of the PCB stackup.

Figure 2.2 Example of AoB: the 64-GHz phased array with the SiGe Tx/Rx modules [30].

The gain of the 32-elements phased array is 14.5 dBi. However, the total antenna aperture (A) is 2.7 x 9.2 cm^2, a large area compared to AoC. **Figure** 2.2 shows the phased array with the SiGe Tx/Rx modules and the PCB stack-up details.

The Antenna in-package AiP is another solution to integrate the antenna within a single package. In this approach, the antenna is combined with an IC die into a standard surface-mounted chip-scale package device. Besides AoB, the AiP approach is flexible for fabricating the antenna on low permittivity and high resistivity substrate. Additionally, the AiP consumes less area and has less interconnection loss than integrating the antenna in the package. Thus, AiP has high radiation efficiency, making AiP a promising solution for wireless communication. Many substrate technologies have the appropriate properties for implementing the package with the embedded antennas, such as low-temperature cofired ceramic (LTCC), glass, liquid crystal polymer (LCP), and Teflon [19], [31]–[33].

IBM researchers have demonstrated a complete AiP system that is cost-effective plastic packaging technology for a fully integrated 60GHz radio, used for communication in the 60GHz ISM band [3]. They used the surface-mountable land-grid array (LGA) and direct chips attach package technologies. Both package technologies provide, which are shown in **Figure** 2.3, a cost-effective packaging solution for gigabit per second wireless communication in the 60-GHz ISM band. Each package technology uses a standard low-cost mold material.

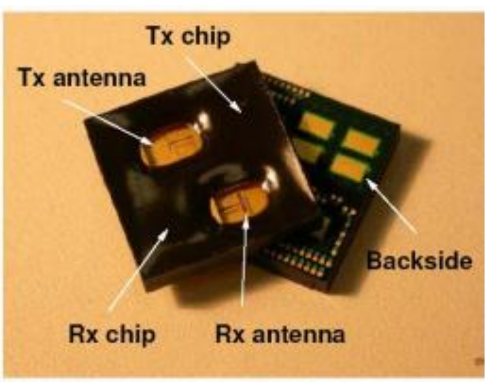

a. Land-grid array (LGA)

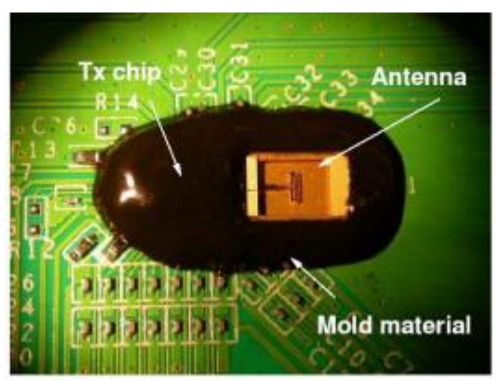

b. Direct chips attach (DCA)

Figure 2.3 Surface mountable land-grid array (LGA) and Direct chips attach (DCA) package technologies [3].

In this work, we use the AiP approach because its implementation provides flexibility in fabricating the antenna on low-loss materials. Also, it consumes less area and has low interconnection loss. As we will show in this work, the AiP approach allows for entirely separate packaged antennas coupled to a general-purpose IC chip, a universal chip. For this work, we selected proximity coupled patch antennas (PCPA) because they do not require complicated fabrication processes and produce moderate gain at the broadside. These advantages make them suitable for AiP design and the proposed flexible antenna lid approach.

The AiP with universal chip provides flexibility in various antenna requirements bandwidth, directivity, polarization) without making any changes in the designed chip (RFIC). We aim to investigate if a thin fixed feed line fabricated on the fixed RFIC chip can be coupled to various antennas at different operating frequencies and polarization (linear or circular). The antenna lid will be changed only without changing the designed chip (RFIC). Moreover, the antenna will be fabricated in low-loss materials. As a result, low-cost and high-performance mm-wave devices can be achieved. Furthermore, we want to understand the limitations required by the thin feed line's fixed dimensions on frequency, bandwidth, gain, and polarization specifications. In other words, we want to analyze the EMC microstrip antenna coupled to a fixed feed line to help understand the design space and provide quick estimates of the antenna's dimension.

The modeling and analysis of a proximity coupled patch antenna are difficult due to the complex EM interactions involved between the feed and the radiation element. Moreover, for the target design of replaceable antenna lids for AiP, the geometrical dimensions of the feed line are fixed from the IC design technology, and the only variables are the patch geometry and substrate parameters. Several models have been used to explain the behavior of the proximity coupled patch antenna (PCPA). These existing models would help our intuitive understanding of the PCPA. In the next section, we introduce some of these models.

2.2 Models to analyze the Electromagnetically coupled patch antenna

As I mentioned before, an electromagnetically coupled (EMC) microstrip antenna is a commonly used planar antenna suitable for AiP design. This antenna is popular for mm-wave applications because it does not require complicated fabrication processes and produces moderate gain at the broadside. This section will give a brief review of the patch antenna and some models that explain the patch antenna's performance.

2.2.1 Patch antenna

The rectangular patch antenna is the most widely used configuration. Transmission-line (TLM) and cavity models are the most comfortable model for analyzing the patch antenna. TLM represents the rectangular patch antenna by two slots separated by a low impedance transmission line with length L. Each slot of width W and height h. Furthermore, the cavity model represents the antenna as an array of two narrow radiating slots, with width W and height h [35].

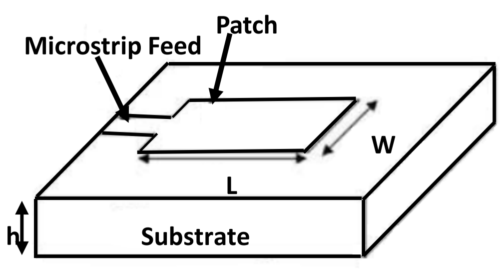

a. Patch antenna.

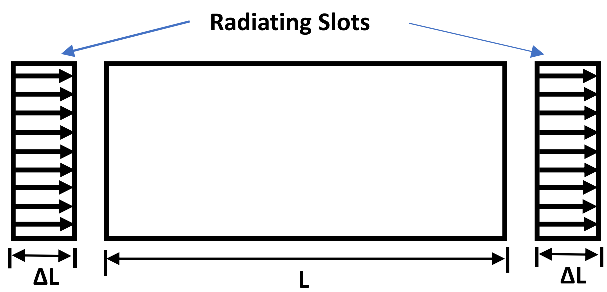

b. Top view showing the two radiating slots.

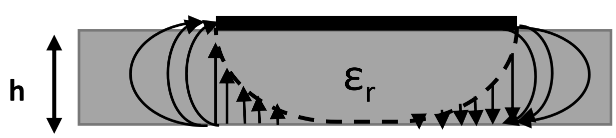

c. Side view showing the electric fields.

Figure 2.4 Rectangular patch antenna.

The patch antenna acts as a cavity resonator with a dominant mode TM_{10}. The resonant frequency of TM_{10} is:

$$f_{r_{10}} = \frac{c}{2L\sqrt{\epsilon_r}} \tag{2.1}$$

Because the patch's dimensions are finite along the length and width, the fields at the patch edges are fringing fields and straight-line underneath the patch. The fringing fields extend the dimension of the patch length on each side by a distance of ΔL. The patch antenna's length is electrically greater than its physical dimensions L by 2ΔL because of the fringing effects at the two edges[35]. See **Figure** 2.4 for more illustration. Also, some of the waves travel in the substrate and some in the air. As a result, effective dielectric constant ε_{eff} is introduced to account for the fringing and the wave propagation in the line.

$$L_{eff} = L + 2\Delta L = \frac{c}{2L\sqrt{\epsilon_{eff}}} + 2\Delta L \tag{2.2}$$

$$\varepsilon_{eff} = \frac{\varepsilon_r+1}{2} + \frac{\varepsilon_r+1}{2}[1 + 12\frac{h}{w}]^{-1/2}, \quad W/h > 1 \tag{2.3}$$

The extension length ΔL is a function of ε_{eff} and the width-to-height ratio (W/h). A very common approximation relation for the normalized extension of the length is [36]:

$$\frac{\Delta L}{h} = 0.412\frac{(\varepsilon_{eff}+0.3)(\frac{W}{h}+0.264)}{(\varepsilon_{eff}+0.258)(\frac{W}{h}+0.8)} \tag{2.4}$$

2.2.2 Modeling the proximity coupled patch antenna (PCPA)

The PCPA configuration is shown in **Figure** 2.5. The patch antenna is electromagnetically coupled to the microstrip feed line. The PCPA consists of two layers, with the microstrip feed on the lower layer and the patch antenna on the upper layer. The feed line terminates in an open-end underneath the patch. Thus, the feed line is called an electromagnetically coupled microstrip line.

Several circuit models have been used to explain the proximity coupled patch antenna (PCPA). **Figure** 2.5 shows a two-layer of PCPA configuration. These existing models add little to our intuitive understanding of the PCPA. While the applied models explain the PCPA behavior, the models are limited by many assumptions and do not apply to all cases. Several researchers have provided different models that describe the interaction involved between the feed line and antenna. However, most researchers simplify their models by many assumptions, which make their models limited for specific applications only.

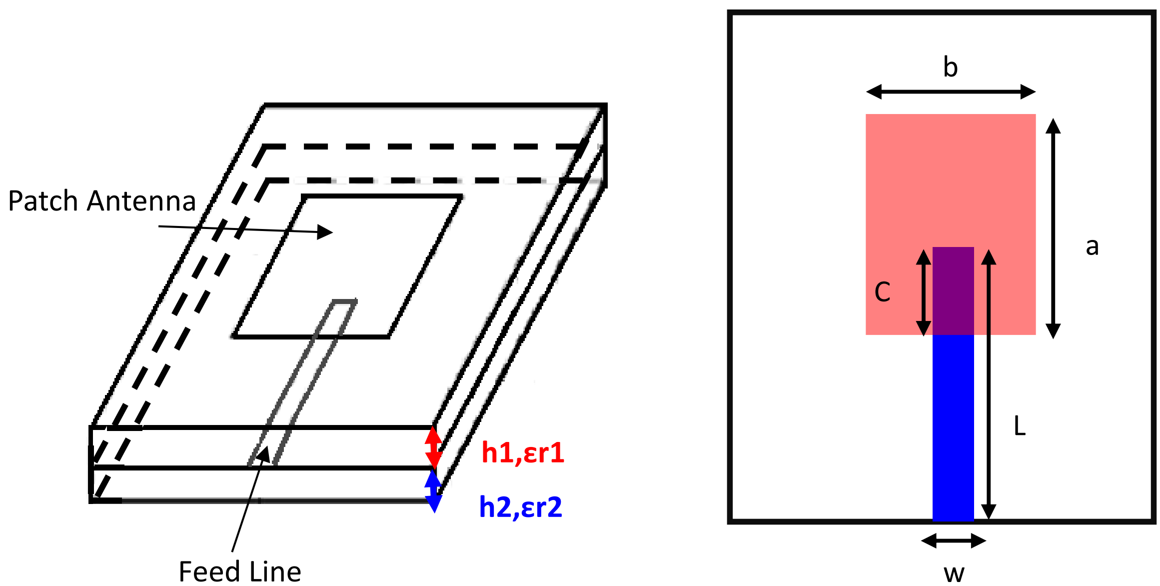

a. 3D plot of the two-layer PCPA. b. Top view of the PCPA.

Figure 2.5 The two-layer PCPA configuration.

Many well-known techniques are available for the analysis and design of microstrip PCPA, and they fall approximately into the following four groups,

1. Multiport network model technique (MNM) [37]–[39].
2. Transmission Line analysis [40], [41].

3. Electromagnetic full-wave techniques, using numerical methods [42].

4. Cavity Model [43].

- **Transsion Line Model (TLM)**

In [40]**,** Zhang, Fukuoka, and Tatsuo introduced a TLM for the PCPA shown in **Figure** 2.6. They separated the antenna system into three regions. Region 1 is the feed line, an inverted microstrip line; region 2 is the overlap area between the antenna and the feed line. Region 3 represents the uncoupled part of the patch antenna, which acts as a suspended microstrip line.

In region 2, there exist two independent moded with different values of propagation constant. One mode is called even mode, and the other one is an odd mode. There are two

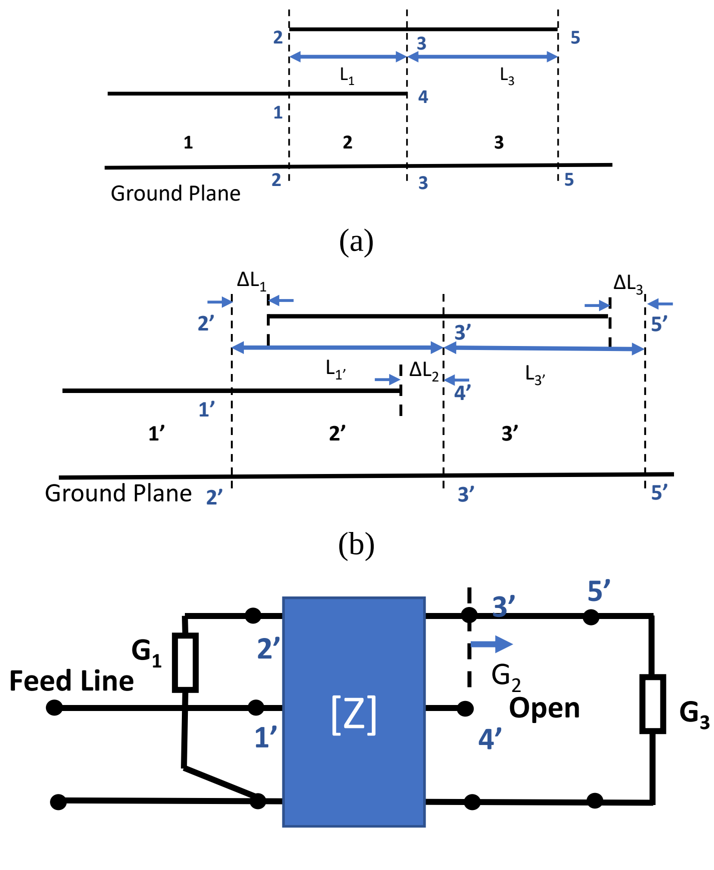

Figure 2.6 Electromagnetically coupled patch antenna system. (a) Side view of the patch antenna system. (b) Equivalent structure of the patch system, including the extensions at the open ends. (c) Transmission line model for the patch antenna system [40].

characteristic impedances at each mode corresponding to the upper (patch antenna) and lower (feed line) strips. A four-port network can represent this region. The Z-matrix of this four-port network includes all the impedances and propagation constants for both modes, even and odd, using microwave network theory. They also have the discontinuities at the patch's open ends (end 2 and 5) and the stripline's open-end (end 4) in their analysis by represented these ends by hypothetical extensions ΔL_1, ΔL_2, and ΔL_3. See **Figure** 2.6b for more illustration. The antenna radiates electromagnetic energy primarily through the slots 2'-2' and 5'-5' in **Figure** 2.6c. Thus, G1 and G3 represent the radiation conductances at 2'-2' and 5'-5', respectively.

However, this model is valid for small height because many empirical expressions, such as the fringing effects, are used based on low-frequency approximation. The radiation conductance is another source of uncertainty. If the substrate has a high dielectric constant and a large thickness, this model's radiation conductance must be redefined. Moreover, the surface wave effect is not included in the analysis of this model.

In [41], Jaisson proposes a new transmission line model for computing the proximity coupled patch antenna's input impedance. **Figure** 2.7 shows PCPA. His model helps approaching final design parameter values quickly. For his TLM, these are some assumptions:

- To maximize radiation efficiency, $W_p \approx L_p$.
- Both the patch and the strip feed line centers are at the center of the x-axis to prevent x-axis modes' excitation and ensure y-axis linear polarisation.
- $\varepsilon_{r1} = \varepsilon_{r2}$ and $h_1 = h_2 = h$.
- The quasi-transverse electromagnetic mode (quasi-TEM mode) M_μ is wanted for radiation resonates between patch edges in planes y = 0 and y= L_p.

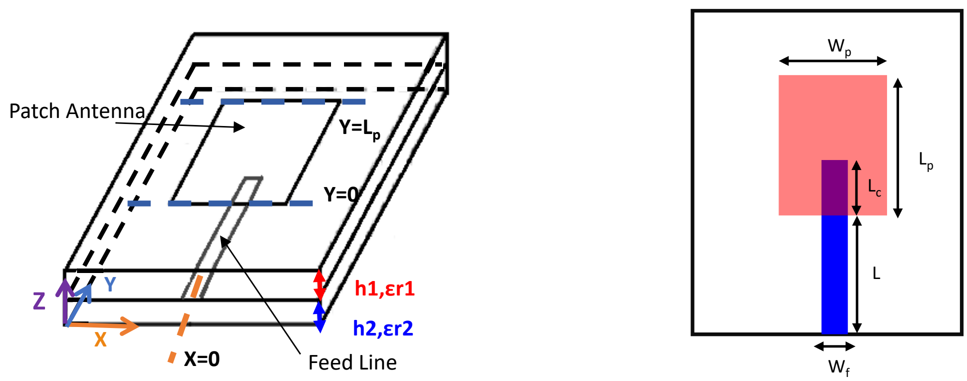

a. 3-D plot of PCPA.

b. Top view of the PCPA.

Figure 2.7 PCPA configuration.

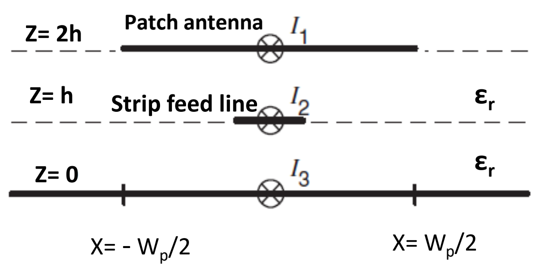

Figure 2.8 Cross-section of EMC length [41].

Electromagnetic couple (EMC) section $0 < y < L_c$ works like two coupled quasi-TEM transmission lines, the feed line and the patch line. **Figure** 2.8 shows the following: the current flow on the patch I_1, the current flow on the feed stip $I_{2,}$ and the current flow on the ground plane. I1 and I3 are decomposed into odd and even modes. The feed strip's current I_2 is the return current and is equal to $-I_1-I_3$.

At pure odd mode, $I_1= -I_3$, so, $I_2= 0$. The odd mode's E-field is normal to the feed strip, and its H-field is parallel to the feed strip. See **Figure** 2.9 for more illustration. The odd mode's E-

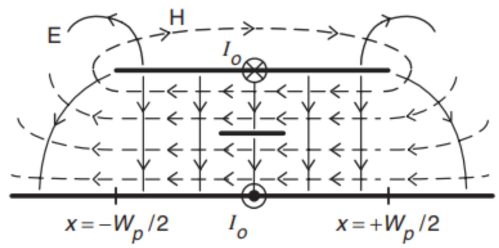

Figure 2.9 Odd mode M_μ [41].

field and H-field are unchanged if the feed strip is removed because of w_f and 2h << W_p and I2=0. The odd mode is the quasi-TEM mode M_μ of the microstrip line.

On the other hand, at pure even mode, $I_1 = I_3$. The E-field and the H-field of the even mode are shown in **Figure** 2.10. Because w_f and 2h << W_p, the finite patch acts as an infinite ground-plane. This TEM mode acts as a balanced sandwiched stripline with strip width w_f and substrate ε_r with height 2h, M_s.

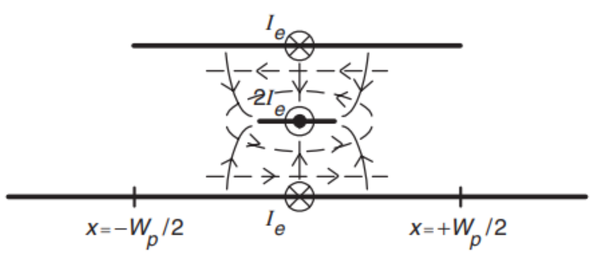

Figure 2.10 Even mode M_S [41].

The odd and even modes do not couple. The equivalent antenna circuit is shown in **Figure** 2.11. However, his model is limited to the case where the feed line and the antenna have the same height ($h_{patch} = h_{feed\ line}$) and the same permittivities (ε_r). See **Figure** 2.7 for more illustration. In the proposed proximity coupled patch antenna design, the antenna has a different height and substrate material than the feed line. Thus, we can not use this model.

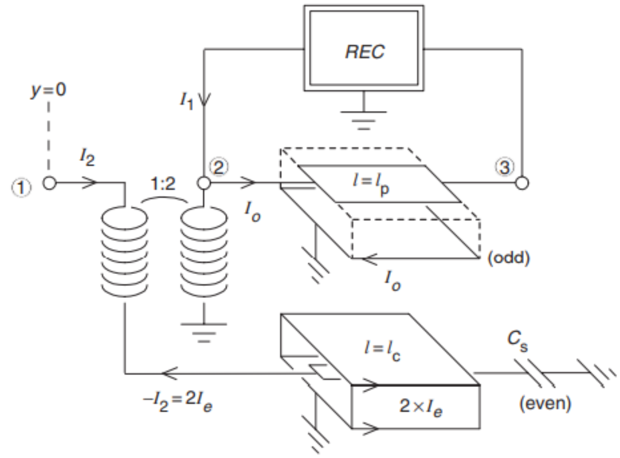

Figure 2.11 PCPA equivalent circuit [41].

These models and other developed models include many assumptions that make them work for a particular application. Also, they have extensive and complex computational procedures that make them challenging to implement [44], [45].

2.3 Array

The mmWave band has a significant path loss. The small wavelengths of mmWave frequencies enable large numbers of antenna elements to be implemented in the same form factor to provide high gains that can compensate for the isotropic path loss. Besides, in many mm-wave applications such as radar, direction finding, air traffic surveillance, microwave remote sensing, military radar, wireless communications, and weather forecast, beam steering is highly demanded. Thus, phased arrays are necessary to overcome a large amount of path loss and achieve the required adequate isotropic radiated power (EIRP) essential for high data rates and steer the beam.

A phased array is one of the beam steering methods, where the beam direction is electronically scanned to different desired directions. Each single antenna element is fed with a distinct β phase shift. The phased array required less maintenance than the mechanical steering of the antenna. Moreover, it is more flexible than mechanical steering.

The excitation amplitude and phase of each element in the phased array control its output to provide a custom shaping of the radiation pattern and scan the space pattern. The primary array antenna model consists of two parts: the element pattern, the pattern of one of the elements by itself, and the array factor, which is the array pattern with the actual elements replaced by isotropic sources. Thus, the array's total pattern is the product of the element pattern and the array factor. **Figure** 2.12 illustrates an equally spaced linear array of isotropic point sources. The array factor is given by [46]:

$$AF = \sum_{n=0}^{N-1} I_n e^{jknd\cos(\theta)} = \sum_{n=0}^{N-1} A_n e^{jn\,(kd\cos(\theta)+\beta)} \tag{2.5}$$

Where: $I_n = A_n e^{jn\beta}$, and N is the number of the antenna element.

Uniform amplitude (A_o) and spacing (d) linear phased array will be investigated in this dissertation.

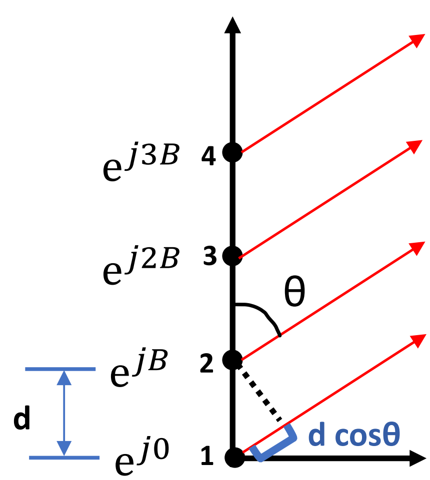

Figure 2.12 Equally spaced linear array of isotropic point sources.

Scanning angle

As I mentioned, beam scanning is highly demanded in many applications, such as wireless mobile communication. Thus, a wide beam angle range is required for these applications. For example, in mobile communication, a wide beam scanning angle is needed to track mobile users. Many researchers try to maximize the beam scan angle range of planar phased array for mm-wave applications. A 32-element TX/RX phased array at 60 GHz is presented in [47] with the pattern scans to ±30°. In [30] , the authors present a 32-element phased-array centered at 64 GHz, scanned to ±50° in the azimuth using a 5-bit phase shifter on the SiGe chip. The total antenna size is 2.7 × 9.2 cm2. The RF layer, which is antenna and transmission lines, is fabricated on a 5-mil (125 μm)-thick TSM-DS3 substrate with $\varepsilon_r = 3$ and tan $\delta = 0.0013$ and is placed on top of an FR-4 layer used for power supply and digital control signal distribution.

This dissertation also will present a phased array antenna with a fixed fed line at various operating frequencies. The phased array performance with a fixed fed line will be analyzed like side lobe level, scanning angle, reflection coefficient, and mutual effect between the antenna. In [30] , they could scan the phased array to ±50° in the azimuth. We study the impact of separating spacing between the antenna on the scan angle at different operating frequencies and the maximum scanning angle for our case where the feed lines structure is fixed. Thus, the separation space between the antenna will be variable.

CHAPTER 3: Linearly Polarized Fixed Fed Patch Antenna

3.1 Introduction

We intend to investigate if a thin fixed feed line fabricated on the fixed RFIC chip can be coupled to various antennas at different operating frequencies and polarization (linear or circular). The antenna will be changed only without changing the designed chip (RFIC). We will study and analyze the EMC microstrip antenna coupled to a fixed feed line to understand the design space and give quick estimates of the antenna's dimension. This chapter will focus on a linearly polarized patch antenna coupled to the fixed thin feed line.

The modeling and analysis of a proximity coupled patch antenna are rugged due to the complex EM interactions between the feed and the radiation element. Moreover, for the target design of replaceable antenna lids for AiP, the feed line's geometrical dimensions are fixed from the IC design technology. The only variables are the patch width, length, height, and substrate parameters. It is essential to determine the limitations imposed by the thin feed line's fixed dimensions on frequency, bandwidth, gain, and polarization specifications.

The cavity and transmission-line (TL) models are standard models used to analyze the patch antenna and estimate the patch antenna's dimensions. In the dominant TM_{10} mode, the resonant frequency f_o is inversely proportional to the patch antenna's length. However, this project's proposed antenna is proximity-coupled to a fixed feed line on a thin substrate. Thus, these models cannot accurately analyze the proposed patch antenna. In this case, we will provide a study to explain the behavior of the antenna's dimensions at different operating frequencies. Thus, the study helps estimate the size of the antennas at various operating frequencies and polarizations.

Several circuit models have been used to explain the behavior of the proximity coupled patch antenna (PCPA). These existing models add little to our intuitive understanding of the PCPA. While the applied models explain the PCPA behavior, the models are limited by many assumptions and do not apply to all cases. In [41], Jaisson proposes a new transmission line model for computing the proximity coupled patch antenna's input impedance. His model helps approaching final design parameter values quickly. However, his model is limited to the symmetric feed line between the patch antenna and the ground plane ($h_{patch} = h_{feed\ line}$). See **Figure** 3.1 for more illustration. In the proposed proximity coupled patch antenna design, the antenna's height does not equal the feed line's height. **The proposed patch antenna design is based on the design in** [1]**, where the feed line is on the top layer of the RFIC chip (thickness= 9.25 µm), and the antenna substrate is much thicker at a thickness of 125 µm.**

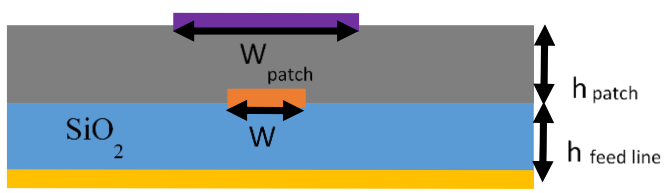

Figure 3.1 Stack-up view of proximity coupled patch antenna with substrate height equal to the substrate height of the feed line.

In this chapter, straightforward analysis is provided to understand the PCPA's behavior at different operating frequencies (f_o) and give a quick estimation for linear polarized antenna's dimensions values. We will focus on developing an analysis that studies how the antenna's dimensions change with operating frequencies in different situations like changing the substrate material or change the feed line dimension. Furthermore, we will investigate the frequency range where the linear polarized radiation can be achieved by only optimizing the antenna and the package dimensions. Also, we will study the factors that limit the frequency range. Moreover, this analysis also investigates how the antennas are sensitive to their dimensions (L_p, W_p, and h_p).

The proposed baseline model [1], shown in **Figure** 3.2, is a patch antenna for the W-band (80 GHz to 106 GHz) that is integrated on a thick quartz package (ε_r=3.8) and a feed line printed on a thin layer of SiO_2. Designs at several different operating frequencies and linear polarization states are explored and validated with a full-wave simulation using HFSS. The analysis provides estimates of the range of frequencies that can be generated using this approach.

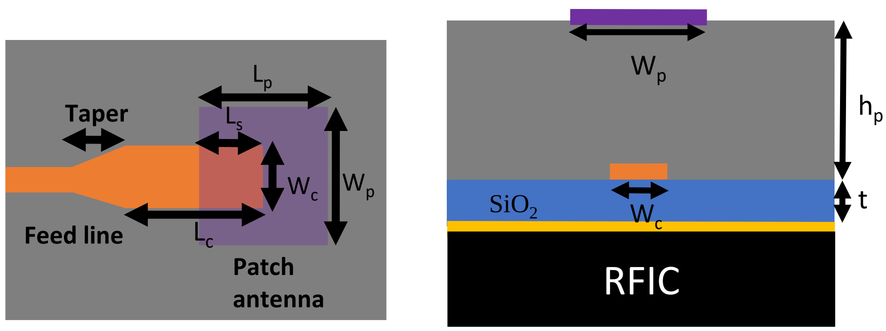

a. Top view b. Stack up view

Figure 3.2 The proposed proximity coupled patch antenna.

Table 3.1 Feed Line geometry for the proposed design [1].

Feed Line geometry	µm
L_c	690
L_s	L_{patch} /2
W_c	250
L_{tapper}	150
h_{TL}=t	9.25

3.2 Research Questions

This chapter's main objective is to generate a simple analysis that gives an intuitive understanding of the adaptable PCPA's behavior and gives a quick estimate for fixed-fed PCPA dimensions at various operating frequencies. This analysis helps us determine whether we can couple a fixed feed line to various LP adaptable antennas at different operating. Additionally, The analysis helps determine the fundamental limitations of the adaptable antenna mounted on top of the fixed RFIC chip. In this chapter, we study the linear polarized patch antenna. **Figure**. 3.2 shows the proposed patch antenna design. **This design is based on the design as published in** [1]. Many questions need to be answered to demonstrate the primary goal of this chapter.

Question 3.1: How do the LP patch's optimal dimensions vary when coupled to the thin fixed feed line at different f_o? This question helps to study the behavior of the antenna's dimensions at different f_o.

Question 3.2: Over what frequency range the linear polarized radiation can be achieved by only optimizing the antenna and the package dimensions? Also, what are the factors that limit the frequency range?

Question 3.3: How is the antenna sensitive to its dimensions? We will study which of the antenna's dimensions (L_p, W_p, h_p) affect input impedance matching performance between the antenna and the fixed feed line?

Question 3.4: Can these results be fit in a geometric model? An intuitive model of the EMC microstrip antenna and the feed line is generated to provide quick estimates of the antenna's dimension.

3.3 Coupling fixed feed line to various linearly polarized antennas at different fo

In this analysis section, the feed line is fixed to its original value (L_c=690 µm, W_c=250 µm) [1], and the patch geometry and mold height are variable. The procedure is as the following: the sequential nonlinear programming optimizer (Gradient) is run using HFSS software to find the optimal width (W_{opt}), length (L_{opt}), and height (h_{opt}) of the antenna, where the return loss is low ($S_{11} < -30$ dB), at several operating frequencies f_0 in W band (80.5 GHz to 106.5 GHz). The loss is not included in this analysis (tangent loss and conductivity loss). These optimal dimensions of the antenna (W_{opt}, L_{opt}, and h_{opt}) are then plotted for all operating frequencies f_0. Curves are fit to predict the behavior of the antenna. In the end, varieties of antennas that operate at different frequencies f_0 are designed to cover a broad band of frequencies at mm-wave the range. These analyses give us a better understanding of the relationship between the antenna's dimensions and operating frequency. **Figure** 3.3 illustrates the analysis procedure for this objective. This numerical analysis is also run for different antenna substrate materials to understand the relationship between the dielectric constant of the material and antenna dimensions. In the original design [1], the antenna is fabricated on a quartz substrate with ε_r=3.78. Other mold materials can be used as antenna lid's substrate, such as two-part aliphatic epoxide globtop and amine-cured two-pack epoxy cement. They have a dielectric constant of 2.9 and 5, respectively [48]. Furthermore, the antenna's fractional bandwidths (FBW) at different f_o are also studied in this analysis. We will find the antenna's fractional bandwidth for one case where the patch antenna is fabricated on quartz material (ε_r=3.78). At the end of this analysis, we include the material loss in our simulations to find the antenna radiation efficiency. We will show the impact of the loss on the antenna performance by presented the antenna efficiency and realized gain.

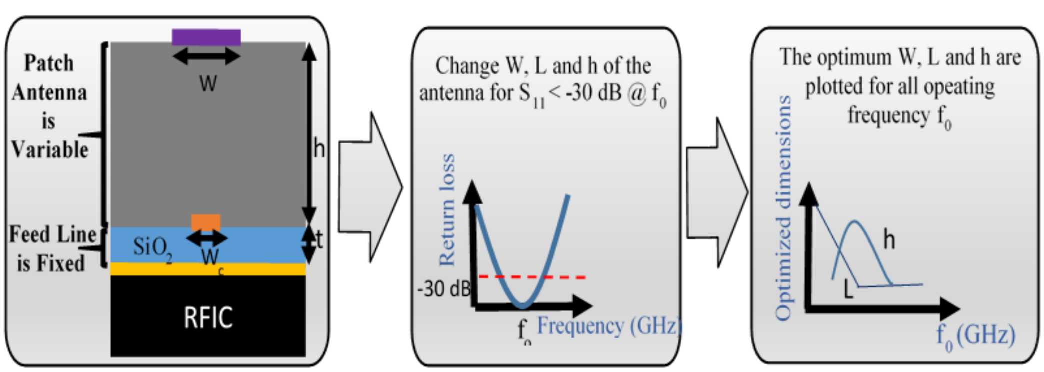

Figure 3.3 Optimization analysis procedure of LP fixed fed patch antenna.

Result and Discussion:

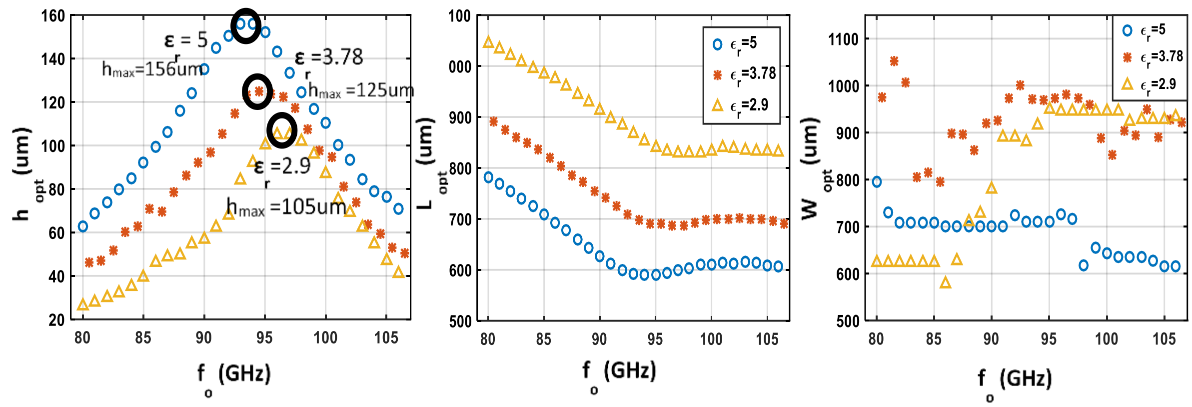

Figure 3.4 Optimal antenna's dimensions vs. operating frequency.

The simulation result of the optimal dimensions of the antenna is shown in **Figure** 3.4. The optimal antenna's height vs. operating frequency plot shows that the optimal height reaches a maximum at some point in the band of interest. I call it a critical frequency (f_c) as it is a salient feature that demarcates a change in behavior in both the optimal height and length plots. At frequencies above or below this critical frequency, the h_{opt} decreases. The critical frequency will be explained more in Chapter five of this dissertation. Very thin antenna substrates may be impractical and limit the ability to match the antenna without feed modifications. Besides, we can observe from the plot that as the dielectric constant ε_r increases, the optimal height of the antenna substrate (h_{opt}) must increase. Increasing the dielectric constant allows the frequency to be tuned over a wider frequency range within $h_{opt} > 50$ um. From plot L_{opt} vs. f_o, $f_o \propto {}^{1}/_{L_{opt}}$ at frequencies lower than the critical frequency. This is expected from the cavity and TL models analysis. Nevertheless, the optimal length of the patch is almost constant at frequencies higher than the critical frequency. Moreover, the antenna's dimensions vs. operating frequency plot indicates a little discernable pattern to the optimal width as the design frequency changes.

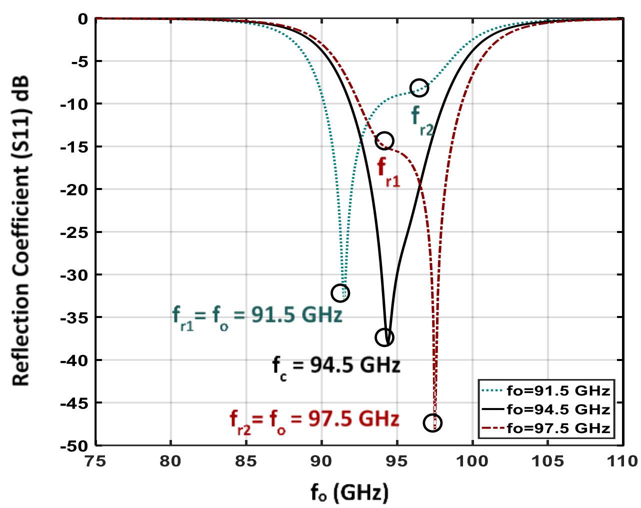

Figure 3.5 Reflection coefficient vs. frequency at three different operating frequencies (91.5 GHz, 94.5 GHz, and 97.5GHz).

Let's look at the return loss vs. frequency at different operating frequencies in **Figure** 3.5. We notice the following: **first, at a frequency higher or lower** than critical frequency, there are two resonant frequencies (f_{r1} and f_{r2}), but one of these frequencies has the lowest reflection coefficient (S_{11}< -25 dB). **Second, at the critical frequency (f_c)**, only one resonant frequency is located at the critical frequency. In other words, f_c is the frequency where the two resonant frequencies are overlapped.

The fractional bandwidth (FBW) vs. operating frequency is presented in **Figure** 3.6. This plot shows that the FBW reaches the maximum at some points in the interesting band (92.5 $\leq f_o \leq$ 98.5GHz), close to the critical frequency (f_c=94.5 GHz). At frequencies above or below these frequencies, the FBW decreases. As I mentioned before, FBW $\propto h/\lambda_g$. As the antenna's height to wavelength ratio (h/λ_g) increases, the FBW increases, and the reverse is true. **Figure** 3.7 shows FWB and h/λ_g vs. fo. Also, we noticed from the FWB vs. fo that the FBW decreases dramatically at f_o= 99.5 GHz and f_o= 91.5 GHz. As I mentioned earlier in this chapter, two resonates frequencies at operating frequencies above or below the f_c, but, at the $f_o = f_c$, the two resonates frequencies are overlapped. We conclude that as the two resonant frequencies moving away in the opposite direction, the FBW becomes narrower. **Figure** 3.8 plots Reflection coefficient vs. frequency at f_o= 98.5 GHz and f_o= 99.5 GHz.

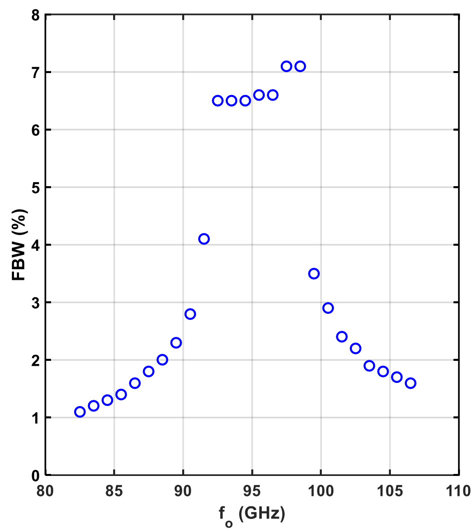

Figure 3.6 Fractional bandwidth vs. operating frequency.

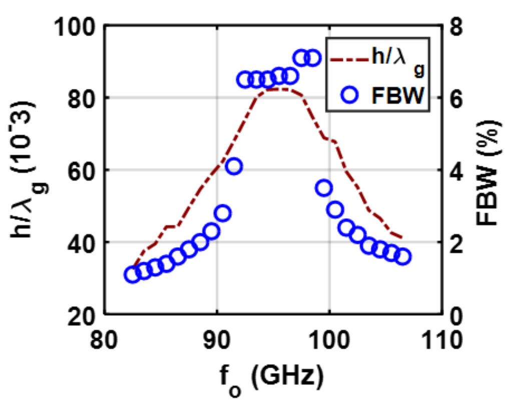

Figure 3.7 FBW and h/λ_g vs. f_o for antenna coupled to flared feed line case.

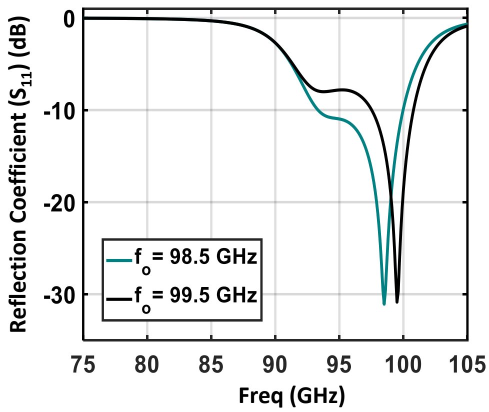

Figure 3.8 Reflection coefficient vs. f for antenna coupled to flared feed line case at f_o= 98.5 GHz and 99.5 GHz.

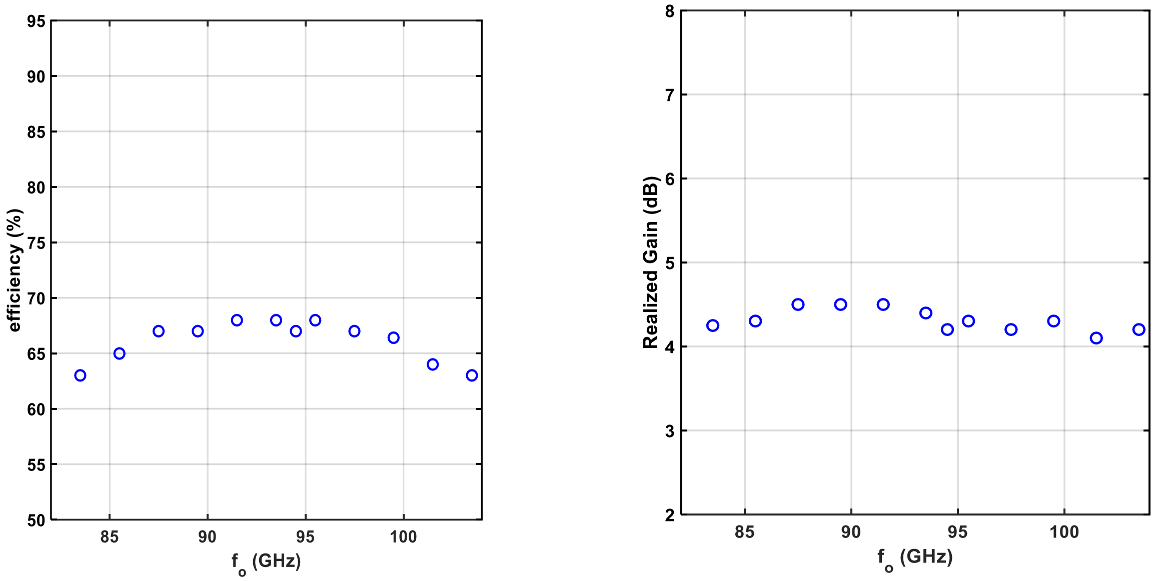

Figure 3.9 Efficiency and Realized gain vs. f_o for flared feed line design with loss effect.

The antenna efficiency and realized gain vs. f_o plots are presented in **Figure** 3.9. The antenna realized gain and efficiency also reach a maximum at the frequency equal to 93.5 GHz, close to the critical frequency (f_c=94.5 GHz). The efficiency and the realized gain decrease at frequencies below or above 93.5 GHz. The realized gain drop dramatically at frequencies above 93.5 GHz.

3.4 The sensitivity of the antenna to its dimensions

In addition to the above analysis procedure, a sensitivity analysis will be investigated in this chapter. Sensitivity analysis is provided to study how the antenna is sensitive to its dimensions. This analysis will help find the antenna's dimension (L_p, W_p, and h_p) with a significant impact on the antenna's operating frequency (f_o) and its impedance matching. These studies will help to understand the behavior of the antenna's dimensions with the operating frequency (f_o). Moreover, they allow us to estimate the linearly polarized patch antenna's dimensions over various operating frequencies.

In this analysis, the flared feed line is fixed to its original value (Lc=690 µm, Wc=250 µm)[1], and the patch is fabricated on a quartz substrate with ε_r=3.78. The procedure is as follows: one of the optimized antennas' dimensions (W_p, L_p, or h_p) is changing while the others are fixed. Then, we run the parametric sweep for the studied antenna's dimension (either W_p, L_p, or h_p) using HFSS software at each operating frequencies f_o. At each parametric value of the studied dimension, we check the reflection coefficient to be less than -20 dB ($S_{11} \leq -20$ dB).

Result and Discussion:

For the following sensitivity analysis, the parametric sweep of W, L, and h is performed, and the reflection coefficient (S_{11}) is simulated. This data is further collected for different operating frequencies (80.5 GHz-104.5 GHz). One example of the type of data collected is shown in **Figure** 3.10 for a frequency of 88.5 GHz. This large data set is used for sensitivity analysis in two ways.

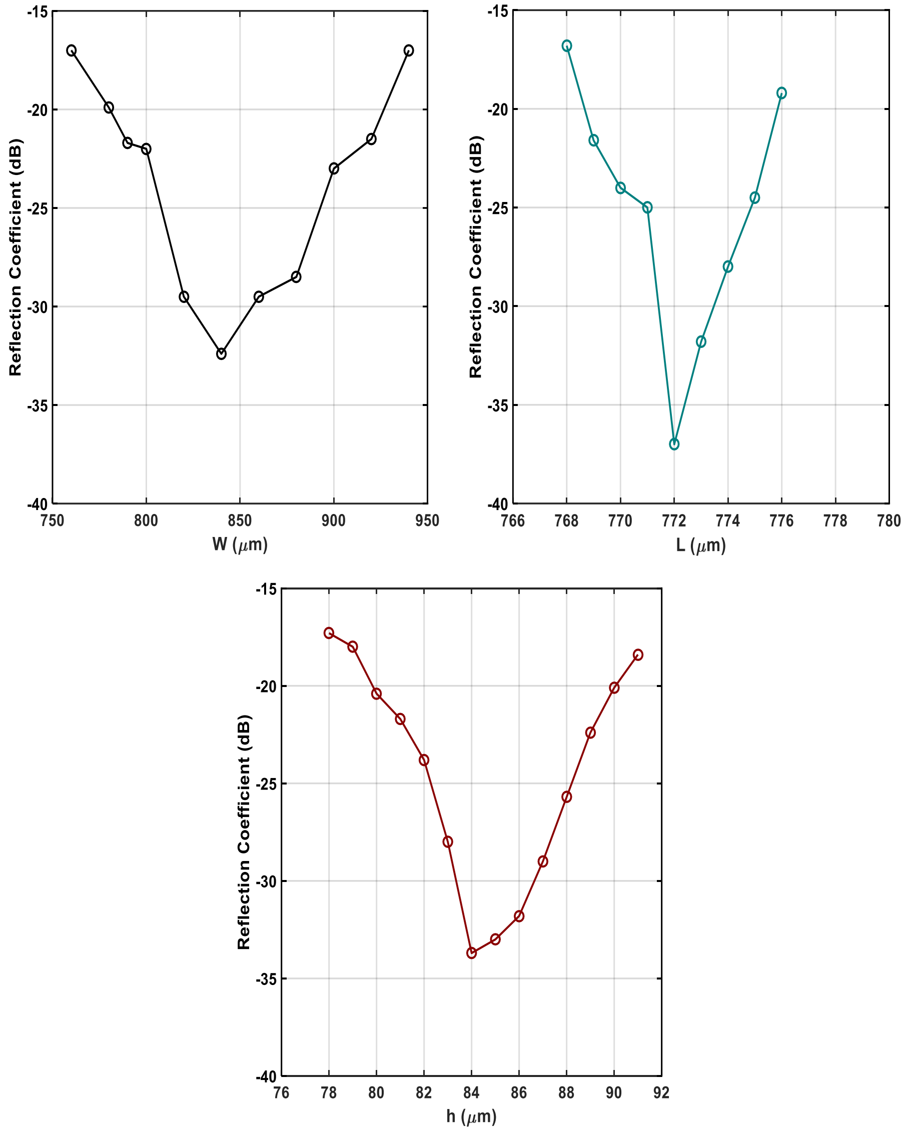

Figure 3.10 Reflection coefficient vs. antenna's dimensions (W,L, and h) at f_o= 88.5 GHz.

The first method is by using bar charts. The bar charts in **Fig**ure 3.11 show the patch antenna dimensions' parametric sweep (W, L, or h) over the operating frequencies. This bar chart is created by first determining the range of each dimension, W, L, and h, over which S_{11} is <-20dB. For example, at fo= 88.5 GHz, the range of W, L, or h, where the $S_{11} \leq$ -20 dB, are between 920 µm - 780 µm, 769 µm – 775 µm, and 80 µm - 90 µm, respectively. The chart in **Figure** 3.11 shows that variation in L and h affects S11 much more strongly than W. Therefore, the proximity coupled patch antenna performance is most sensitive to its height and length. Due to the relative insensitivity of W to the antenna's performance, a fixed-width value can be chosen for the curve fitting process of the W_{opt} vs. f_o and W_{opt} sharp analysis data curves (further discussed in the next Section 3.5). Thus, the number of variable antenna dimensions will reduce, and the curve fitting analysis will be more straightforward.

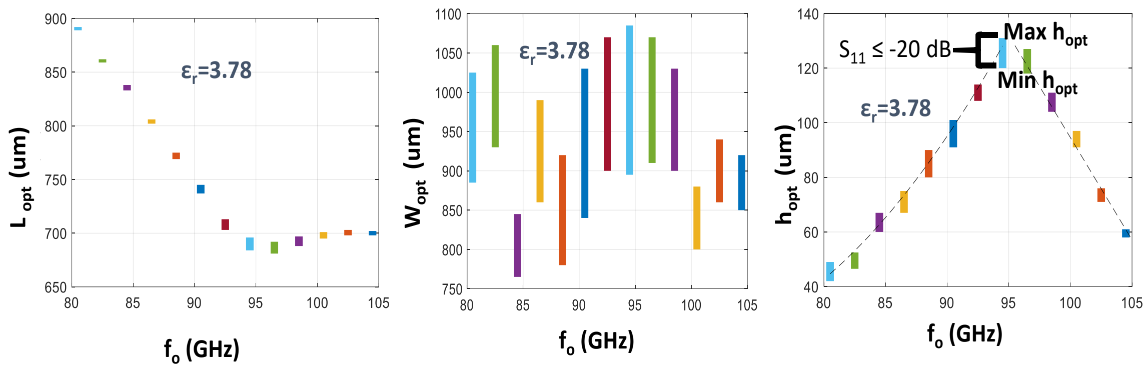

Figure 3.11 Sensitivity analysis: bar charts.

A second method of evaluating the sensitivity is by first determining the dimension value in um where S_{11} is a minimum for each sweep – for example, in **Figure** 3.10, S_{11} is minimum for W, L, or h at 825 µm, 698 µm, and 94 µm, respectively at f_o= 88.5 GHz. Now, we can plot S_{11} vs. an x-axis of the W, L, or h dimensions normalized to 825 µm, 698 µm, and 94 µm, respectively. Using this plot, we can compare the variation in S_{11} for W, L, or h simultaneously using one figure and compare their sensitivities to antenna performance. We plot S_{11} vs. Δ antenna's dimension (W,L and h) at three different operating frequencies(f_o), at f_o= 88.5 GHz < f_c, f_o=f_c=94.5 GHz and at f_o=100.5 GHz > f_o in **Figure** 3.12. The x-axis reference 0 is at the dimension that has the minimum S_{11}. In each plot, we observe that there is a much larger variation in S_{11} for normalized dimensions of W than for those of L or h – which again reiterates the observation above that the antenna performance is much more sensitive to its length and height than its width.

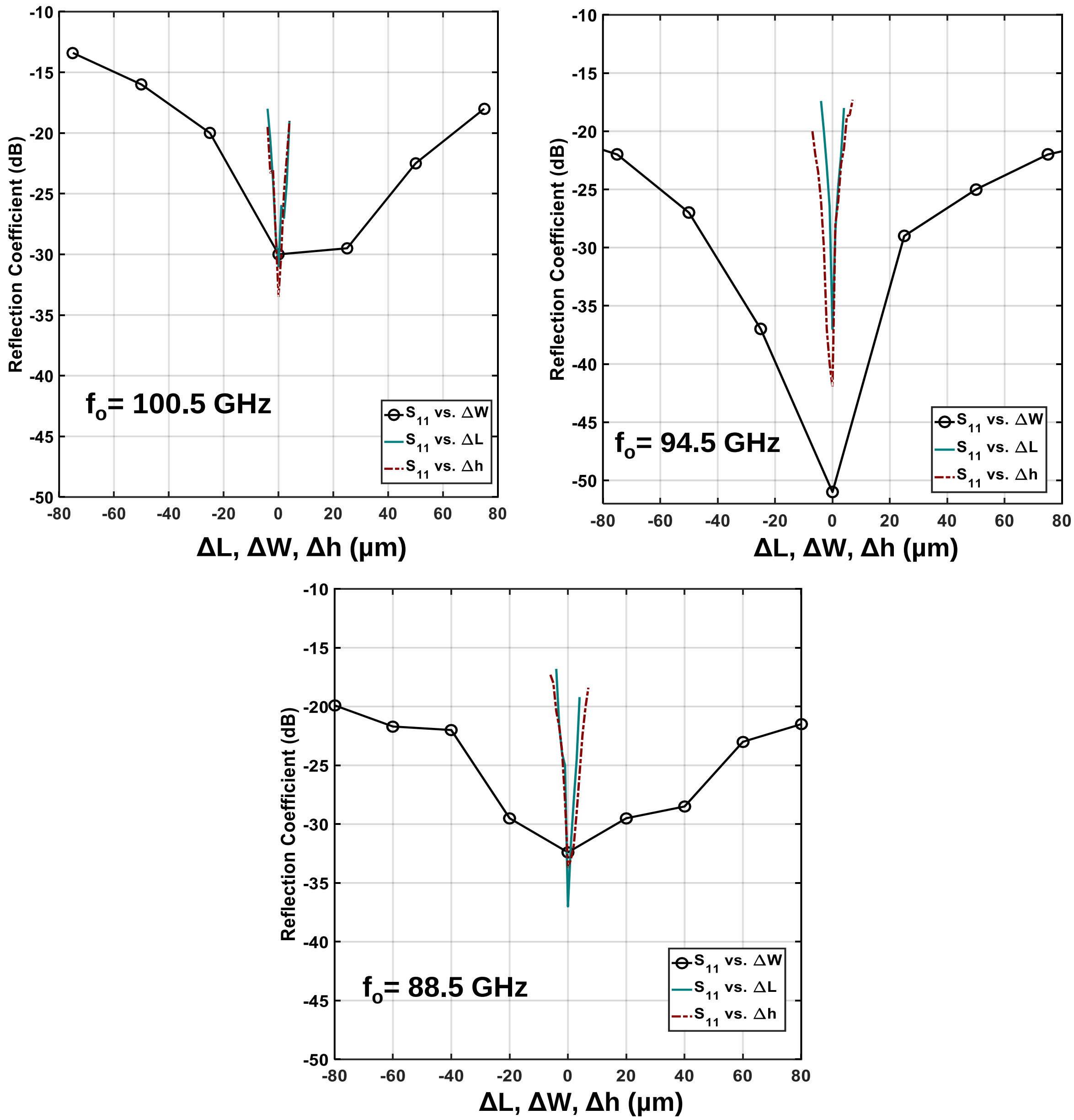

Figure 3.12 Reflection coefficient vs. ΔW, ΔL, Δh at different operating frequencies (88.5 GHz, 94.5 GHz, and 100.5 GHz).

3.5 Fitting the results in an intuitive model of the EMC microstrip antenna and the feed line

The curves in **Figure** 3.4 show the optimal antenna's dimensions vs. operating frequency plots for LP patch antenna coupled to the fixed feed line. Next, We want to generate mathematical functions that best fit the result data points in curves shown in **Figure** 3.4. Thus, the mathematical functions would help the antenna's designers to estimate the dimensions required for specific operating frequencies.

In section 3.3, The numerical analysis was run for different antennas' substrate materials, which are quartz, two-part aliphatic epoxide globtop, and amine-cured two-pack epoxy cement. They have a dielectric constant of 3.78, 2.9, and 5, respectively [48]. We observe that the optimal antenna's dimensions vs. operating frequency plots for the three different cases have similar behavior. Thus, we will run the curve fitting for one antenna' substrate material, which is quartz.

The Curve fitting process:

We try to fit the data to a simple mathematical function like a first-order or second-order degree polynomial function. The curve fitting analysis will be processed in Matlab.

In the following, the curve fitting process will be explained for each optimized antenna dimension.

1. The optimized length (L_{opt})

From plot L_{opt} vs. f_o, $f_o \propto {}^{1}/_{L_{opt}}$ at frequencies lower than the critical frequency. This is expected from the cavity and TL models analysis, as we mention in the introduction section. The reciprocal function is used to fit these data points.

$$L_{opt}(in\ \mu m) = \frac{a}{f_o} + b \tag{3.1}$$

Where: f_o: the operating frequency in GHz unit, $a = 113390,\quad b = -510.$

However, the optimal length of the patch is almost constant at frequencies higher than the critical frequency. This behavior is not as we expected. It is unclear why L is not $\propto {}^{1}/_{f_o}$.

$$L_{opt} \approx 692\ \mu m \tag{3.2}$$

2. The optimized Width (W_{opt})

The antenna's W_{opt} vs. operating frequency plot indicates a little discernable pattern to the W_{opt} as the design frequency changes. Moreover, the sensitivity analysis shown in Figure 3.11 and **Figure** 3.12 demonstrate that the proximity coupled patch antenna is not sensitive to its width. As a result, a fixed-width value is chosen to fit the W_{opt} vs. f_o's data curve.

$$W_{opt} = 920\ \mu m \tag{3.3}$$

3. The optimized height (h_{opt})

The optimal antenna's height vs. operating frequency plots shows that the optimal height reaches a maximum at f_c—the h_{opt} decreases at frequencies above or below this critical frequency (f_c). We try to use either first or second-order polynomial function because the polynomial function is simple and more comfortable to be used

The Coefficient of determination (R-squared) will indicate the proportionate amount of variation in the response variable, which is the optimized antenna's dimensions, explained by the independent variables fo in the linear regression model. As the linear regression model defines more variability, the R-squared will be more significant.

- $f_o \leq f_c$

The h_{opt} vs. f_o data at operating frequencies below f_c can fit a first-order and second-order polynomial function. To test which of these functions is more accurate and closer to the data, we used the R-squared equation.

The first-order fitted equation is:

$$h_{opt}(in\ \mu m) = \ aa_{h1}\ f_o + \ bbc_{h1} \tag{3.4}$$

Where: f_o: the operating frequency in GHz unit, $aa_{h1} = 6,\ bb_{h1} = -439.7.$

The second-order fitted equation is:

$$h_{opt}(in\ \mu m) = a_{h1}\, f_o{}^2 + b_{h1}\, f_o + c_{h1} \qquad (3.5)$$

Where: f_o: the operating frequency in GHz unit, $a_{h1} = 0.15,\ b_{h1} = -19.5,\ c_{h1} = 671.$ The second-order R-squared value is 99.2 % and higher than the R-squared value of the first-order polynomial function, 98.3 %. The R-squared value difference is marginal, so we try the two equations to estimate the antenna's height at f_o= 78GHz, a frequency point out of the interested frequency range (80.5 to 106.5 GHz). Using the fitting equations for h_{opt}, W_{opt} and L_{opt}, the estimated dimension for antenna operating at 78 GHz, is presented in Table 3.2. These estimated antenna's dimensions at f_o= 78 GHz are used to simulation the antenna in HFSS software. The result in **Figure** 3.13 shows that the second-order function gives an acceptable estimation for the h_{opt} value. The operating frequency (f_o) using the second-order equation to estimate the h_{opt} is 77.1 GHz, which is close to the desired operating frequency f_o=78 GHz. Besides, the reflection cofficient= -18.2 dB which is acceptable value. On the other hand, The operating frequency (f_o) using the first-order equation to estimate the h_{opt} is 69.9 GHz, and the reflection coefficient = -7.9 dB. Thus, The second-order equation is chosen to fit the h_{opt} vs. f_o data.

Table 3.2 The estimated antenna's dimensions at f_o=78 GHz by using the fitted equations.

L_{opt}= $\frac{a}{f_o} + b$ (μm)	**W_{opt} (μm)**	**h_{opt} (μm) First-order equation**	**h_{opt} (μm) Second-order equation**
941.1	920	25.3	36.4

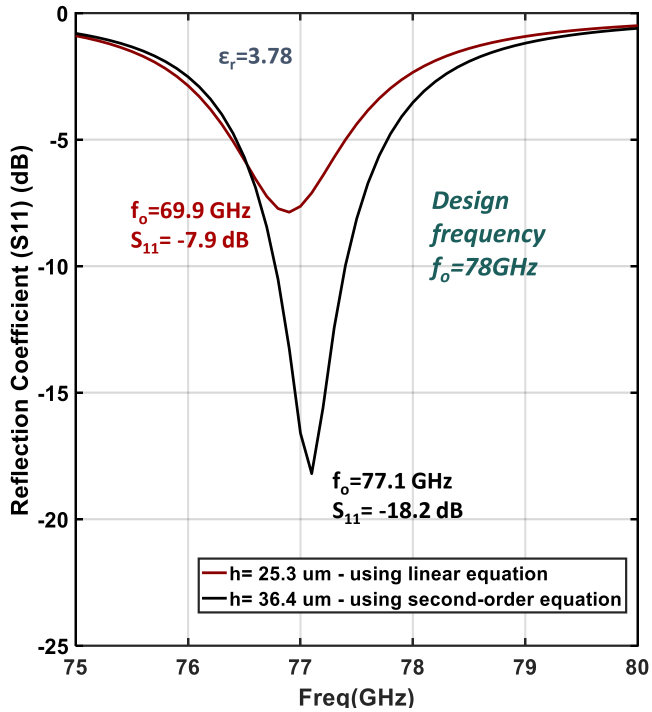

Figure 3.13 S_{11} vs. f of the estimated antenna's dimension at f_o= 78 GHz using the two fitted equations of h_{opt} data.

- $f_o \geq f_c$

h_{opt} vs. f_o at operating frequencies above f_c can fit a first-order and second-order polynomial function. R-squared value of the two polynomial is the same and equal 98.6 %. Both polynomial functions give the same estimated value for the height of the antenna. See Table 3.3. Thus, the first-order is chosen to fit the h_{opt} vs. f_o data because it is more uncomplicated and easy to use.

The first-order fitted equation is:

$$h_{opt}(in\ \mu m) = a_{h2}\ f_o + b_{h2} \tag{3.6}$$

Where: the operating frequency in GHz unit, $a_{h2} = -7.5,\ b_{h2} = 843.6.$

The second-order fitted equation is:

$$h_{opt}(in\ \mu m) = a_{h2}\ {f_o}^2 + b_{h2}\ f_o + c_{h2} \tag{3.7}$$

Where: f_o: the operating frequency in GHz unit, $a_{h2} = 0.03,\ b_{h2} = -12.91,\ c_{h2} = 1117.$

Table 3.3 The estimated antenna's dimensions at f_o=107 GHz by using the fitted equations.

h_{opt} (μm) First-order equation	h_{opt} (μm) Second-order equation
42.17	42.77

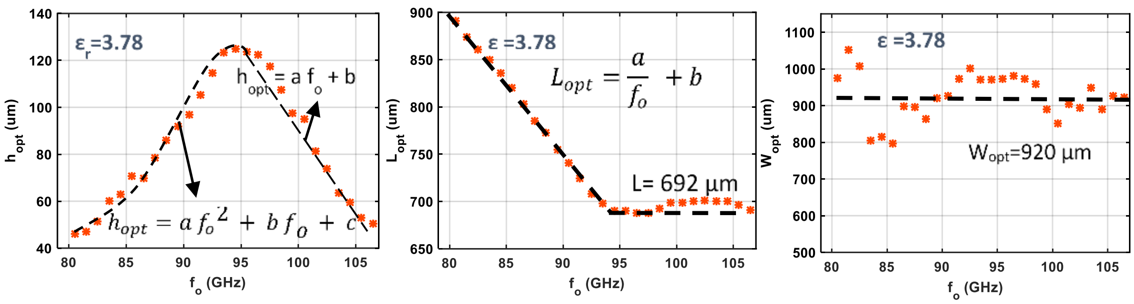

Figure 3.14 Optimal antenna's dimensions vs. operating frequency.

The generated equations of the optimal antenna's dimensions are fitted on the data curves in **Figure** 3.14. Three operating frequencies are chosen to test the generated equation: two operating frequencies (f_o = 78 GHz and f_o= 107 GHz) are out of the frequency band (80.5 GHz to 106 GHz) and one f_o at the frequency band center (f_o = 94 GHz). The generated equations are applied to estimate the patch antenna's dimensions at the intended operating frequencies (78 GHz, 107 GHz, and 94 GHz). Then, we use the three antennas' estimated dimensions to run the simulation and check if the equations give an acceptable estimation for the antenna's dimensions. The results, shown in **Figure** 3.15 and **Figure** 3.16, illustrate that this analysis provides good start values for the antenna's dimensions. The summarization of the curve fitting analysis is presented in Table 3.4. The percent errors between the predicted and designed frequency are very low.

Table 3.4 The simulated results of the curve fitting analysis.

Design f_o (GHz)	78	94	107
Simulated f_o (GHz)	77.1	93.7	107.7
Percentage of errors (%)	1.1	0.3	0.7
S11 at simulated f_o (dB)	-18.2	-32.7	-24.2
Realized Gain at design f_o (dBi)	4	6.1	6.1

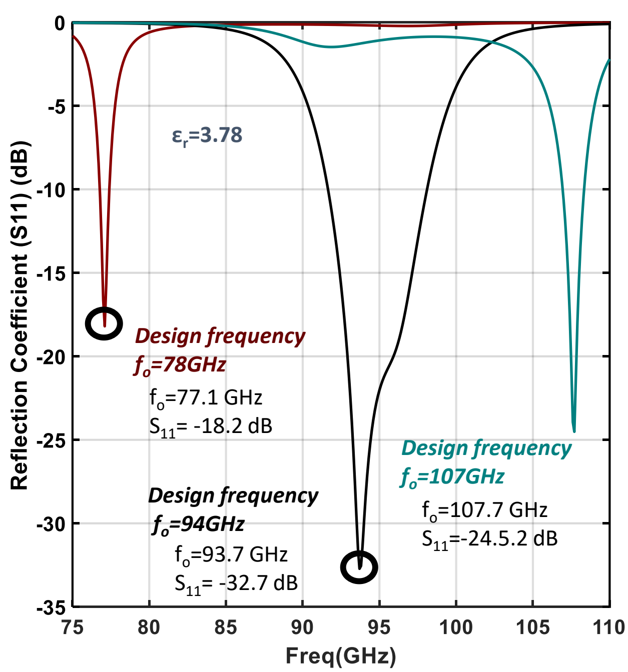

Figure 3.15 Reflection coefficient vs. frequency at three different operating frequencies (78 GHz, 94 GHz, and 107 GHz).

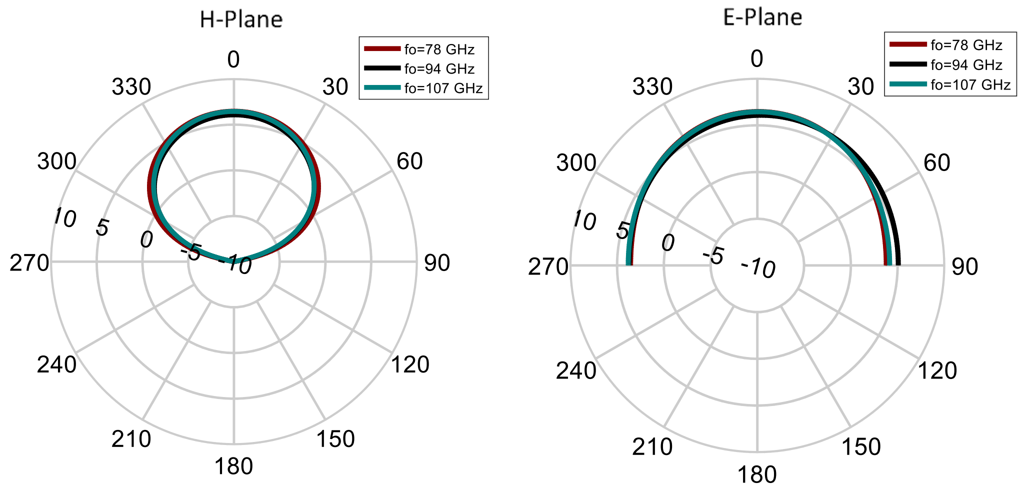

Figure 3.16 Radiation patterns of the proposed proximity coupled patch antenna.

The purpose of this fitting the data to these equations is to generate a library of expressions that designers can use to create other antenna lids. However, these curve fitting processes should be redesigned for other mold materials, which can be used as antenna lid's substrate and for other feed line designs. In this work, we analyze the proposed antenna-in-package of a universal chip for two mold materials beside the quartz as the substrate for the antenna, two-part aliphatic epoxide, and globtop amine-cured two-pack epoxy cement. This analysis helps predict the antenna's dimensions, but the fitted model equations would change as the antenna substrate material changes. The long-term goal is to generate a model that fits more mold materials. The optimization analysis will rerun for different mold materials, and then the results will be fit in equations. Moreover, the generated model will predict the critical frequency at each mold materials case and feed line design.

3.6 Research Outcomes

In this chapter, analyses are generated to predict the range of the operating frequencies that can be achieved by coupling the linear polarized antenna to the fixed feed line. In these analyses, we optimize the patch geometry and mold height to operate at a variety of frequencies f_0.

Furthermore, we investigate how the antenna is sensitive to its dimensions (L_p, W_p, and h_p). Moreover, the optimized antenna's dimension vs. operating frequencies data was fitted to a characteristic geometric model. Also, this intuitive model is used to provide a quick estimate of the antenna's dimensions.

Based on the primary research questions identified at the beginning of the chapter, the outcomes are listed below:

Question 3.1: How do the LP patch's optimal dimensions vary when coupled to the thin fixed feed line at different f_o? This question helps to study the behavior of the antenna's dimensions at different f_o.

The optimal antenna's dimensions vs. operating frequency plots show that the optimal height and length change their behavior at a specific frequency that I call a critical frequency (f_c). At operating frequencies above or below this critical frequency, the optimal height (h_{opt}) decreases. From plot L_{opt} vs. f_o, f_o is inversely proportional to the patch antenna's length at frequencies lower than the critical frequency. This is expected from the cavity and TL models analysis. However, the patch's optimal size is almost constant at frequencies higher than the critical frequency, unexpected behavior. Moreover, the antenna's dimensions vs. operating frequency plot indicates a little discernable pattern to the optimal width as the design frequency changes. The critical frequency will be explained more in chapter five of this dissertation.

The fractional bandwidth (FBW) vs. operating frequency plot shows that the FBW reaches the maximum at some points in the interesting band ($92.5 \leq fo \leq 98.5$GHz), close to the critical frequency (f_c=94.5 GHz). At frequencies above or below these frequencies, the FBW decreases. This is because the bandwidth (BW) is directly proportional to the antenna's height to wavelength ratio (h/λ). Besides, two resonates frequencies at operating frequencies above or below the f_c, but, at the $f_o = f_c$, the two resonates frequencies are overlapped. We conclude that as the two resonant frequencies moving away in the opposite direction, the FBW becomes narrower.

Question 3.2: Over what frequency range the linear polarized radiation can be achieved by only optimizing the antenna and the package dimensions? Also, what are the factors that limit the frequency range?

We found out that fixed feed integrated on fixed RFIC chip could be proximity coupled to various patch antennas at different operating frequencies. The frequency range that we achieved is 80.5 GHz to 106.5 GHz. However, some limitations narrow the frequency range. As we observed, the antenna's height is one of the limits—the h_{opt} decreases at frequencies above or below f_c. At the low-frequency range and high frequency, the h_{opt} is very thin—for example, the h_{opt}= 46 µm and 50.4 µm at f_o= 80.5 GHz and f_o= 106.5 GHz, respectively. Very thin substrates may be impractical and limit the ability to match the antenna without feed modifications. This limitation allows the frequency to be tuned over a more comprehensive frequency range within h_{opt} > 50 um. The antenna's impedance frequency bandwidth is another limit to the operating frequency range because the frequency bandwidth decreases at the lower and higher f_o in the range of interest. The fractional bandwidth is 1 % and 1.6 % at f_o= 82.5 GHz and f_o= 106 GHz, respectively.

Question 3.3: How is the antenna sensitive to its dimensions? We will study which of the antenna's dimensions (L_p, W_p, h) affect input impedance matching performance between the antenna and the fixed feed line?

The proximity coupled patch antenna is sensitive to its height and length only. The sensitivity analysis results show that the patch antenna's length and height significantly affect the impedance matching at a specific operating frequency. On the other hand, the antenna's width has less impact on the patch antenna's impedance matching performance. This behavior is expected from the patch antenna.

Question 3.4: Can these results be fit in equations? Polynomial equations are used of the EMC microstrip antenna, and the feed line is generated to provide quick estimates of the antenna's dimension.

We could fit the optimized antenna's dimension vs. operating frequency results in characteristic geometric equations. These equations correlated the optimized antenna dimensions to its f_o. The generated equations are applied to estimate antennas' dimensions at different operating frequencies (78 GHz, 94 GHz, and 107 GHz). The results show that this analysis gives good start values for the antenna's dimensions even with frequencies outside the interesting band.

3.7 Summary

In this section, an analysis is generated to predict the range of the operating frequencies that can be achieved by coupling the linear polarized antenna to the fixed feed line integrated on a fixed RFIC chip. A low-cost and high-performance antenna can be generated. The generated analysis is applied to estimate antennas' dimensions at different operating frequencies (78 GHz, 94 GHz, and 107 GHz). The results show that this analysis gives good start values for the antenna's dimensions. This analysis indicates that linear polarized radiation can be achieved by only optimizing the antenna and the package dimensions over a wide frequency range. However, some limitations narrow the frequency range.

Until this point, simulation analysis has been used to test the generated analytic model. In this analysis, we study the relationship between the antenna's dimensions and the operating frequencies when changing the antenna's substrate and length of the feedline (L_c).

CHAPTER 4: Circularly Polarized Fixed Fed Patch Antenna

4.1 Introduction

Linear polarized antennas require to transmit and receive antennas to be of the same polarization, hence require accurate alignment of the antennas. Circular Polarized antennas allow signal reception irrespective of the receive antenna's orientation concerning the transmit antenna and can suppress multipath interference. Circularly polarized microstrip patch antennas are widely used in portable/ handheld devices, such as RFID reader antennas, WLAN, GPS, rectenna for energy harvesting, and mobile phone antennas [49]–[54].

In this chapter, analyses are provided to understand the CP patch antenna's behavior in the fixed feed case at different operating frequencies. We will focus on developing research that studies how the antenna's dimensions change with operating frequencies in different situations like changing the substrate material. This understanding of CP patch antenna behavior helps us give a quick estimation for circularly polarized antenna's dimensions values and define the limits of generating CP with a fixed feed line.

Circular polarization can be generated if two orthogonally polarized modes are excited with a 90^0 time-phase difference between them and their amplitudes are equal. This can be achieved by adjusting the patch antenna's physical geometry and using either one or two feed lines. A dual-orthogonal fed circularly polarized patch antenna needs two independent sources or a power divider with 90 degrees offset RF output to excite two orthogonal modes with equal amplitude but in phase quadrature. However, the dual orthogonal feed lines technique prevents us from using the same passive feed structure for linear and circular polarization designs. Moreover, the power divider is complicated and power-consuming. In addition to dual-orthogonal feeds, the single feed also can obtain circular polarization. The patch antenna is fed at a single point that excites two orthogonal degenerate modes with equal amplitudes. By applying a proper design to create an asymmetry in the cavity, the field of one mode can lead by 45^0, while the field of the other mode can lag 45^0. Thus, the phase difference between the modes is 90^0, which is necessary for circular polarization. To create a single-fed circularly polarized patch antenna, several methods have been developed. The three commonly used methods to produce a nearly circular polarized patch antenna are a slightly off-square diagonal fed patch, a square patch with notches, and a square patch with the diagonal slot, as shown in **Figure** 4.1.

The disadvantage of the slightly off-square patch method is that it is difficult to insert the

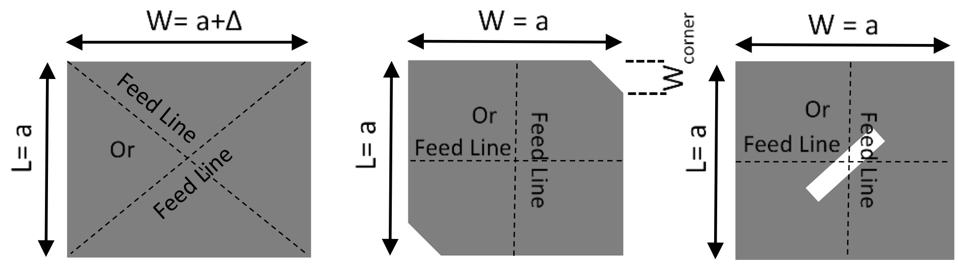

a. Slightly off-square patch b. Square patch with notches c. Patch with slot

Figure 4.1 Single-feed arrangements for circular polarization of rectangular patch antenna.

antenna symmetrically with the feed line's center with proximity coupled feed line type. This complicates the fabrication process—See **Figure** 4.2 for more illustration. The patch with slot method has a significant tradeoff between VSWR and axial ratio value when choosing the feed line's location [54]. As a result, we selected the patch antenna with a notch, shown in **Figure** 4.3, from the three single-feed arrangements to generate circular polarization as the first choice to start.

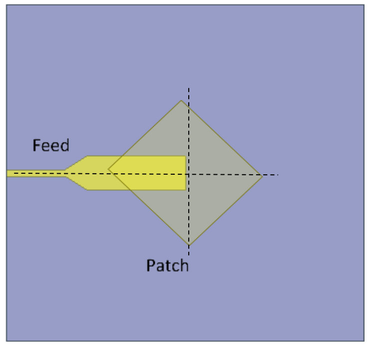

Figure 4.2 Slightly off-square proximity coupled patch antenna.

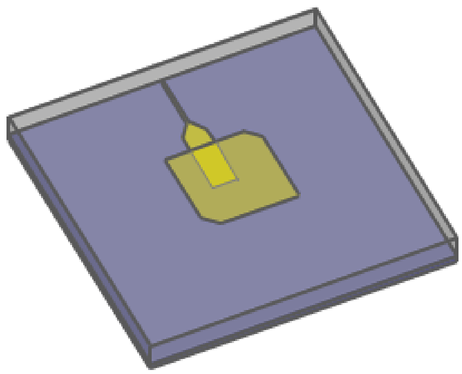

Figure 4.3 Circularly polarized proximity coupled patch antenna with the notch.

4.2 Research Questions

This chapter aims to create an uncomplicated analysis to provide us with a good understanding of the CPPA's dimensions behavior at different operating frequencies. Moreover, this generated analysis gives us a quick estimate of the antenna's dimensions (W_p, L_p,h) at a specific operating frequency (f_o) when coupled to the fixed feed line. This analysis helps us determine whether we can couple a fixed feed line to various LP adaptable antennas at different operating. Additionally, The analysis helps determine the fundamental limitations of the adaptable antenna mounted on top of the fixed RFIC chip. In this chapter, the circularly polarized radiation is studied. The following questions should be answered to achieve our goal:

Question 4.1: How do the CP patch's optimal dimensions vary when coupled to the thin fixed feed line at different f_o? This question helps to study the behavior of the antenna's dimensions at different f_o.

Question 4.2: Over what frequency range the Circularly polarized radiation can be achieved by only optimizing the antenna and the package dimensions? Also, what are the factors that limit the frequency range? We try to create this circular polarization using the same fixed feed line proposed in the linear polarization chapter (chapter 3).

Question 4.3: Can these results be fit in a geometric model? An intuitive model of the EMC microstrip antenna and the feed line is generated to provide quick estimates of the antenna's dimension.

4.3 Optimizing the dimensions of CP single fix fed patch antenna (Lp, Wp, h) across a wide frequency range.

An analysis of circularly polarized proximity coupled patch antenna in the package is investigated to explain the EM behavior between the antenna and transmission line and to provide quick estimates of antenna's dimensions when coupled to the fixed tapered feed line. In this analysis, the feed line is set to its original value (L_c=690 µm, W_c=250 µm)[1], and the patch geometry and mold height are variable. The feed line substrate is silicon dioxide (SiO2). The axial ratio (AR) and input impedance match (return loss S_{11}) should be optimized together for effective circular polarization. The axial ratio is equal to one (0dB) for perfect circular polarization. However, the method used to create CP, which is the patch with a notch, obtains nearly circular polarization, which means AR close to one (AR <2dB). In the numerical analysis, circular polarization is generated by using a single feed.

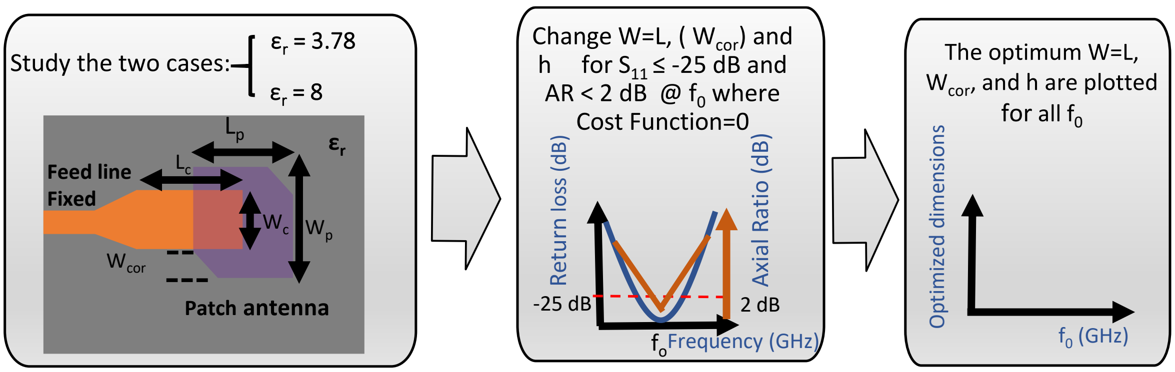

Figure 4.4 Analysis procedure for circular polarization generated by one fix feed line.

The analysis procedure used to achieve CP radiation across a wide range of operating frequencies is similar to the linearly polarized patch antenna's procedure. Nonetheless, the axial ratio performance will be considered, too, with the input impedance matching performance. The procedure is as the following: the sequential nonlinear programming optimizer (Gradient) is run using HFSS software to fund the optimal width (W_{opt}), length (L_{opt}), and height (h_{opt}) of the antenna, where the reflection coefficient is low ($S_{11} \leq -25$ dB) and the axial ratio is close to one (AR<2 dB) at the several operating frequencies f_0 in W band (80.5 GHz to 106.5GHz). The procedure used in this analysis is shown in **Figure** 4.4. The cost function is equal to zero when the two conditions are satisfied. All these optimization simulations in HFSS are conductive at a certain operating frequency (f_o) to reduce the simulation time. In other words, the AR and S_{11} are optimized at specific f_o, not over bandwidth. Moreover, we do not target specific applications that required certain bandwidth for AR or S_{11}. Also, the goal of this study is not to optimize the BW.

The cost function used in the optimization analysis is:

Condition 1 (P1): $\boldsymbol{AR \leq 2dB}$

$$\text{P1}= \begin{cases} \mathbf{0} & \boldsymbol{if}\ \left[\left(\frac{\text{AR}}{2\ \text{dB}}\right)-1\right] \leq 0 \\ \left[\left(\frac{\boldsymbol{AR}}{\boldsymbol{2\ dB}}\right)-\mathbf{1}\right] & \boldsymbol{if}\ \left[\left(\frac{\text{AR}}{2\ \text{dB}}\right)-1\right] > 0 \end{cases}$$

Condition 2 (P2): $\boldsymbol{S11}$ $(\textbf{reflection coefficient}) \leq \boldsymbol{-25dB}$

$$\text{P2}= \begin{cases} \mathbf{0} & \boldsymbol{if}\ \left[\left(\frac{25\ \text{dB}}{\text{RL}}\right)-1\right] \leq 0 \\ \left[\left(\frac{\mathbf{25\ dB}}{\mathbf{RL}}\right)-\mathbf{1}\right] & \boldsymbol{if}\ \left[\left(\frac{25\ \text{dB}}{\text{RL}}\right)-1\right] > 0 \end{cases}$$

Cost function = P1+P2=0

In this numerical analysis illustrated in **Fig**. 4.4, two cases are investigated. The simulation is run for two different antenna substrate materials (ε_r=3.78 and ε_r=8) coupled to a fixed tapered feedline. The first substrate is quartz (ε_r= 3.78), which is the original design. We selected a high dielectric constant value (ε_r= 8) for the second case to compare it with quartz's dielectric constant

value (ε_r=3.78) to understand the relationship between the material's dielectric constant and optimal antenna dimensions.

Result and Discussion:

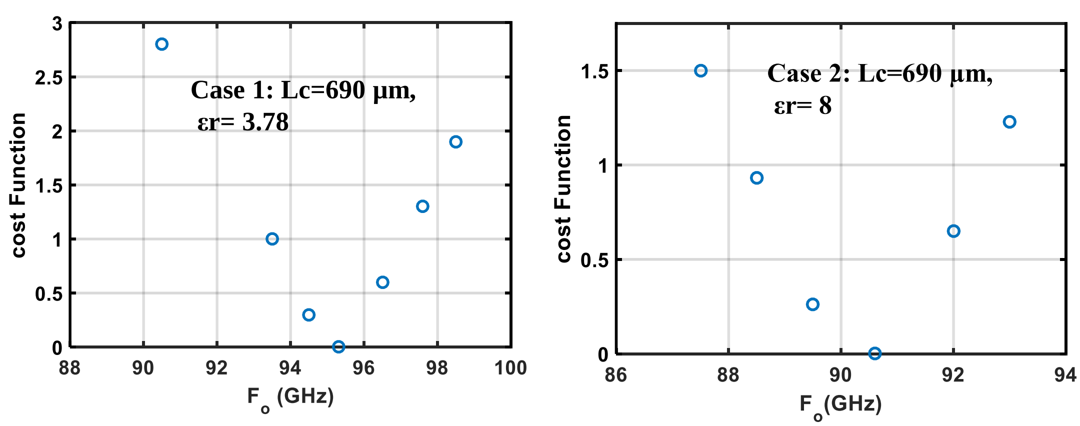

Figure 4.5 Cost function vs. operating frequency for the three different cases.

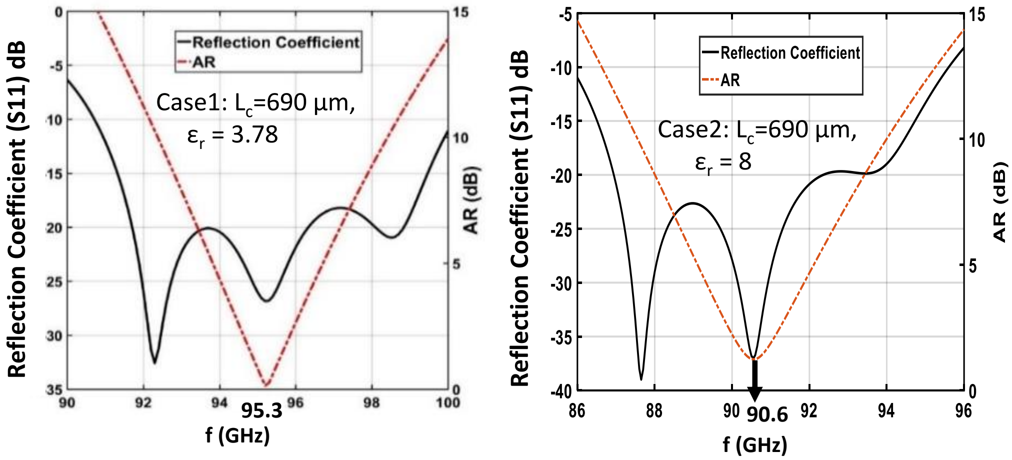

Figure 4.6 Reflection coefficient and axial ratio vs. frequency at the f_o for the two different cases.

The optimization analysis is run, and the results are presented in **Figure** 4.5 and **Figure** 4.6. **Figure** 4.5 shows the cost function vs. fo at the two different antenna substrate materials (ε_r=3.78 and ε_r=8). We notice that the optimization analysis's cost function is zero only around the specific operating frequency, which is f_o=95.3 GHz for ε_r=3.78 case and 90.6 GHz for ε_r=8 case. The result in **Figure** 4.6 shows the reflection coefficient and axial ratio (AR) vs. frequency at the only operating frequency where the cost function= 0 for the two cases. As we observed, with a single fixed feed, it is challenging to create circularly polarized patch antennas coupled to a fixed feed line over a band of frequencies. However, in Chapter 3, we could optimize the LP patch antenna's dimensions at various operating frequencies (f_o). The cost functions are zero at these different operating frequencies (f_o).

Moreover, we can observe from the cost function vs. fo results in **Figure** 4.5 that the operating frequency 95.3 GHz, where the coat function=0 for the original design case (quartz substrate) is close to the critical frequency (f_c=94.5 GHz). The original design case has been investigated in Chapter 3. On the other hand, the high dielectric material case (ε_r=8) has not been studied in Chapter 3, so we want to investigate if operating frequency (f_o) 90.6 GHz, where the cost function equals zero, is close to the fc of this specific case. Thus, we run the LP optimization analysis in Chapter 3 for the high dielectric case at a few operating frequencies near 90.6 GHz to find the f_c, where only one resonant frequency. The simulation is run to find the antenna's optimal dimensions at few operating frequencies around 90.6 GHz (89 GHz to 92 GHz). The reflection coefficient vs. frequency at the three operating frequencies (89 GHz, 90 GHz, 91 GHz, and 21 GHz) is shown in **Figure** 4.7. We observe from these results that the f_c is 90 GHz for ε_r=8 case, close to 90.6 GHz. Table. 4.1 shows the single operating frequency where the cost function equals zero and fc in each case.

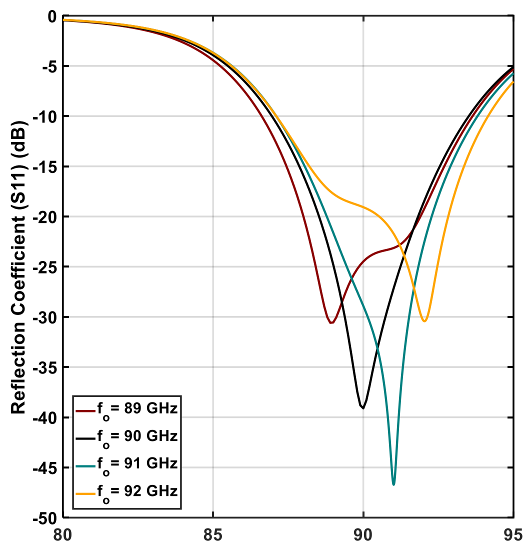

Figure 4.7 Reflection coefficient vs. frequency at 89, 90, 91, and 92 GHz for ε_r=8 case.

Table 4.1 Critical frequencies and the single operating frequency at different cases.

Case number	**Dielectric constant ε_r**	**Critical Frequency f_c (GHz)**	**Operating Frequency (GHz)**
1 (Original design)	3.78	94.5	95.3
2 (change ε_r)	8	90	90.6

Additionally, we show the reflection coefficient and AR vs. frequency result at operating frequency (f_o) 92 GHz where the cost function does not equal zero for case study 2 (ε_r=8) in **Figure** 4.8. The minimum cost function at f_o=92 GHz is 0.65.

In conclusion, we could not achieve circularly polarized radiation over a broadband of operating frequencies by coupled the antennas to a fixed feed line. We can only get the circularly polarized patch antenna's dimensions at a few operating frequencies around the critical frequency.

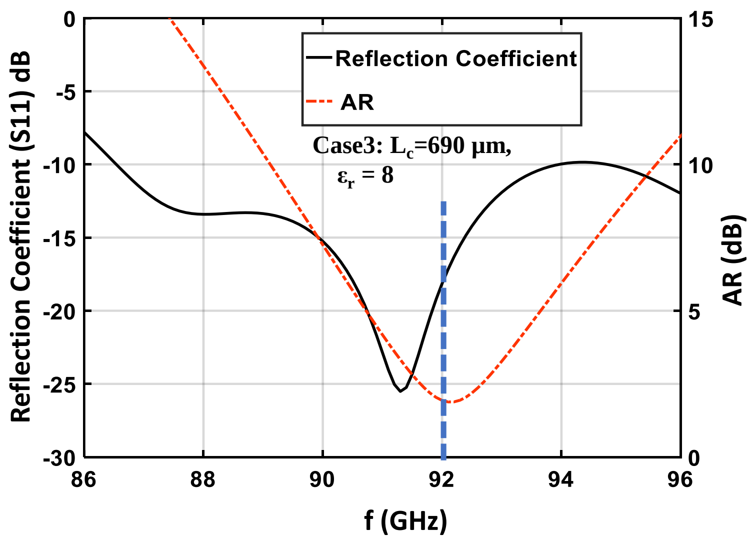

Figure 4.8 Reflection coefficient and axial ratio vs. frequency at the f_o= 92 GHz for the studied case-2.

Furthermore, We used the other methods, which are slightly off-square patch and square patch with notches, to produce a nearly circular polarized patch antenna. However, these CP arrangements' behavior is the same. We still can not create CP radiation by coupled the antenna to a fixed feed line over various operating frequencies.

4.4 Research outcome

This chapter aims to generate a simple analysis to provide quick estimates of the circularly polarized antenna's dimensions (L_p, W_p, W_{cor}, h) at a specific operating frequency (f_o) and understand the CP patch antenna's behavior when coupled to the fixed feed line. The research questions of this chapter are:

Question 4.1: How do the CP patch's optimal dimensions vary when coupled to the thin fixed feed line at different f_o?

Question 4.2: Over what frequency range the Circularly polarized radiation can be achieved by only optimizing the antenna and the package dimensions? Also, what are the factors that limit the frequency range?

Question 4.3: Can these results be fit in geometric equations?

We observe that we can achieve circularly polarized radiation over a very narrow frequency range by optimizing the antenna. We observed from the results of the two study cases (εr=3.78 and εr=8) that we can only have the circularly polarized patch antenna's dimensions at a few operating frequencies around the critical frequency. Therefore, without enough data points, we could not fit the results in equations. The only variables in this analysis were the antenna's dimensions. The feed line's design was not changed.. We need to explore how to achieve our primary objective of this chapter. We hypothesize that the fixed feed line's design limits the frequency range where the CP radiation can be created.

4.5 Summary

This chapter tried to generate some analyses to investigate how the CP patch antenna's dimension varies when it is coupled to a fixed thin feed line at different operating frequencies. Also, we tried to explore the frequency range where the CP radiation can be achieved and the factors that limit this frequency range.

However, we could only obtain a circularly polarized patch antenna at few operating frequencies around the critical frequency with a thin fixed feed. We hypothesize that the design of the fixed thin feed line limits the analysis in this chapter. We will investigate more in modifying the feed line design and how this modification affects the antenna's dimensions behavior and the location of the f_c in the interested frequency band in Chapter 5.

CHAPTER 5: Feed Line Modifications to Extend the Frequency Range of CP Patch Antennas

5.1 Introduction

We investigated designing a single fix fed circularly polarized patch antenna for various operating frequencies in Chapter 4. However, it was challenging to achieve that goal with a fixed feed line because matched circular polarization can be generated only at a few particular operating frequencies around the critical frequency. Changing the antenna's dimensions had little effect on the antenna's performance away from this critical frequency. We hypothesize that the fixed feed line's design limits the ability to match the circularly polarized antenna,

Additionally, in Chapter 3, we find some limitations that narrow the frequency range where a fixed feed line is in proximity coupled to a patch antenna. We observe that the antenna's height is one of the limits. We noticed that the h_{opt} decreases at frequencies above or below f_c. At the low-frequency range and high frequency, the h_{opt} is very thin. Very thin substrates may be impractical and limit the ability to match the antenna without feed modifications. The antenna's fractional bandwidth is another limit to the operating frequency range because the frequency bandwidth decreases at the lower and higher f_o in the range of interest. We also hypothesize that the fixed feed line's design limits the ability to couple the fixed feed line to the linearly polarized antenna at a wide frequency range. We will investigate modifications to the feed line that improve the flexibility of the antenna.

5.2 Review of observed critical frequency

In Chapter 3, when the linearly polarized fixed fed patch antenna was analyzed, the simulation results repeated in **Figure** 5.1 show that the antenna's optimal dimensions (L_{opt} and h_{opt}) change its behavior at a breakpoint, which I call critical frequency (f_c). We observed that the optimal height (h_{opt}) reaches a maximum at the critical frequency (f_c). At frequencies above or below this critical frequency, h_{opt} decreases. The fragile substrate may be impractical and limit the ability to couple the antenna to a fixed feed line. Moreover, the simulation results also show that the patch's optimal length (L_{opt}) is almost constant at frequencies higher than the critical frequency. This is not the behavior expected from a microstrip patch antenna, and $f_o \propto \ 1/L_{opt}$ It is expected instead, as seen at the frequencies lower than f_c. The unusual behavior suggests a second mode is also active in this antenna.

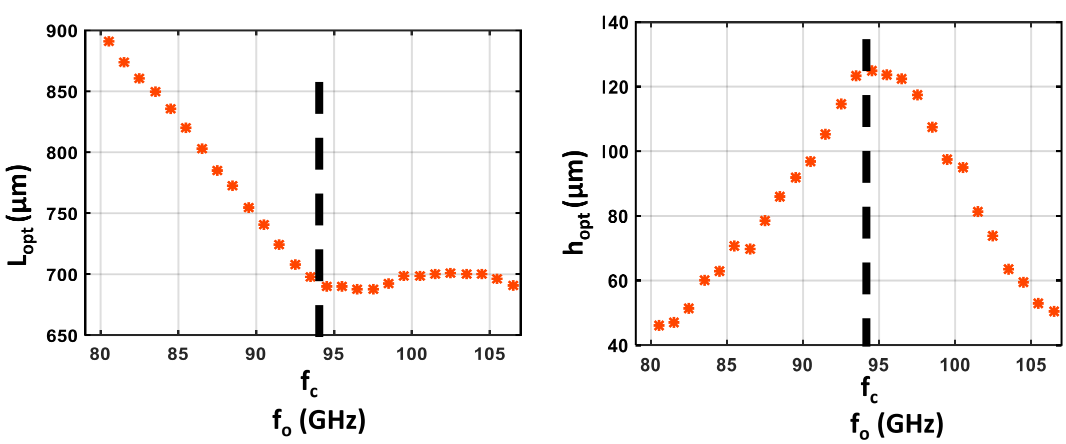

Figure 5.1 Optimal antenna’s dimensions vs. operating frequency.

Moreover, if we look to the return loss vs. frequency at different operating frequencies shown in **Figure** 5.2, we would notice the following: **first, at a frequency higher or lower** than critical frequency, there are two resonant frequencies (f_{r1} and f_{r2}), but one of these frequencies has the lowest reflection coefficient (S_{11}< -25 dB). **Second, at the critical frequency (f_c)**, only one resonant frequency is located at the critical frequency. In other words, f_c is the frequency where the two resonant frequencies are overlapped. These two resonant frequencies are two different modes that are active in this proposed antenna design. Also, at the f_o=f_c= 94.5 when ε_r=3.78, we notice that the L_p = L_c= 690 µm, near a half wavelength at 94.5 GHz. We hypothesize that the taper feed line also radiates, and it may is represented in the second mode. We will investigate that in the next sections.

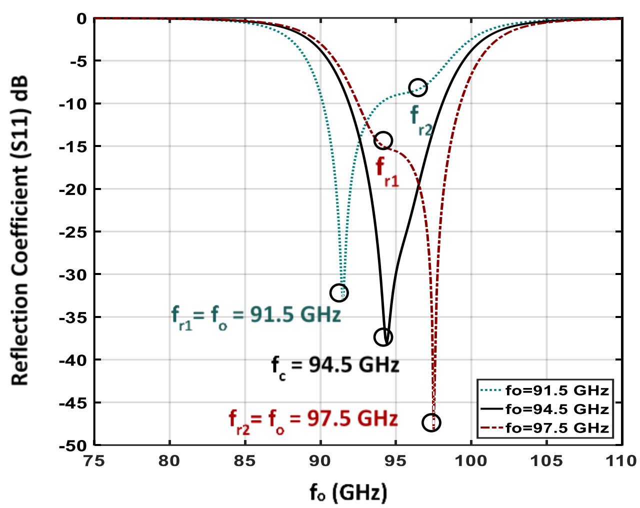

Figure 5.2 Reflection coefficient vs. frequency at three different operating frequencies (91.5 GHz, 94.5 GHz, and 97.5GHz).

The location of the critical frequency in the band of interest is essential to determine the ability to match the antenna without feed modifications over the specified frequency band. We hypothesize that if we shift the location of f_c to be out of the interested frequency range, there will be no changes in the behavior of the antenna dimensions, and there will be only one mode, which has the expected behavior from the microstrip patch antenna.

Table 5.1 Critical frequency at different dielectric constant.

ε_r	2.9	3.78	5	8
f_c (GHz)	98	94.5	93	90

As shown from the analysis in Chapter 3, the dielectric constant (ε_r) of the antenna substrate shifts the critical frequency location about two to four GHz. Table.5.1 shows the f_c at different ε_r. We need to find a way to change the location of f_c other than changing the dielectric constant (ε_r) because changing the ε_r is insufficient. One possibility is to change the feed line itself. The feed line's design has not been changed in the previous studies in Chapters 3 and 4, so in this chapter, we will be exploring how changing the feed line design affects the location of the f_c.

This analysis includes studying the impact of changing the flared feed line's dimensions (L_c and W_c) on the proximity coupled patch antenna. In addition to changing the flared feed line's dimensions, removing the removing the flared part (taper) also will be explored in this chapter.

5.3 Research Questions

This dissertation's primary focus is to investigate the ability to couple adaptable proximity coupled antennas at different operating frequencies to the fixed feed line for adjustable mm-wave antenna-in-package design. To understand the design space and provide quick estimates of the antenna's dimensions at a specific operating frequency (f_o), an intuitive analysis of proximity coupled patch antenna and the fixed feed line is needed. However, there are challenges we faced in Chapter 4 that prevent us from accomplishing the primary goal. In the introduction section of this chapter, we explain the difficulties encountered in the previous chapters (three and four). The influence of changing the feed line design on creating linear or circular polarization at various operating frequencies is needed to be studied.

The following questions are required to be answered to reach the main goal:

Question 5.1: How do the taper feed line's dimensions affect PCPA behavior, with a particular focus on the location of the critical frequency in the interested frequency range? We hypothesize that the length L_c of the taper has a significant effect on the critical frequency location.

Question 5.2: Can the feed line be modified to move or eliminate the f_c characteristics observed in Chapters 3 and 4? If the answer is yes, the following question will need to be answered:

Question 5.2.1: Over what frequency range can the circularly polarized radiation be achieved by only optimizing the antenna and the package dimensions with the modified feed line?

Question 5.2.2: Over what frequency range the linearly polarized radiation can be achieved by optimizing the antenna and the package dimensions with the new modified feed line?

5.4 Effect of the feed line on the Critical Frequency

We hypothesized that the flared feed line's dimensions, which were near a half wavelength at 94.5 GHz, were closely connected with the location of the critical frequency in this design. To examine our hypothesis, the effect of the feed line's dimensions on the LP proximity coupled patch antenna is studied. We want to determine the impact of changing the feed line's sizes (L_c and W_c) on the critical frequency location. **Figure** 5.3 shows the proposed proximity coupled patch antenna.

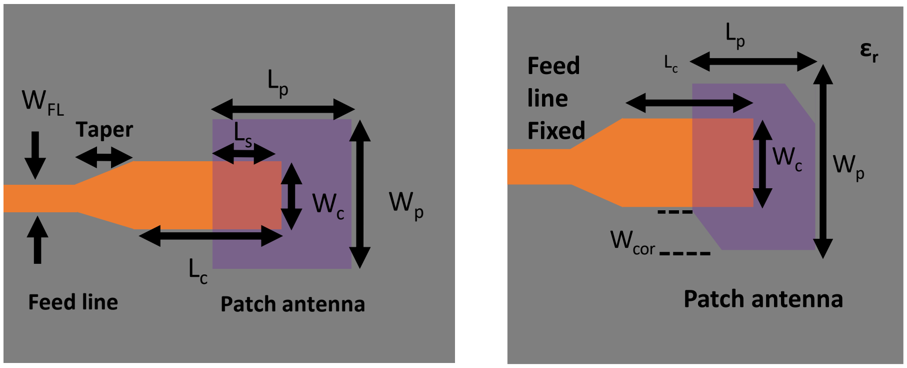

a. Top view of linearly polarized patch antenna   b. Top view of circularly polarized patch antenna

Figure 5.3 The proposed proximity coupled patch antenna.

First, The length of the feed line underneath the antenna (L_c) is changed by $\pm$ 14.5 % of its original value, which is 690 µm [1], (590 µm and 790 µm). The antenna is then optimized across the W-band (80.5 to 106.5 GHz) using the same LP antenna optimization procedures as in Chapter 3. **Figure** 5.4 illustrates the analysis procedures. In every case, the dimensions of the antenna (W_{patch}, L_{patch}, and h_{patch}) are optimized for S_{11}<-30 dB at different operating frequencies (f_o). Then, the optimum W_p, L_p, and h are plotted for all f_o.

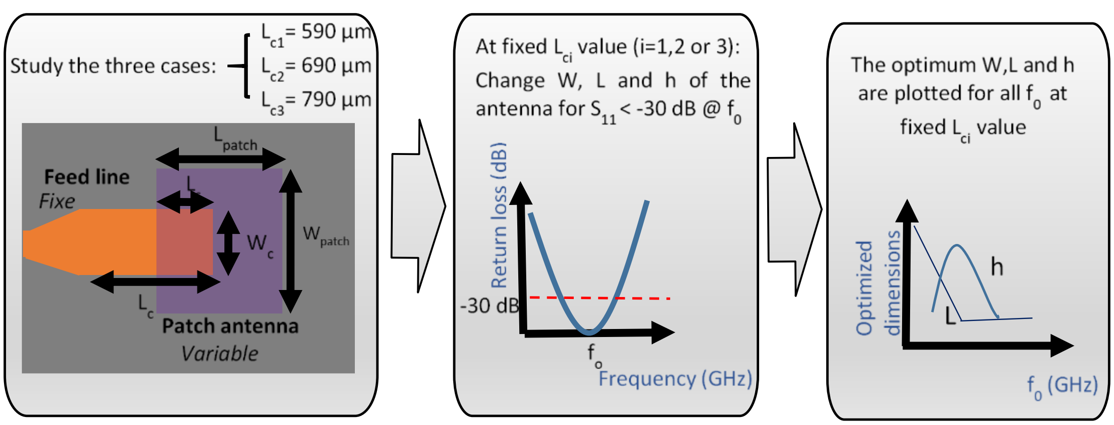

Figure 5.4 Analysis Procedures of optimizing the LP patch antenna'dimension at different feed line length (L_c).

Results and Discussion:

The optimal antenna dimensions vs. operating frequencies at different feed line lengths (L_c) is shown in **Fig**. 5.5. The optimization results indicate that changing the feed line length (L_c) shifts the critical frequency location. Table 5.2 gives the observed values of critical frequency for each feed. We notice that a 14.5% increase in L_c's value (L_c=790µm) moves the critical frequency's position from 94.5 GHz to 84.5 GHz, which is about an 11% percent decrease in f_c. On the other hand, we observe that a 14.5% decrease in L_c's value (L_c=590µm) moves the critical frequency's position from 94.5 GHz to 108.5 GHz, about a 15 % percent increase in f_c.

Moreover, we observe that the L_{patch} at f_c is equal to L_c, and the L_{patch} stays almost constant at frequencies higher than the f_c. This observation indicates that the second mode is related to the feed line being radiated, and the flared feed line's length is near a half wavelength at the critical frequency. Thus, the feed line acts as a thin patch antenna.

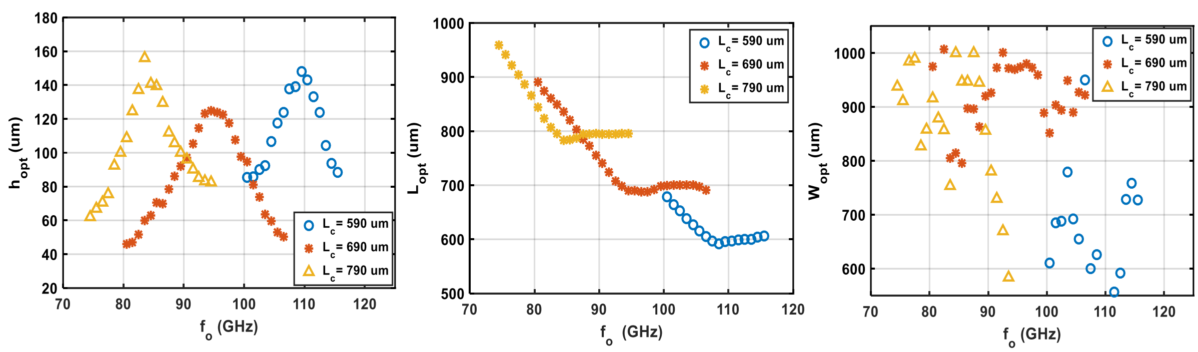

Figure 5.5 Optimal antenna's dimensions vs. operating frequency.

Table 5.2 The value of the critical frequency at different L_c values.

Lc (µm)	**Critical Frequency (GHz) (f_c)**	**L_{patch} @ f_c (µm)**
590 (-14.5%)	108.5 (+11%)	591.3
690 (original value) [1]	94.5	690
790 (+14.5%)	84.5 (-11%)	783.6

Next, the width of the feed line (W_c) underneath the antenna is changed by a ± 10% of its original value, which is 250 µm (225 µm and 275 µm). The antenna is then optimized across the W-band (80.5 to 106.5 GHz) using the same LP antenna optimization procedures as in Chapter 3 for the fixed new W_c value.

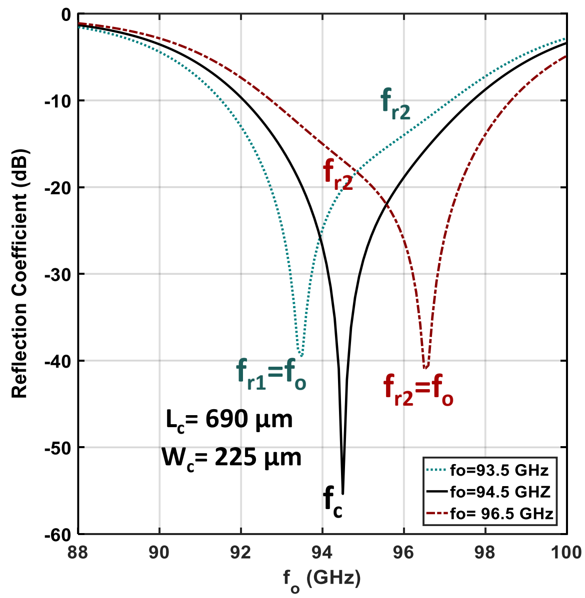

Figure 5.6 Reflection coefficient vs. f at W_c=225 µm.

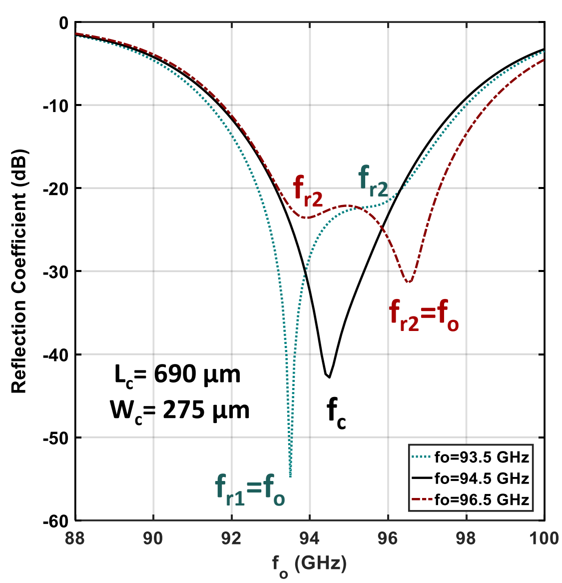

Figure 5.7 Reflection coefficient vs. f at W_c=275 µm.

The reflection coefficient vs. frequencies curves at different feed line' widths W_c=225 μm and W_c=275 μm are shown in **Figure** 5.6 and **Figure** 5.7, respectively. Each figure shows three optimized antennas at three different operating frequencies, one at the critical frequency, two around the critical frequency. **Figure** 5.6 and 5.7 show that the two cases' critical frequencies (W_c=225 μm and W_c=275 μm) are 94.5 GHz, where there is only one resonant frequency in S_{11} vs. frequency plot. This result indicates that the critical frequency location is not affected by the feed line's width (W_c) underneath the antenna. See Table.5.3 for more explanation. We expect this result because the microstrip patch antenna's operating frequency depends on the patch's length.

Table 5.3 The value of the critical frequency at different W_c values.

Wc (μm)	**Critical Frequency (GHz) (f_c)**	**L_{patch} @ f_c (μm)**
225 (-10%)	94.5	699.1
250(original value) [1]	94.5	690
275 (+10%)	94.5	681

These analyses show that the feed line's length underneath the antenna (L_c) significantly affects the critical frequency position. The feed line's length underneath the antenna (L_c) is near a half wavelength at the critical frequency and frequencies > f_c. Thus, the second mode is related to the thin feed line's radiation, and its radiation affects the proximity coupled patch antenna behavior. This confirms our hypothesis that the half-wave resonant is set up on the taper feed stub, and the presence of the additional resonant creates the critical frequency effect.

We hypothesize that the second mode, which is affected by the feed line, will move to a very low frequency as the fed line's length increases. Thus, the critical frequency will not exist in the interested frequency range (W-band). To achieve this goal, we increase the feed line's length underneath the antenna to be equal to the whole feed line. Thus, the flared feed line will be removed to ensure that the second mode is out of the interested frequency band. In the next section, I will discuss the effect of eliminating the taper from the feed line.

5.5 Effect of removing the taper section from the feed line

In the previous section (5.4), we observed the effect of the taped feed line's dimensions on shifting the critical frequency location in the interested frequency band range. We hypothesize that the second mode will move to a very low frequency as the fed line's length increases. Thus, we will remove the taper section from the feed line to ensure that the second mode is out of the interested frequency band by increasing the feed line's length underneath the antenna. Moreover, we have to keep the feed line's impedance equal to 50 ohms as a given value in the previous chapters. However, the 50 ohms feed line's width (W_{FL}) is 16.3 μm with a thickness equal to 9.25 μm (see **Figure** 5.3). The feed line' width (W_{FL}) is very narrow, so the coupling between the antenna and the feed line will be weak. As a result, we increase the feed line's width, but we keep its impedance equal to 50 ohms. Also, the feed line will still be fabricated on a SiO2 substrate (ε_r=4). Increase the height and the width of the feed line to be 50 ohms. But, we have to consider the effect of the surface wave as the feed line's substrate height increases. The new feed line design will be called the straight feed line.

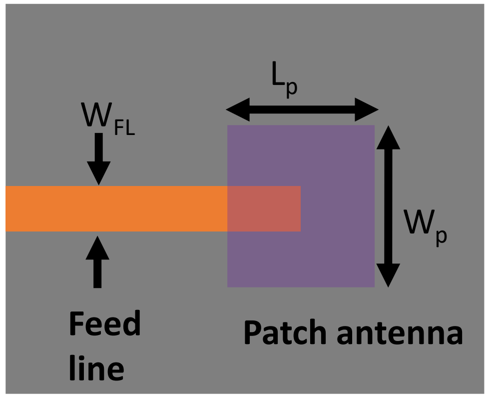

Figure 5.8 The straight feed line design.

The new feed line dimension, which is named the straight feed line, is given in Table 5.4.and the design of the straight feed line is presented in **Figure** 5.8. The new feed line has dimensions W_{FL}= 59 µm and h_{FL}= 40 µm. It is fabricated on SiO2 substrate (ε_r=4).

Before using the new suggested design of the feed line for circularly polarized patch antenna analysis, we will first simulate for linearly polarized patch antenna to check the second mode's existence in the interested band of frequencies (80 GHz to 110 GHz). As explained earlier in Chapter 3, we optimize the LP antenna at different operating frequencies (91.5 GHz, 94.5 GHz, and 97.5GHz).

Figure 5.9 shows the reflection coefficient vs. frequency of the optimized design at three different operating frequencies (91.5 GHz, 94.5 GHz, and 97.5GHz) for both new and old feed line designs. We can observe that the dispersant of the second resonant frequency. Thus, we will use the new suggested design to feed the patch antenna instead of the old design.

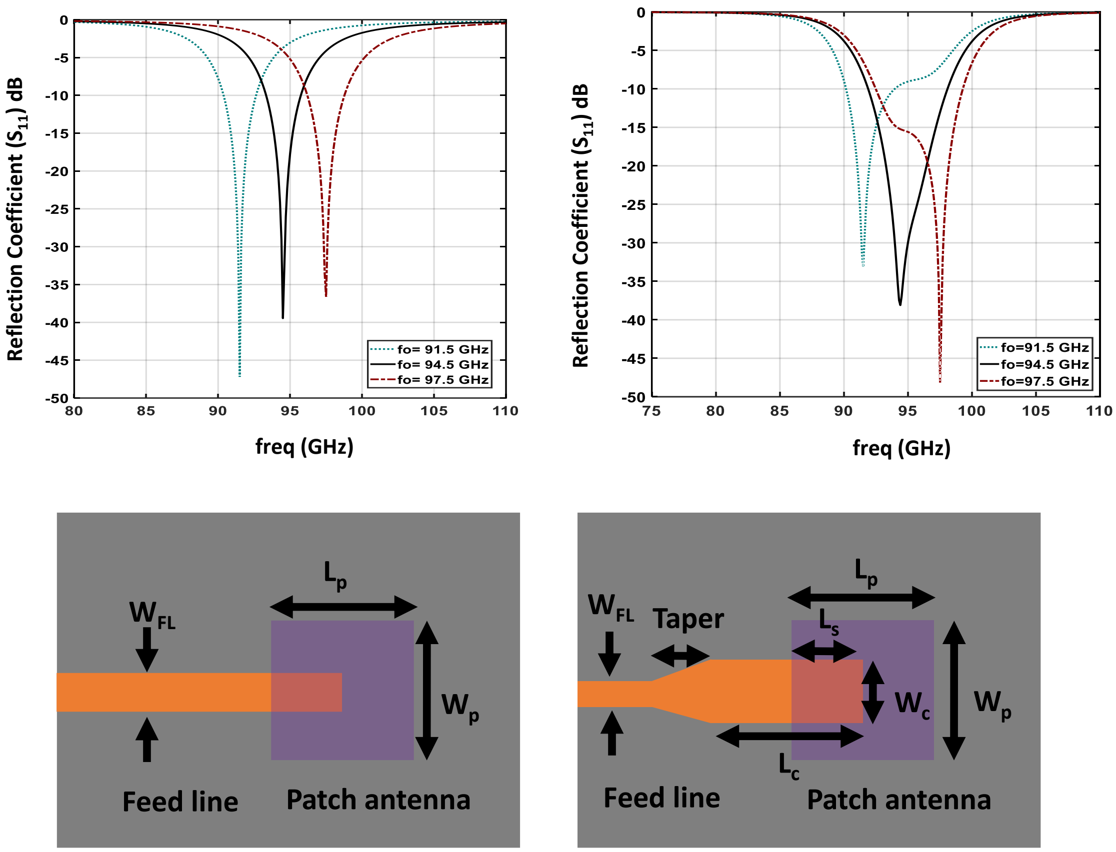

a) b)

Figure 5.9 Reflection coefficient vs. frequency at three different operating frequencies (91.5 GHz, 94.5 GHz, and 97.5GHz) a. for the new feed line design b. for old feed line design.

5.5.1 Circularly polarized patch antenna

The new design of the feed line, "a straight feed line," as I name it, will be used to achieve circularly polarized radiation over a wide frequency range by optimizing the antenna and fixed the feed line. **Figure** 5.10 shows the new proposed design for the feed line. These optimization studies will help us to achieve the primary goal of Chapter 4. The goal is to create a simple analysis that provides quick estimates of the antenna's dimensions at a specific operating frequency (f_o) and understand the antennas' behavior coupled to the fixed feed line. This fixed straight feed line will be coupled to the circularly polarized patch antenna.

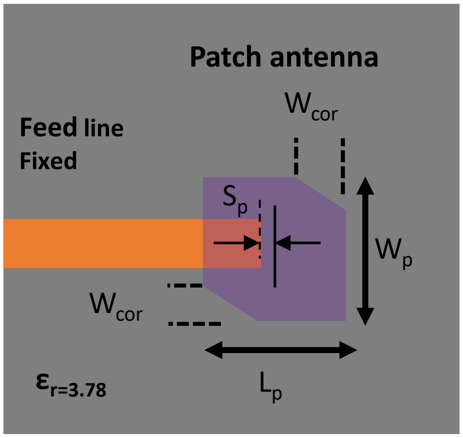

Figure 5.10 The new proposed design of Circularly polarized patch antenna.

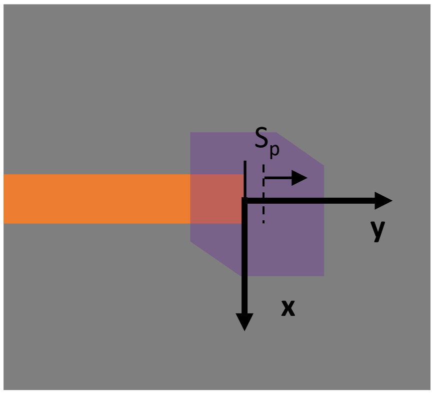

Figure 5.11 CP patch antenna.

A patch antenna with a notch (see **Figure** 5.10) is chosen to generate circular polarization, as been used in chapter 4. The variable patch dimensions are W_{cor}, height (h), and L_p. The patch will also be shifted to the positive of the x-axis by S_p. **Figure** 5.11 illustrates the variable values.

The analysis procedure is used to achieve the target is similar to the processes that have been used for the Circularly polarized patch antenna in Chapter 4. At the optimal dimensions (W_{opt} =L, W_{cor}, h_{opt}, and S_{p_opt}) of the antenna, the reflection coefficient is low ($S_{11} < -30$ dB), and the axial ratio is close to one (AR< 2 dB) at the several operating frequencies f_0 in W-band. The procedure used in this analysis is shown in **Figure** 5.12. The cost function is equal to zero when the two conditions are satisfied.

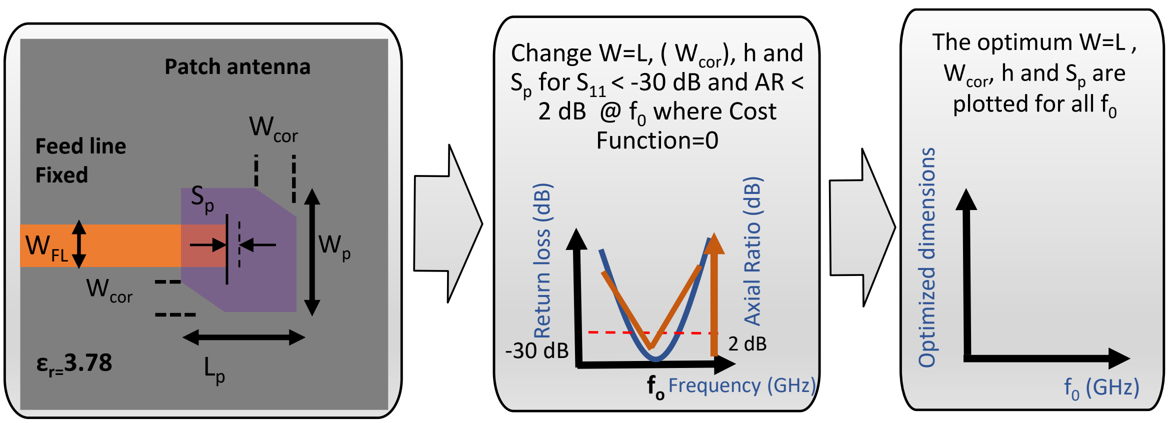

Figure 5.12 Analysis Procedure for Circular Polarization generated by straight fix feed line.

In this numerical analysis illustrated in **Figure** 5.12, the simulation is run for a patch antenna integrated on a thick quartz substrate (ε_r=3.8) coupled to a fixed feed line length. The dimensions of the patch antennas are variable (W_{cor}, h_{patch}, and W_{patch}). Furthermore, the patch will be shifted to the positive y-axis of the feed line. See **Figure** 5.11 for illustration. One difference with this optimization is that a new variable is introduced: the shift value to the positive direction (S_p). We did not move the patch in chapter 4 because moving the patch did not affect the optimization analysis in chapter 4. Thus, we did not include it to reduce the number of variables and save time.

Results and Discussion:

As opposed to Chapter 4, we could generate CP antenna designs across an extensive frequency range that met all cost function criteria, AR< 2 dB and S_{11}< -20 dB. The simulation results are shown in **Figure** 5.13. The optimal antenna's dimensions vs. operating frequency plots show that $f_o \propto {}^{1}/_{L_{opt}}$. This is expected from the cavity and TL models analysis, as mentioned in the introduction section in Chapter 3. Moreover, the antenna's dimensions vs. operating frequency plot indicate a little discernable pattern to the optimal width corner (W_{cor}) and height (h) as the design frequency changes. The patch's optimal height is close to the feed line's height value (h_{FL}= 40 μm). Furthermore, the S_{p_opt} vs. f_o plot indicates that the patch location's optimal shift value reaches the minimum amount at the center of the band of interest; at the frequencies above or below the center frequency, the S_{opt} increases.

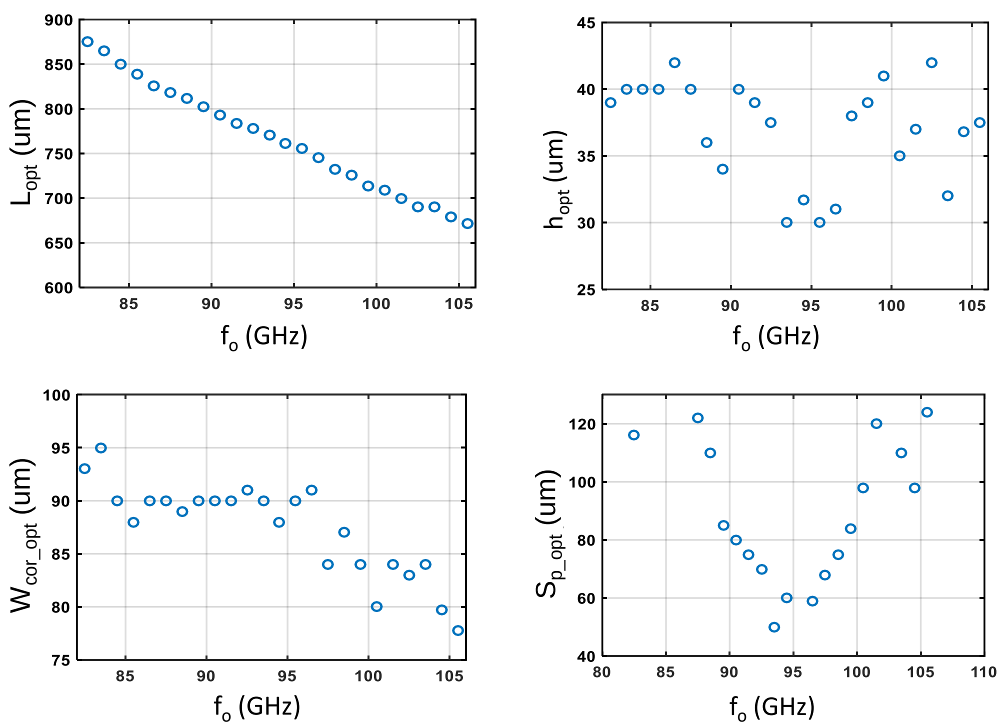

Figure 5.13 Optimal antenna's dimensions vs. operating frequency (f_o) plots.

5.5.2 Linearly polarized patch antenna

The previous section results show that circularly polarized radiation can be generated over a wide range of operating frequencies using the straight feed line. Our primary goal is to provide flexibility in various antenna requirements (bandwidth, directivity, polarization) without making any changes in the designed chip (RFIC). The feed line is part of the RFIC chip. Thus, the new feed line design should be fixed and used to feed the patch antenna electromagnetically regardless of the polarization type and operating frequency. We need to rerun the linearly polarized simulation for the straight feed line. The patch geometry and mold height are variable.

The procedure is as the following: finding the optimal width (W_{opt}), length (L_{opt}), and height (h_{opt}) of the antenna, where the return loss is low ($S_{11} < -30$ dB), at several operating frequencies f_0 in W band. The optimizer is run to find L, W, and h where S11< -30dB. These optimal dimensions of the antenna (W_{opt}, $L_{opt,}$ and h_{opt}) are then plotted for all operating frequencies f_0.

Moreover, the 10 dB antenna's fractional bandwidths (FBW) of the antenna are calculated and plotted vs. operating frequency. In the end, we will include the loss effect in this analysis by adding the material loss (loss tangent) and conductivity loss to find the efficiency and realized gain of the antenna. We also will compare the two feed line designs (flared feed and straight feed).

Results and Discussion

The optimized antenna dimensions results are shown in **Figure** 5.14, and we can observe that the operating frequency f_o is inversely proportional to the optimal length of the patch antenna $f_o \propto {}^{1}/_{L_{opt}}$. This is expected from the cavity and TL models analysis, as mentioned in the introduction section of Chapter 3. Moreover, the antenna's dimensions vs. operating frequency plot indicates a little discernable pattern to the optimal width as the design frequency changes. We can also observe from the results that the patch's optimal height is close to the feed line's height value ($h_{opt} \approx h_{FL}$= 40 µm).

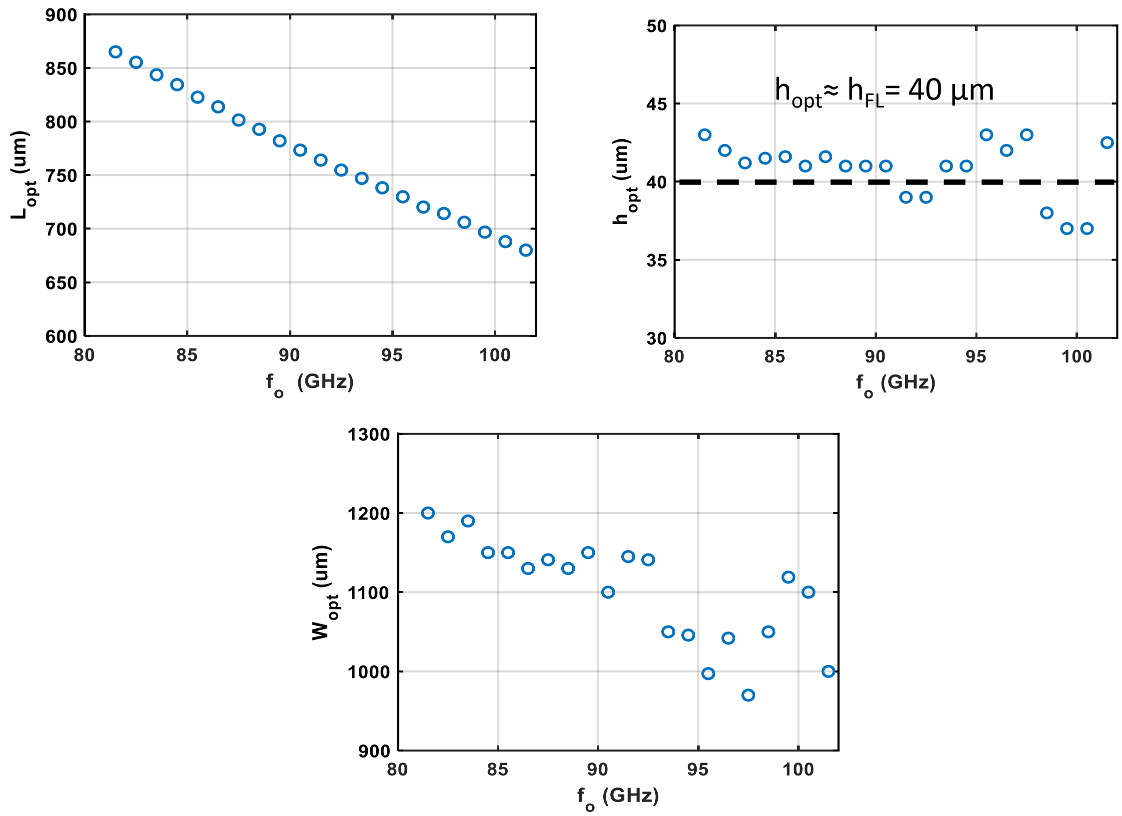

Figure 5.14 Optimal antenna's dimensions vs. operating frequency plots for straight feed line design.

The 10 dB FBW is shown in **Figure** 5.15. For the antennas coupled to the new feed line design (Straight feed line) case, we notice that the 10 dB fractional bandwidth (FBW) without including the loss effect increases with increasing the operating frequency f_o. Still, the bandwidth is narrow for all f_o. The 10 dB BW increases monotonically with thickness. With almost fixed patch height, as the operating frequencies (f_o) increase, the wavelength decreases. Thus, the h_{patch}/λ_g is larger at higher f_o. FBW $\propto \frac{1}{Q} \propto h/\lambda_g$. We plot FBW vs. f_o and h/λ_g vs. f_o in one graph, shown in **Figure** 5.15c. Both plots have the same behavior, FBW and h/λ_g increase as f_o increases.

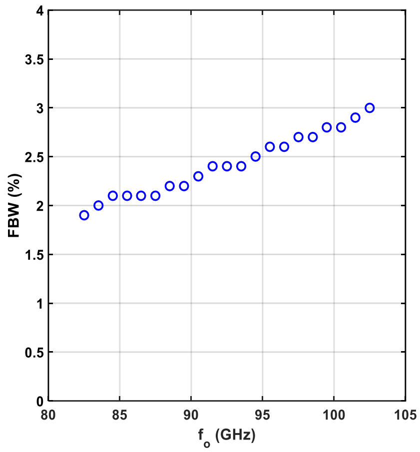

a. Straight feed line design (new)

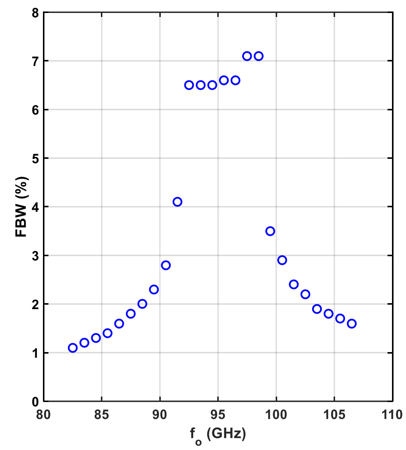

b. Flared feed line design (old)

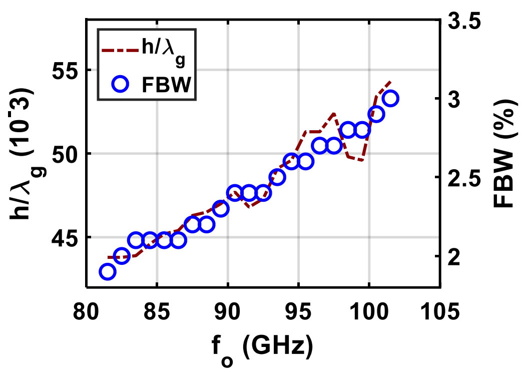

c. FBW and h/λ_g vs. f_o straight feed line case.

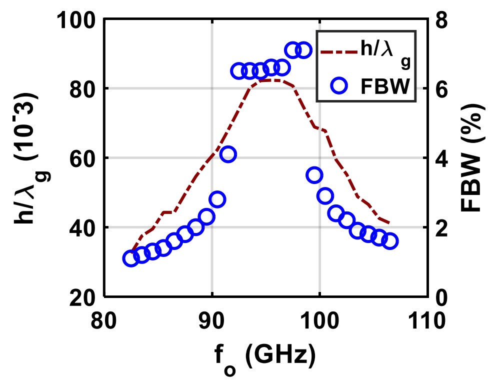

d. FBW and h/λ_g vs. f_o flared feed line case.

Figure 5.15 FBW vs. f_o for both feed line designs.

For antenna coupled to the old feed line design (flared feed line), as I mentioned in Chapter 3, we observe that the FBW reaches the maximum at some points in the interesting band ($92.5 \leq fo \leq 98.5$GHz), close to the critical frequency (f_c=94.5 GHz). See **Figure** 5.15b. At frequencies above or below these frequencies, the FBW decreases. As the antenna's height to wavelength ratio (h/λ_g) increases, the FBW increases, and the reverse is true. Also, we noticed from the FWB vs. f_o that the FBW decreases dramatically at f_o= 99.5 GHz and f_o= 91.5 GHz. We conclude that as the two resonant frequencies moving away in the opposite direction, the FBW becomes narrower.

Figure 5.15d shows the FBW and h/λ_g vs. fo for flared feed line design. The 10 dB bandwidth of the old feed line design is higher than the new one.

After including the loss effect, the antennas' efficiency and realized gain coupled to new and old feed line designs at different f_o are presented in **Figure** 5.16 and **Figure** 5.17, respectively. The antenna realized gain and efficiency for antenna coupled to the new feed line design (straight feed line) are almost constant for all f_o and higher than the old feed line design. On the other hand, the antenna efficiency and realized gain of the antenna coupled to the old feed line design are shown in **Figure** 5.17. The antenna realized gain and efficiency also reach a maximum at the frequency equal to 93.5 GHz, close to the critical frequency (f_c=94.5 GHz). The efficiency and the realized gain decrease at frequencies below or above 93.5 GHz. The realized gain drop dramatically at frequencies above 93.5 GHz. Table 5.4 shows the comparison between the two feed lines design.

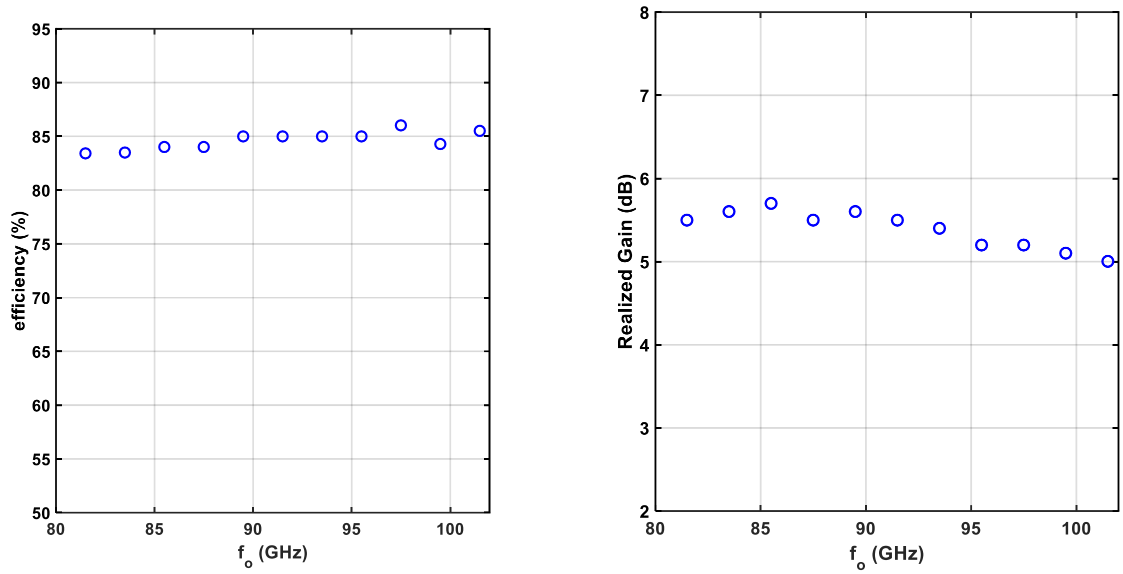

Figure 5.16 Efficiency and Realized gain vs. f_o for straight feed line design with loss effect.

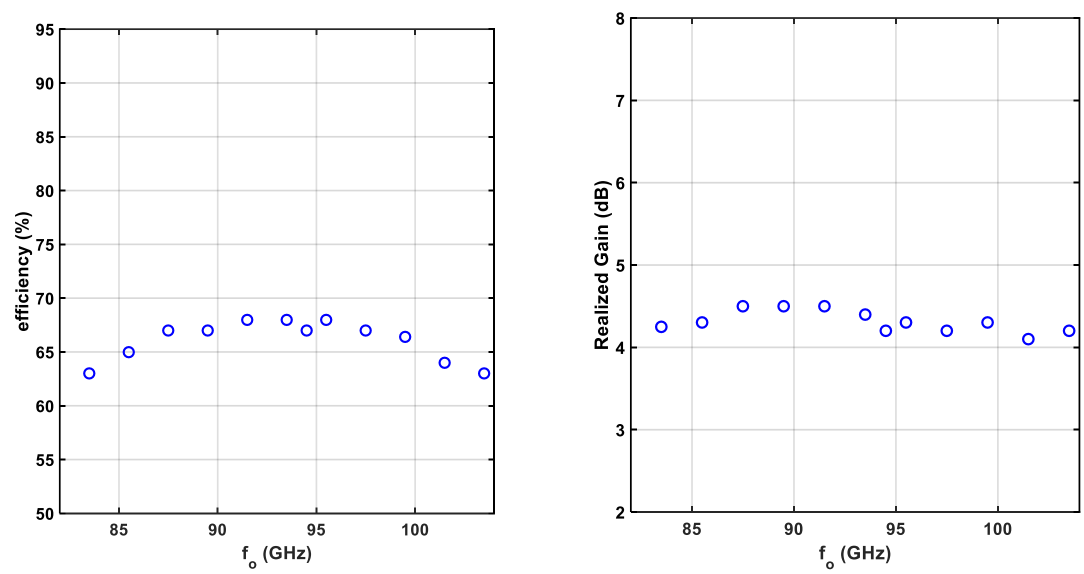

Figure 5.17 Efficiency and Realized gain vs. f_o for flared feed line design with loss effect.

Table 5.4 The comparison between the two-feed line design.

Feed Line	**Straight feed line**	**Flared feed line**
Picture	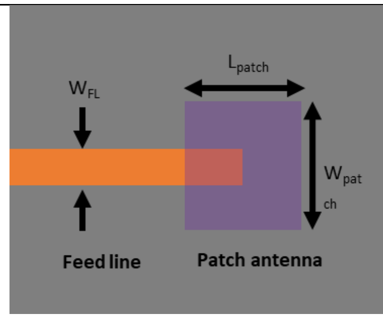	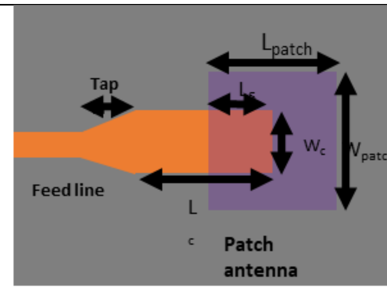
The height of the feed line (h_{TL}) (μm)	40	9.25
The substrate material of the feed line	SiO2	The SiO2 top layer in the RFIC chip
FBW (%)	lower	Higher
Realized Gain (dBi)	Higher	Lower
Efficiency (%)	Higher	Lower

5.6 Research outcome

Based on the primary research questions identified at the beginning of the chapter, the outcomes are listed below:

- **Question 5.1: How do the taper feed line's dimensions affect PCPA behavior, with a particular focus on the location of the critical frequency in the interested frequency range?**

We investigate the impact of the flared part of the feed's line (L_c and W_c) on shifting the location of the f_c over the frequency band. The analysis in section 5.4 shows that the feed line's length underneath the antenna (L_c) significantly affects the f_c position. Thus, the feed line design affects the proximity coupled patch antenna behavior. In **Fig**. 5.5, we observe that as the L_c increases, the f_c shifts to a lower frequency. The flared feed line's length is near a half wavelength at the critical frequency and frequencies > f_c. Thus, the second mode is related to the thin feed line's radiation, and its radiation affects the proximity coupled patch antenna behavior. This confirms our hypothesis that the half-wave resonant is set up on the taper feed stub, and the presence of the additional resonant creates the critical frequency effect.

- **Question 5.2: Can the feed line be modified to move or eliminate the f_c characteristics observed in chapters 3 and 4?**

We analyzed the impact of removing the taper section from the feed line on eliminating the f_c characteristics observed in previous chapters. The f_c is eliminated from the interested frequency band (80.5GHz to 100.6.5 GHz) after the taper was removed. We hypothesize that the second mode will move to a very low frequency as the fed line's length increases. The straight feed line was used instead of the flared feed line. The simulation results in section 5.5 show that only one resonant frequency exists in the interesting range (W-band). Additionally, it shows that circularly and linearly polarized radiation can only be generated by optimizing the antenna and the package dimension with the straight feed line.

We have achieved this chapter's primary aim to examine the ability to couple PCPA at different operating frequencies and polarization to the fixed feed line for adaptable mm-wave antenna-in-package design. Using the straight feed line on a thicker substrate, we could generate linearly and circularly polarized radiation with a fixed feed over a wide frequency range.

5.7 Summary

The feed line's length underneath the antenna (L_c) significantly affects the critical frequency position. Also, we observe from the analysis that the flared feed line's length is near a half wavelength at the critical frequency and frequencies > f_c. Thus, the second mode is related to the thin feed line's radiation, and its radiation affects the proximity coupled patch antenna behavior.

The f_c is eliminated from the interested frequency band (80.5GHz to 100.6.5GHz) after the taper was removed. Using the straight feed line on a thicker substrate, we could generate linearly and circularly polarized radiation with a fixed feed over a wide frequency range.

CHAPTER 6: Proximity Coupled Patch Antenna Array

6.1 Introduction

We discussed linearly and circularly polarized patch antennas at different operating frequencies coupled to a fixed feed line for adaptable mm-wave antenna-in-package design in the previous chapters. This chapter will study arrays of such linearly and circularly polarized patch antenna with a fixed feed structure and their performance across frequency and scan angle.

A patch antenna as a single element provides low gain. However, in many mm-wave applications such as wireless communication, radar, and imaging system, high gain is required to overcome a large amount of path loss and achieve the required adequate isotropic radiated power (EIRP) essential for high data rates. This requirement can be achieved by enlarging the size of the single antenna. Nevertheless, another way to increase the gain without increasing the size of a single antenna is using an array of antennas [5]-[6],[1],[30],[55]. In addition to the high gain requirement for many applications, beam scanning also is demanded. A phased array is very attractive for those applications to get high gain in the desired direction (θ).

Despite common use, the patch antenna has significant mutual coupling effects. This issue leads to scan blindness in many cases. Mutual coupling between antennas is affected by the spacing between antennas and the thickness of the substrate. A way to reduce the mutual coupling is by using a large separating (d) and thinner substrate. However, even with a thin substrate and large separation, there is a mutual coupling. This issue because of the surface wave existence in the substrate. The fundamental surface wave mode (TM_0) has zero cutoff frequency. Therefore, the surface wave always propagates in the substrate. The surface wave's presence increases the mutual coupling between the antenna element in an array leading to scan blindness.

In addition to the mutual coupling and surface wave issues, there is another concern that should be avoided in designing the array, multiple maxima in the radiation pattern. In addition to the maim maximum lobe, another maximum lobe exists in other directions in the radiation pattern. This issue is referred to as grating lobes. This critical issue causes the array to send or receive signals from directions different than the main lobe direction without attenuation.

In this chapter, the scan performance of the antenna elements in an array will be explored. This study will include mutual coupling and grating lobes issues. We will investigate how these issues impact this project's proposed design, a fixed feed lines structure proximity coupled to the patch antennas in an array.

6.2 Research Questions

This chapter's primary goal is to understand the design of linearly or circularly polarized phased arrays coupled to fixed feed lines fabricated on an RFIC chip. Because the feed is fixed, the separation distance between the feed lines (d) is set. The separation distance between the antennas (d) is fixed as well, even as the array must operate over several different frequencies band. Moreover, we want to understand how the fixed array spacing at various operating frequencies (f_o) limits the array scanning. In other words, how is the fixed feed lines structure at different f_o affect the scan angle range?

The following questions will be studied to help us understand the ability to design linearly or circularly polarized phased array coupled to fixed feed lines fabricated on a fixed RFIC chip for different operating frequencies and scan angels:

Question 6.1: How does fixed array lattice impact the circuit parameter of the antenna, such as the mutual coupling and impedance matching, at different f_o for broadside case?

Question 6.2: How does fixed array lattice affect the antenna's radiation parameter, such as sidelobe level and the grating lobe's existence in the radiation pattern, at different f_o for broadside case?

Question 6.3: How is the scanning angle limited by the fixed feed spacing at different operating frequencies? This question helps us explore the limitation in the beam scanning due to the grating lobes' presence and the mutual coupling at fixed array lattice.

We will study these questions for linearly, and circularly polarized patch antenna phased array. The analysis that will be reviewed in this chapter is the H-plane uniform amplitude and spacing array. All the antennas, which are equally separated (d), will be fed to an identical amplitude with a progressive phase shift equal to β between the antennas. For more illustration, see **Figure** 6.1.

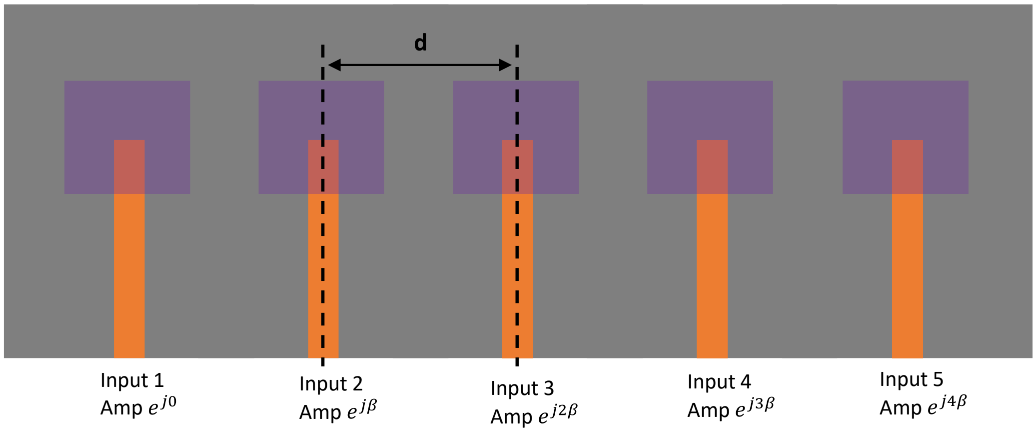

a. Top view of the uniform phased array.

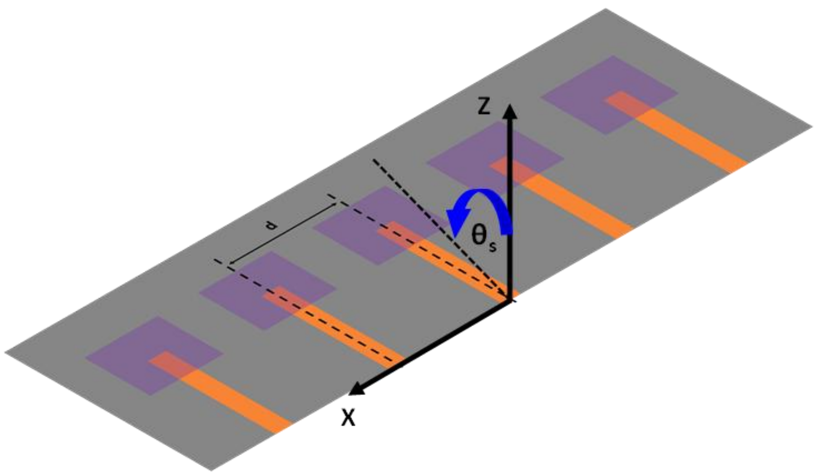

b. Equally spaced five element phased array picture shows the snanning angle (θ_s) direction.

Figure 6.1 Uniform phased five-antenna array.

6.3 Impact of the fixed feed spacing on the performance of the LP phased array

This section aims to study the impact of the separation distance between antennas (d) on an LP phased array's beam scanning performance at different operating frequencies (81.5 GHz to 100.5 GHz) when the antennas are coupled to fixed feed lines. We will study the H-plane five-elements uniform amplitude and spacing array. The antennas are equally separated (d) and fed to an identical amplitude with a progressive phase shift equal to β between the antennas. The array is shown in **Figure** 6.1.

The array factor is given by:

$$AF = A_o \sum_{n=1}^{N} e^{j(n-1)\varphi} \tag{6.1}$$

Where: $\varphi = kd\ sin\ \theta_s + \beta$, N is the number of elements, and d is the spacing distance between antennas.

The array factor equation can be rewritten:

$$AF = A_o e^{j\frac{(N-1)}{2}\varphi} \frac{\sin\left(\frac{N}{2}\varphi\right)}{\sin\left(\frac{\varphi}{2}\right)} \tag{6.2}$$

If the references point is the physical center of the array, the array factor of equation (6.2) reduces to:

$$AF = A_o \frac{\sin\left(\frac{N}{2}\varphi\right)}{\sin\left(\frac{\varphi}{2}\right)} \tag{6.3}$$

AF in equation (6.3) reaches the maximum at $\varphi = 0$, and the maximum value is N. The array factor of equation (6.3) is normalized $(AF)n$ so that the maximum value is equal to unity. The normalized array factor is:

$$(AF)_n = \frac{\sin\left(\frac{N}{2}\varphi\right)}{\mathrm{N}\sin\left(\frac{\varphi}{2}\right)} \tag{6.4}$$

The maximum of the array factor occurs for $\varphi = 0$. The desired scan angle is,

When we place the maximum of an array factor at the desired scan angle θ_s, we have $\varphi = kd\ sin\ \theta_s + \beta = 0$. Thus, phase excitation between the antennas $\beta = -kd\sin(\theta_s)$ so that the main beam maximum is in the direction θ_s relative to the broadside direction. The next maximum array factor value is at $\varphi = \pm 2\pi$. To avoid the second maximum array factor, which is the grating lobe, we have to make the visible region < $-kd\sin(\theta_s)$. Where $k = 2\pi/\lambda$. As a result, the separation distance should be $d < \frac{\lambda}{1+|\sin\theta_s|}$ to avoid the grating lobe.

The spacing between the antenna (d) affects both the mutual coupling and the existence of grating lobes. Both the mutual coupling and grating lobe existence affect the antenna array's beam scanning performance. To reduce the mutual coupling between the antennas, the separation distance (d) should be large. On the other hand, to avoid the grating lobes, the separation between the antennas should not ($d_{max} < \frac{\lambda}{1+|\sin\theta_s|}$) for a large array. A short spacing increases the mutual coupling between the antennas, and a large spacing affects the existence of the grating lobes. Thus, at high frequency, where the wavelength is short, the separation distance (d) is large compared to the wavelength so that the grating lobes will exist in the visible region. The existence of the grating lobe affects the array beam scanning. Instead, at low frequency, where the wavelength is large compared to the separation distance (d), the mutual coupling will affect the array's performance. Thus, fixing the separation distance (d) between the antennas in an array for various operating frequencies is challenging.

We need to choose an optimum value for the separation distance to improves the antenna elements' scan performance in an array. The minimum spacing value would be determined at the lowest frequency value of the frequency range. Instead, the maximum spacing value can be evaluated at the highest frequency value of the frequency range. Thus, we hypothesize that the scope of suitable separation distances value range will be narrow.

The first sub-section will study the broadside phased antenna array, which means the scan angle (θ_s) is **zero.** Then, in the following sub-section, the beam scanning performance will be presented.

6.3.1 Broadside linearly polarized patch antenna phased array

The five-element uniform antenna array will be used to study both the mutual coupling effect and the grating lobe's existence at four operating frequencies—two frequencies at the low-frequency range and another two operating frequencies the high-frequency range. **Figure** 6.1 and **Figure** 6.2 show the five-elements uniform phased array, a unit cell of one antenna element, respectively. In this analysis section, the feed line is fixed (W_{FL}= 59 µm), and the patch geometry and mold height are variable. Also, the separation distance between the antennas is variable to analyze its impact. The antenna was fabricated on a quartz substrate, which has ε_r=3.78.

We use the optimum dimension of linearly polarized patch antenna that has been provided in Chapter 5 for the straighten feed line design at the four interesting operating frequencies (81.5 GHz, 88.5 GHz, 94.5 GHz, and 100.5 GHz). At each operating frequencies, separation distance (d) is variable. We will check the maximum active reflection coefficient (S_{ii}) and mutual coupling S_{ij} at each separation distance (d) value for each operating frequency. The active s-parameter of an antenna within an array is its s-parameter when all the other antennas are excited. So the active S_{ii} is the reflection confession of antenna "i" when all other antennas are excited

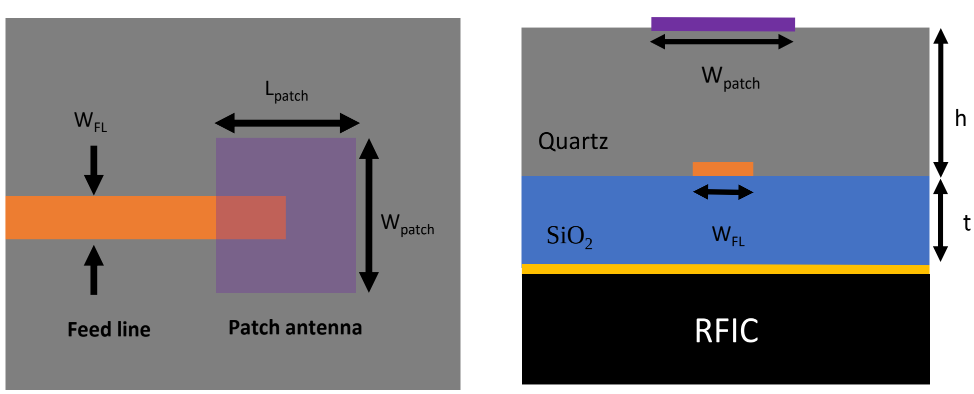

Figure 6.2 One antenna element cell (unit cell).

Results and Discussion:

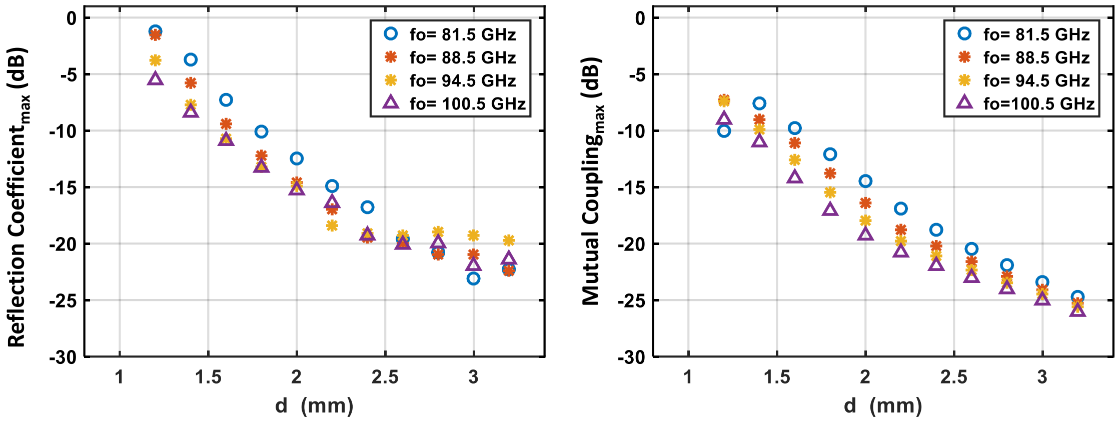

Figure 6.3 Maximum active reflection coefficient and mutual coupling vs. separation distance ($\boldsymbol{d}$) at different f_o for broadside LP phased array.

Figure 6.3 presents the reflection coefficient and mutual coupling vs. separation values at different operating frequencies (f_o) for broadside LP phased array. The plots in **Figure** 6.3 show that both the reflection coefficient and mutual coupling decrease with d. We expected the decrease in mutual coupling and reflection coefficient as d decreases. We also observe from **Figure** 6.3 that the highest maximum mutual coupling among the four chosen operating frequencies is at f_o= 81.5 GHz, wavelength (λ)= 4 mm, the lowest operating frequency in the interested frequency band (81.5-100.5 GHz). As mentioned earlier, a short spacing increases the mutual coupling between the antenna. Thus, at a low frequency where the wavelength is longer, the mutual coupling will affect the array's performance. As a result, the minimum spacing value would be determined at the frequency range's lowest frequency value. If we choose, the maximum acceptable mutual coupling to be (S_{ij}) > -10 dB. Then, we notice from **Figure** 6.3 that the minimum d should be > 1.6 mm= 0.4λ.

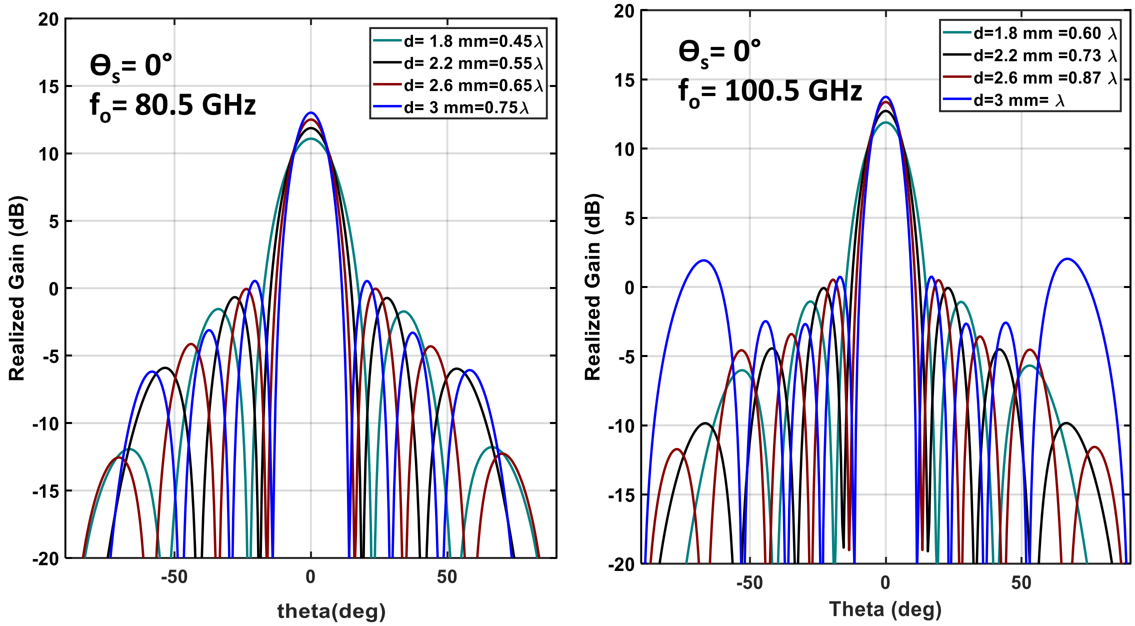

Figure 6.4 Realized gain vs. theta at different $\boldsymbol{d}$ for broadside case LP phased array at different d.

From the realized gain vs. theta plot in **Figure** 6.4, we observe that the grating lobe appears very strongly in the visible region when d= 3mm at operating frequency f_o= 100.5 GHz, wavelength (λ)= 3 mm, the highest operating frequency in the interested frequency range. As mentioned earlier, a large spacing d affects the grating lobes' existence so that the grating lobes will appear at higher frequencies, where the wavelengths are short. Therefore, the maximum spacing value can be evaluated at the highest frequency value of the frequency range. Thus, the maximum spacing value (d) < 3mm. If we look to the theory, the simplest theory equation from the AR, which is $d_{max} < \frac{\lambda}{1+|\sin\theta_s|}$, says that maximum d is also < 3mm=λ at f_o=100.5 GHz and broadside (θ_s=0).

However, the maximum d is also limited by the desired scan angle $\left(d_{max} < \frac{\lambda}{1+|\sin\theta_s|}\right)$. From the d_{max} equation, as the scan angle increase, the d_{max} decrease. To determine the d_{max}, we need to study the scan beam performance and how the d limits the range of scan angle. In the next sub-section, we will analyze the beam scan performance, so we will be able to determine the maximum separation distance d_{max} between the antennas in a phased array.

6.3.2 Beam scanning performance analysis of an H-plane LP 5-element phased array

In this section, the beam scanning of the uniformly spaced one-dimensional phased array is studied. The pattern's main beam is steered to the desired angle by feeding each antenna with identical amplitude (A_o) and a progressive phase shift equal to β between the antennas. Phase excitation between the antennas $\beta = -kd \sin(\theta_s)$ so that the main beam maximum is in the direction θ_s relative to the broadside direction.

Before steering the beam, we have to choose the acceptable values for the separation distance (d) between the antennas. From the broadside analysis results (**Figure** 6.3), a value of d can be selected, so the antennas' mutual coupling (S_{ij}) is reasonable. We choose the acceptable value of S_{ij} to be ≤ -10 dB. As a result, the allowable values for d are from 1.8 mm to 3 mm. See **Figure** 6.3 for more justification.

We analyze the beam scanning for two different operating frequencies -- one at the low-frequency range 81.5 GHz, another at the high-frequency range 100.5 GHz. At each operating frequency, the separation distance (d) is changed over several values (1.8, 2.2, 2.6, and 3 mm) to study the effect of the d on the been steering at the two different operating frequencies (81.5 GHz, and 100.5 GHz). The beam is steered to a specific angle (θ_s) from 0 to -50°by changing the phase shift between antennas β at each d (See **Figure** 6.1).

Among the other characteristics, one critical characteristic of the phased array is sidelobe level, and we defined it as:

$$SLL = 20 \log \left[\frac{|maximum\ value\ of\ the\ largest\ side\ lobe|}{|maximum\ value\ of\ main\ lobe|} \right] \quad (6.5)$$

SLL is one of the evaluation criteria that we are going to use to analyze the phased array. The SLL vs. θ_s at different d values is also analyzed for the two operating frequencies (81.5 GHz and 100.5 GHz) in this study. We choose the acceptable value of SLL to be ≤ -10 dB.

Case 1: f_o= 81.5 GHz:

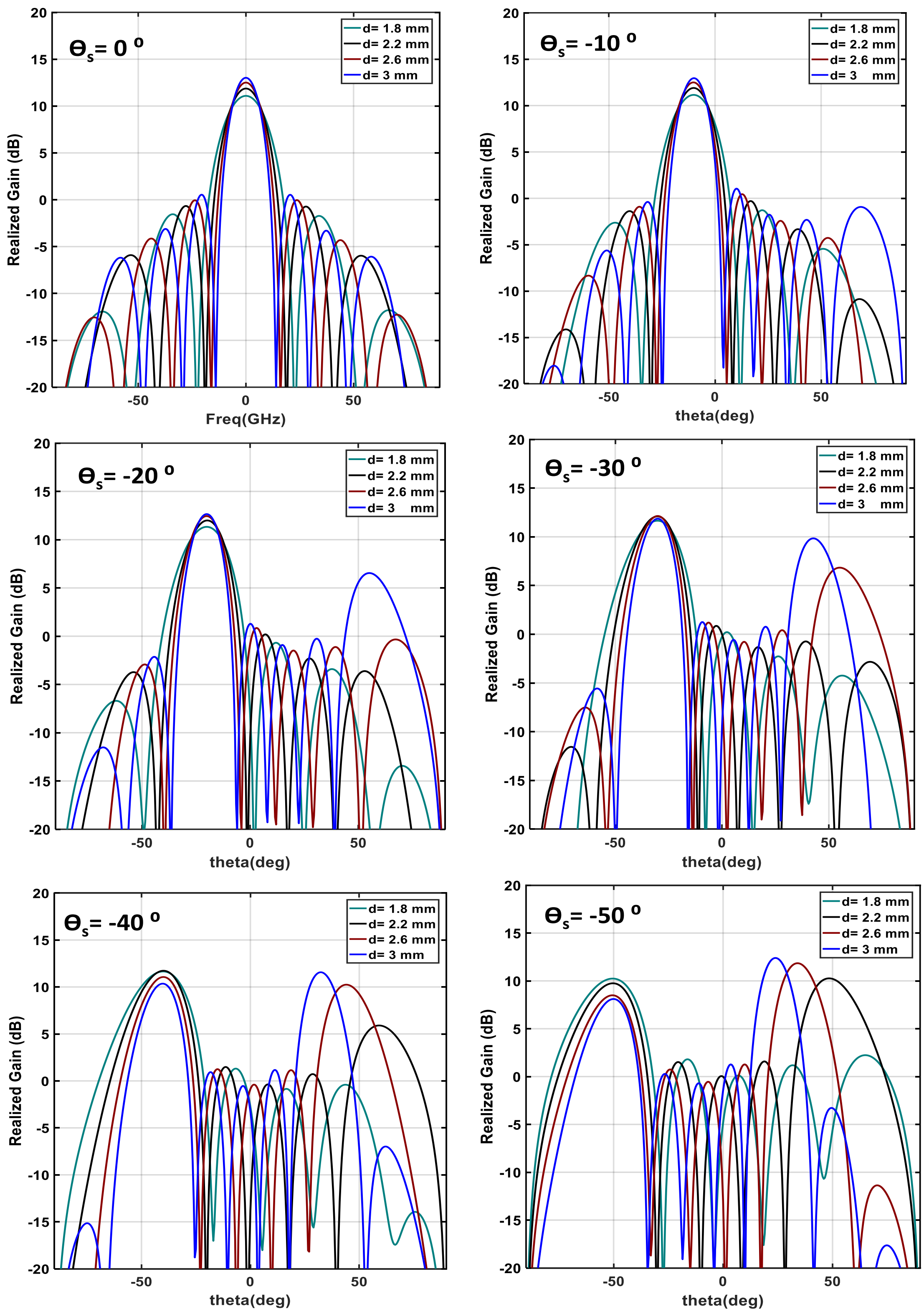

Figure 6.5 Realized gain v. Theta. at different scan angles for f_o=81.5 GHz.

Case 2: f_o= 100.5 GHz:

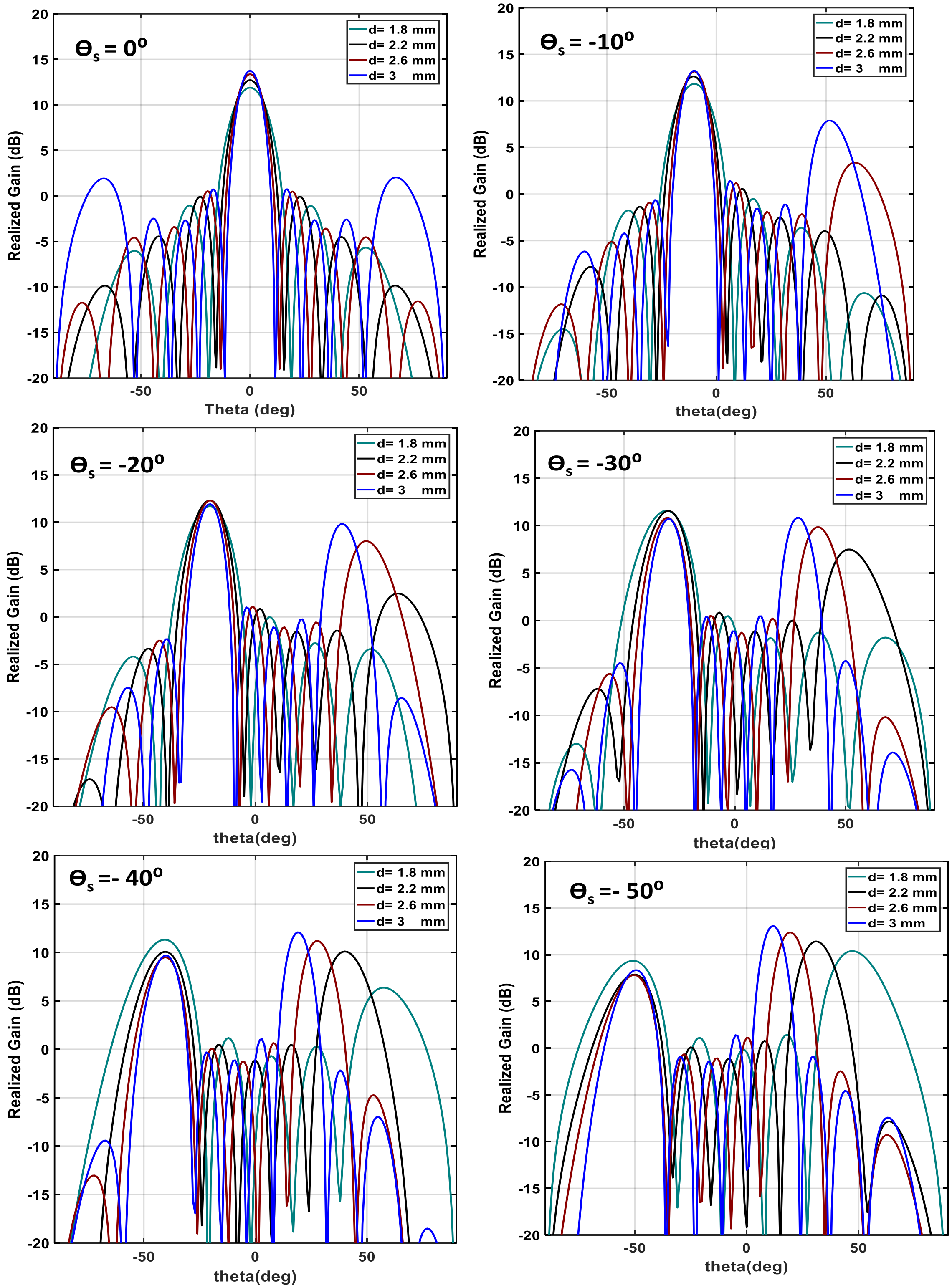

Figure 6.6 Realized gain v. Theta. at different scan angles for f_o=100.5 GHz.

Results and Discussion:

The beam steering's results, the realized gain vs. theta at different scan angles (θ_s= 0-50°) for the two operating frequencies (f_o= 81.5 and 100.5 GHz), are presented **Figure** 6.5, **Figure** 6.6. If we break these results down further by plotting the realized gain and SLL vs. scanning angle (θ_s) at f_o= 81.5 GHz and f_o=100.5 GHz, we get the new results in **Figure** 6.7 and **Figure** 6.8.

The results in **Figure** 6.5 and **Figure** 6.6 represent the realized gain vs. theta for different d and θ_s values at the two f_o= 81.5 GHz and 100.5 GHz. These results show that as the d and θ_s increase, the grating lobe movies into the visible region. Moreover, at a higher operating frequency (f_o=100.5 GHz) and maximum d=3mm, the grating lobe exists in the visible region at θ_s=0. On the other hand, when the f_o=81.5 GHz and maximum d =3mm, the grating lobe exists in the visible region at θ_s=-10. As I mentioned in the introduction of this chapter, to avoid the existence of grating lobes, the d_{max} between the antennas should be $< \frac{\lambda}{1+|\sin\theta_s|}$. Thus, the grating lobe's appearance in the visible region is affected by both the f_o and desired scan angle (θ_s).

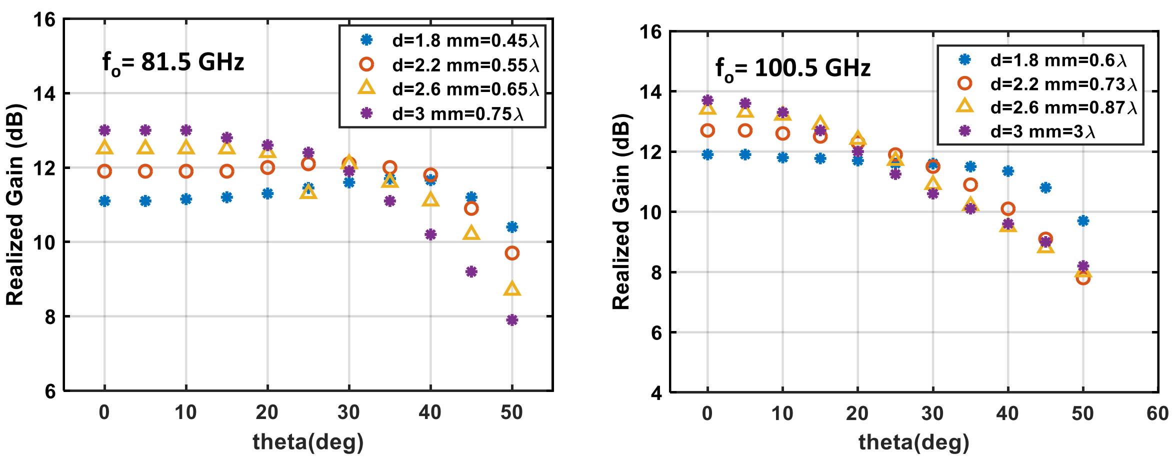

a. Realized gain vs scan angle.

b. Realized gain vs. scan angle

Figure 6.7 Realized gain vs. θ_s at different $\boldsymbol{d}$ for f_o= 81.5 and 100.5 GHz.

The Realized gain vs. θ_s results in **Figure** 6.7 shows that the realized gain starts to decrease at θ_s= 30° at both operating frequencies (81.5 GHz and 100.5 GHz). This reduction in the realized gain because of the scan loss. The complete pattern of the phased array is found by multiplying the array factor by the element pattern. As the main beam is scanning, the element pattern remains fixed while the array factor examines the phase change. The total array pattern's peak follows the element pattern shape as the phased array is scanned. Thus, the array's main beam's peak is reduced by the level of the element pattern at the desired angle. As a result, the realized gain decreases as the array is scanned.

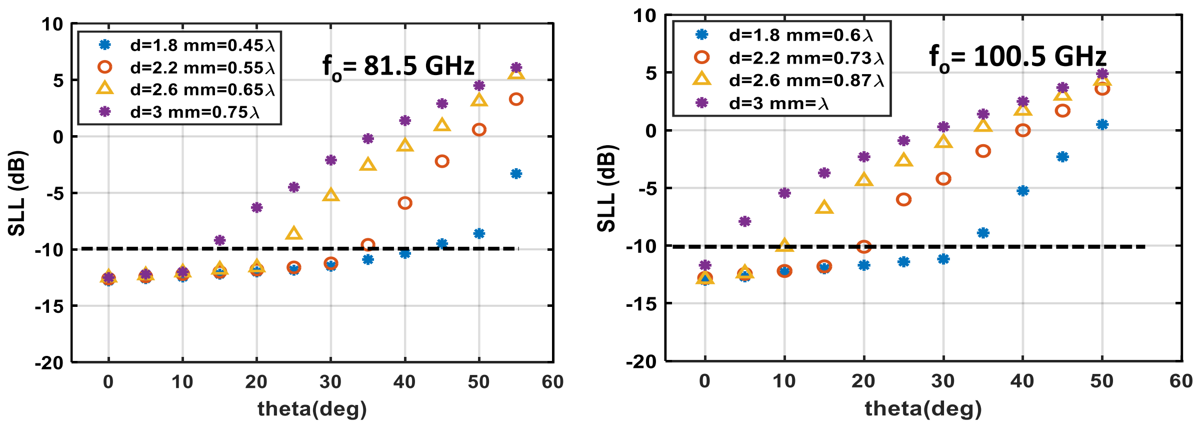

a. SLL vs. scanning angle (theta θ_s) for f_o= 81.5 GHz. b. SLL vs. scanning angle (theta θ_s) for f_o= 100.5 GHz.

Figure 6.8 SLL vs. θ_s at different $\boldsymbol{d}$ for f_o= 81.5 and 100.5 GHz.

The results in **Figure** 6.8 show that as d and θ_s increase, the sidelobe level (SLL) increases. SLL can increase for two reasons: one, the near sidelobes gain increases as they move closer to the element pattern main beam. The second reason is the grating lobe moving into the visible region when the visible region becomes too large. The visible region increases either by increases d or increases the scan angle θ_s.

From the given results in this section, we can find the maximum scanning angle ($\theta\ _{s_{max}}$) where the SLL and realized gain have acceptable values at each d (1.8 mm to 3 mm) and operating frequencies (81.5 GHz and 100.5 GHz). We choose the acceptable value for SLL to be ≤ -10 dB. The $\theta_{s_{max}}$ vs. d plot is shown in **Figure** 6.9. The $\theta_{s_{max}}$ decreases as d and operating frequencies (f_o) increase. At the lowest separation distance $d = 1.6\ mm$, the $\theta_{s_{max}} = 40^{\circ}$ and 30° at f_o=81.5 GHz and 100.5 GHz, respectively. On the other hand, at the highest separation distance $d = 3\ mm$, the $\theta_{s_{max}} = 10^{\circ}$ and 0° at f_o=81.5 GHz and 100.5 GHz, respectively. We noticed that the beam could not be steered at the highest operating frequency (f_o=100.5 GHz) in the interested frequency range when the separation distance d=3mm because of the grating lobe in the visible region at broadside (θ_s=0). We can conclude that the d_{max} should be < 3mm to avoid the grating lobe and steer the phased array's main beam away from the broadside.

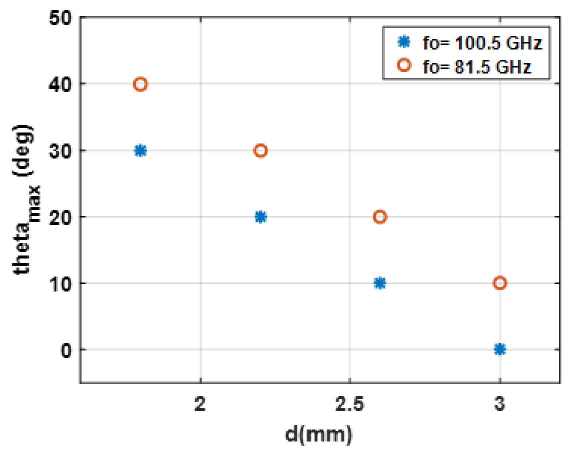

Figure 6.9 Maximum θ_s vs. separation distance $\boldsymbol{d}$ at f_o= 81.5 and 100.5 GHz.

6.4 Impact of the fixed feed spacing on the performance of the CP phased array

This section analyzes the impact of the separation distance between antennas (d) on a CP phased array's beam scanning performance at different operating frequencies (81.5 GHz to 104.5 GHz) when the antennas are coupled to fixed feed lines. We study the H-plane five-elements uniform amplitude and spacing array. The antennas are equally separated (d) and fed to an identical amplitude with a progressive phase shift equal to β between the antennas.

We attempted to use the optimum circularly polarized antenna dimension provided in chapter 5. When we put them in the 5-element array, we find that the CP antenna was very sensitive to the presence of the adjacent element in the array. We realize the optimization needs to be conducted with other elements present and changes with the separation value d. As a result, we choose the proper separation values (d) based on linear polarization phased array analysis in section 6.3 to use them in CP phased array study.

6.4.1 Optimization analysis for CPA at specific separation distance d

To study the CP Phased array, we need to first redesign the antenna for a specific fixed spacing value d. Based on the LP broadside phased array results, the reasonable spacing is d= 2.2 mm. **Figure** 6.8 and **Figure** 6.9 show d= 2.2 mm is a reasonable choice of spacing value for low mutual coupling, lower reflection coefficient, and acceptable scan angle range. Also, we want to study the beam steering performance at a larger separation distance between the antennas d. This analysis will help to answer the research questions of this chapter. How will the large d affect the grating lobe's existence? And how will that impact the scan angle range?

We use an infinite array simulation to accelerate the analysis. We also use unit cell simulation at the specific spacing value, either $d = 2.2$ mm or d=2.8 mm, to run the optimization analysis to find the circular polarized phased array's optimized antenna dimensions. The variable is the patch dimensions (W_{cor}, h_p, and L_p). The patch antennas are shifted to a positive direction of the y-axis to improve the matching between antennas and feed lines. **Figure** 6.10 illustrates the variable values. The antennas' separation distance is fixed to the specific value, which either 2.2 mm or 2.8 mm. Then, we use the optimum antenna dimensions from the infinite optimization analysis results to study the circularly polarized 5-elements phased array performance at each separation distance (2.2 mm and 2.8 mm).

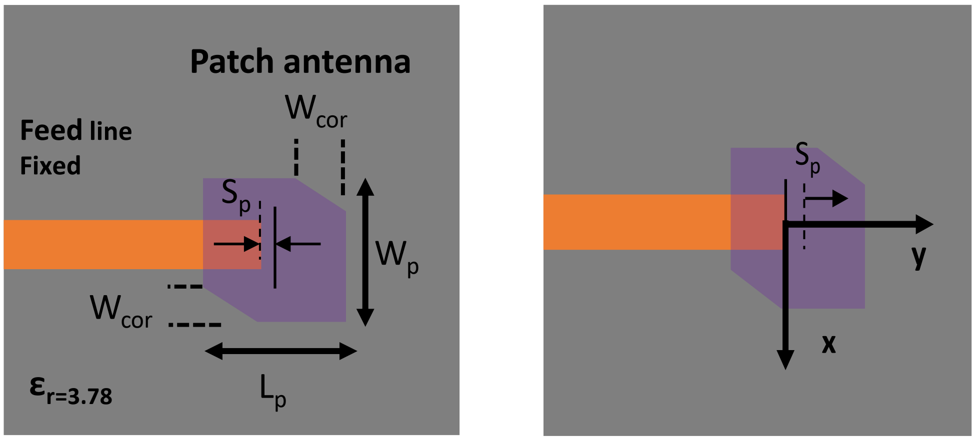

Figure 6.10 Unit cell element of circularly polarized phased array.

6.4.1. A The separation distance between the antennas is 2.2 mm

In Chapter 5, we observed that the optimized antenna's height (h_{opt}) is almost equal to the height of the feed line' substrate (h_{FL}), which is equal to 40 µm. Thus, the height of the antenna will be fixed to 40 µm to run the simulation faster. Also, fixing the height of the patch antenna simplifies the optimization analysis.

The analysis procedure used to achieve the antennas' optimal dimensions is similar to the circularly polarized patch antenna's optimization analysis procedure in Chapter 5. At the optimal dimensions (W_{opt} =L, W_{cor}, and S_{p_opt}) of the antenna, the reflection coefficient is low ($S_{11} < -20$ dB), and the axial ratio is close to one (AR < 2 dB) at the several operating frequencies f_0 in W band. The cost function is equal to zero when the two conditions are satisfied.

Results and Discussion:

The results of the optimization are shown in **Figure** 6.11. The optimal antenna's dimensions vs. operating frequency plots show that $f_o \propto {}^{1}/_{L_{opt}}$. This is expected from the cavity and TL models analysis, as mentioned in the introduction section in Chapter 3. Moreover, the antenna's dimensions vs. operating frequency plot in **Figure** 6.11 is a little discernable pattern to the optimal width corner (W_{cor}) and the S_{p_opt} as the design frequency changes. The S_{p_pt} vs. f_o plot in **Figure** 6.11 indicates that the patch optimal shift value is almost constant over the whole interested frequency band and equal to 74 µm. Also, the W_{corner} value is nearly equal to 130 µm. Looking at the CP's optimization results in **Figure** 5.13 from Chapter 5, we can see these results are different from the optimization result in this chapter.

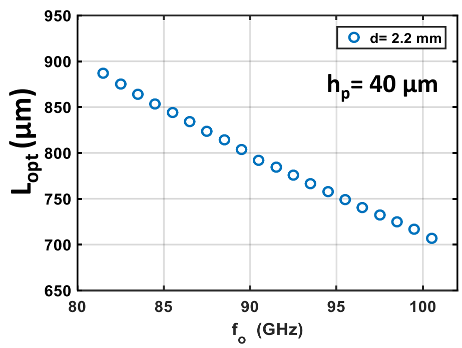

a. L_{opt} vs. f_o at d= 2.2 mm.

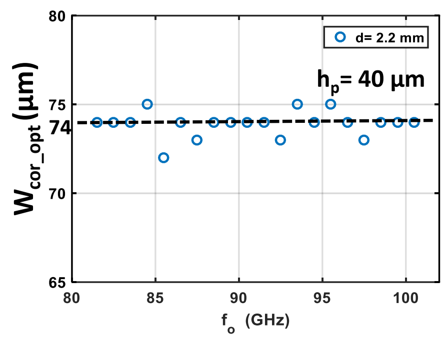

b. W_{cor_opt} vs. f_o at d= 2.2 mm.

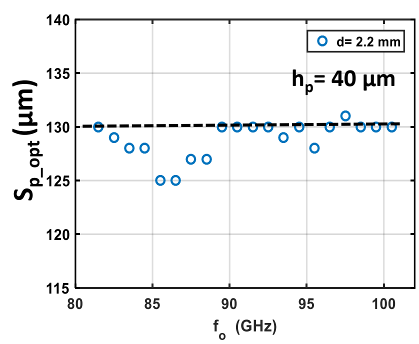

c. S_{p_opt} vs. f_o at d= 2.2 mm.

Figure 6.11 Optimal antenna's dimensions analysis for the infinite array at $\boldsymbol{d}$= 2.2 mm.

We can also observe from the optimal antenna's dimensions analysis in **Figure** 6.11 that the important CP antenna characteristics, the impedance matching (S_{11}) and AR, depending on the patch's length. The other antenna's dimensions (W_{cor_opt} and S_{p_opt}) are almost constant all over the f_o band, so these two dimensions are set to a constant value. Thus, The antenna's length is the only variable; therefore, the optimization analysis is simpler and consumes less time for running. The simulation analysis for infinite CP patch antenna phased array at different f_o is rerun with the following conditions:

- W_{cor}= 74 µm.
- S_p= 130 µm.
- h_{patch}= 40 µm
- L_p=L_{p_opt}, The length of the antenna is equal to the optimized length from the previous optimization analysis.
- At each f_o return loss (S_{11}) ≤ -20 dB and AR < 2 dB.

The result is shown in **Figure** 6.12. This result is identical to the previous work in **Figure** 6.11c (L_{opt} vs. f_o), despite those dimensions being fixed and the length is the only parameter that changing.

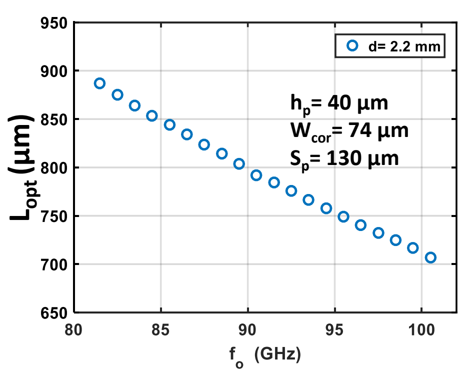

Figure 6.12 L_{patch_opt} vs. f_o at $\boldsymbol{d}$= 2.2 mm.

6.4.1. B The separation distance between the antennas is 2.8 mm.

Also, we want to study the beam steering performance at a larger separation distance between the antennas d= 2.8 mm. The variable patch dimensions are W_{corner}, height (h), and L_{patch}. Also, the patch will be shifted to the positive of the y-axis. The separation distance between the antennas is fixed and equal to 2.8 mm. The height of the antenna will be fixed to 40 µm as the previous analysis of d=2.2 mm.

Results and Discussion:

The results are shown in **Figure** 6.13. We observe that $f_o \propto {}^{1}/_{L_{opt}}$, which is expected from the cavity and TL models analysis, as mentioned in the introduction section in Chapter 3. Moreover, the antenna's dimensions vs. operating frequency plot indicate a little discernable pattern to the optimal width corner (W_{cor}) and the S_{p_opt} as the design frequency changes. The S_{p_opt} vs. f_o plot shows that the patch location's optimal shift value is almost constant over the whole interested frequency band, equal to 65 µm. Also, the W_{cor_opt} value is nearly identical to 172 µm.

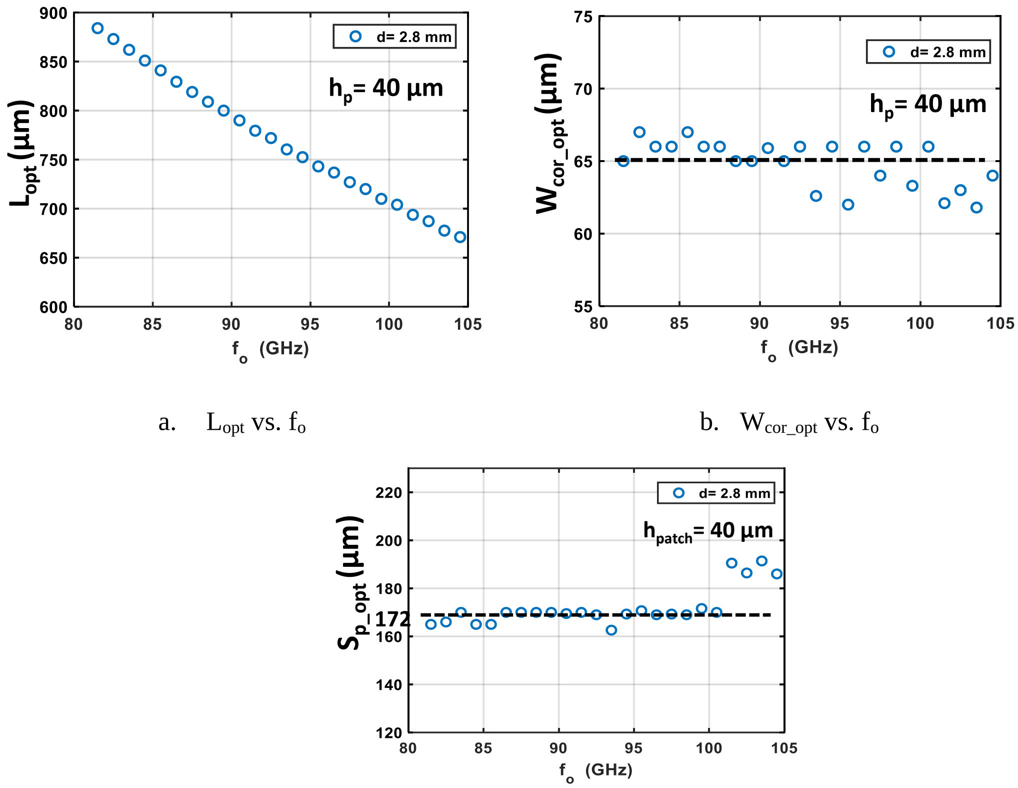

a. L_{opt} vs. f_o

b. W_{cor_opt} vs. f_o

c. S_{p_opt} vs. f_o

Figure 6.13 Optimal CP antenna's dimensions vs. operating frequency at ***d***= 2.8 mm and h_p= 40 μm for infinite CP phased array.

We can observe from the optimal antenna's dimensions analysis that the CP antenna performances, which are the impedance matching (S_{11}) and AR, depending on the patch's length. The other antenna's dimensions (W_{corner_opt} and $Shift_{patch\_opt}$) are almost constant all over the f_o band, so these two dimensions are set to a constant value. Thus, The antenna's length is the only variable; therefore, the optimization analysis will be simpler and consumes less time for running. The simulation analysis for infinite CP patch antenna phased array at different f_o is rerun with the following conditions:

- W_{cor}= 65 μm.
- S_p= 172 μm.

- h_p= 40 µm
- L_p=L_{opt}, The length of the antenna is equal to the optimized length from the previous optimization analysis.
- At each f_o return loss (S_{11}) ≤ -20 dB and AR < 2dB.

The result in **Figure** 6.14 is identical to the previous work in **Figure** 6.13a (L_{patch_opt} vs. f_o), regardless of those dimensions being fixed and the length is the only parameter that changing.

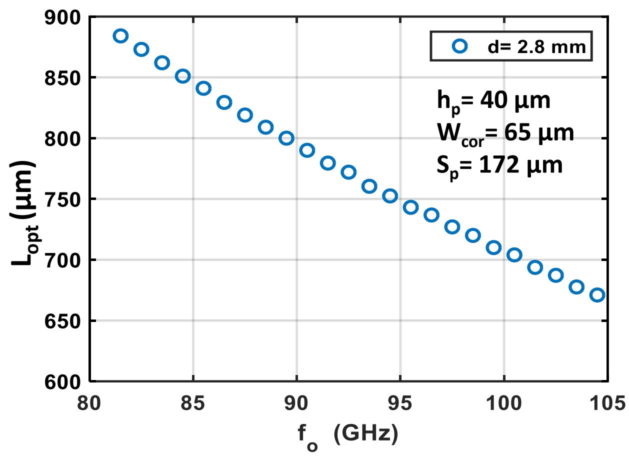

Figure 6.14 Optimal CP antenna's length vs. operating frequency at ***d***= 2.8 mm, W_{corner}= 65 µm, $shift_{patch}$= 172 µm, and h_{patch}= 40 µm for phased array.

6.4.2 Beam scanning performance analysis of an H-plane CP 5-element phased array

The uniformly 5-element circularly polarized H-plane phased array's beam scanning capacity is studied in this section. The pattern's main beam is steered to the desired angle θ_s. All the antennas are fed to an identical amplitude (A_o) with a progressive phase shift equal to β between the antennas.

We study the CP phased array's beam steering performance for two different spacing values (2.2 mm and 2.8 mm) at two operating frequencies -- one at the low-frequency range is 81.5 GHz, another at the high-frequency range of 100.5 GHz. We use the optimal CP antenna dimensions from section 6.4.1 at separation distance d= 2.2 mm and 2.8 mm. We make some modifications to the W_{cor} and S_p values to achieve AR < 2 dB. Table 6.1 shows the optimal dimensions of the antennas at each separation distance and operating frequency. The beam is steered to a specific angle (θ_s) from 0 to -50° by changing the phase shift between antennas β at each d. SLL and AR values are used to analyze the phased array's scan performance. We choose the acceptable value of SLL to be ≤ -10 dB and AR to be < 2 dB.

Table 6.1 The optimal CP antenna dimensions at different f_o and $\boldsymbol{d}$.

f_o (GHz)	d (mm)	$L_{patch}=W_{patch}$ (µm)	h_{patch} (µm)	S_p (µm)	W_{cor} (µm)
81.5	2.2	887	40	129	73
100.5	2.2	709	40	130	74
81.5	2.8	886	40	172	75
100.5	2.8	704	40	172	75

Result and discussion:

The beam steering's results, the realized gain vs. theta at different scan angles (θ_s= 0-50°) for the two operating frequencies (f_o= 81.5 and 100.5 GHz), are presented **Figure** 6.15 and **Figure** 6.16. If we break these results down further by plotting the realized gain and SLL vs. scanning angle (θ_s) at different f_o (81.5 GHz and 100.5 GHz) and spacing d (2.2 mm and 2.8 mm), we get the new results in **Figure** 6.17 and **Figure** 6.18. Furthermore, we find the maximum scan angle, where the SLL≤ -10 dB and AR< 2 dB, at each f_o for the two d values.

The results in **Figure** 6.15 and **Figure** 6.16 represent the realized gain vs. theta for different d (2.2 mm and 2.8 mm), and θ_s (0° to -50°) values at the two f_o, 81.5 GHz and 100.5 GHz. These results show that as the d, f_o, and θ_s increase, the grating lobe movies into the visible region. As I mentioned in section 6.3, to avoid the grating lobe, we have to make the visible region < $-kd\sin(\theta_s) = -\frac{2\pi d}{\lambda}\sin(\theta_s)$. The visible region increases as f_o, d, and θ_s increase.

At the larger separation distance d=2.8 mm and high operating frequency f_o= 100.5 GHz, the grating lobe exists in the visible region at broadside θ_s=0 (see **Figure** 6.16). However, at the same larger separating distance (d=2.8 mm) and low operating frequency f_o= 81.5 GHz, the grating lobe exists in the visible region at θ_s=-10°. On the other hand, at the shorter separation distance d=2.2 mm and high operating frequency f_o= 100.5 GHz, the grating lobe exists in the visible region at broadside θ_s=- 20° (see **Figure** 6.15). At low operating frequency f_o= 81.5 GHz, the grating lobe exists in the visible area at θ_s=-30°. Thus, the grating lobe's existence in the visible region limits the scan angle range (θ_s). As we observed from the LP phased array's steering performance in section 6.3, the grating lobe occurs in the visible region as the visible region increases by increasing f_o, and d and this limits the scan angle θ_s.

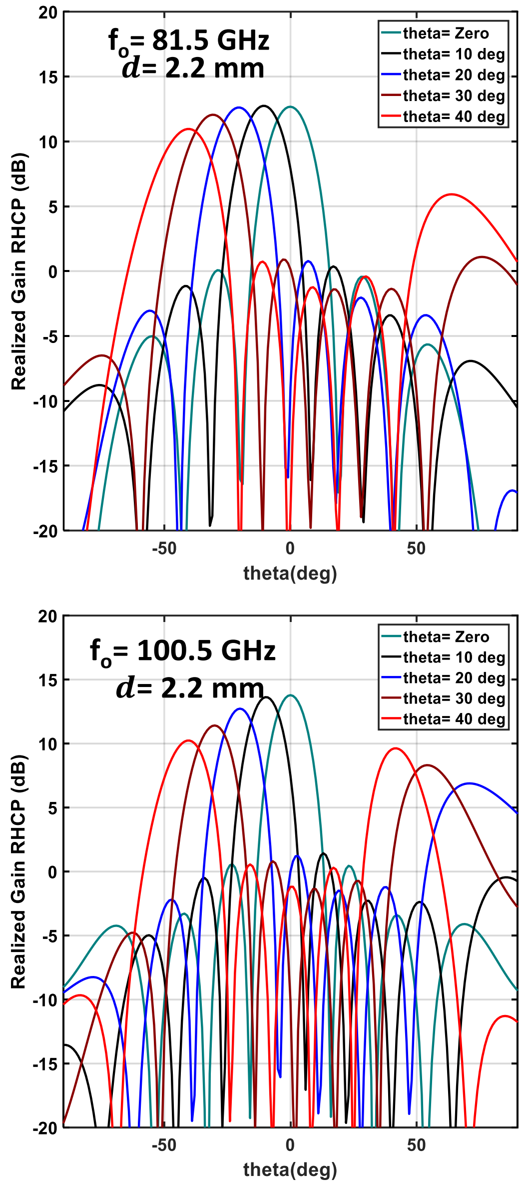

Figure 6.15 Realized gain RHCP vs. theta for ***d***= 2.2 mm at f_o= 81.5 and 100.5 GHz.

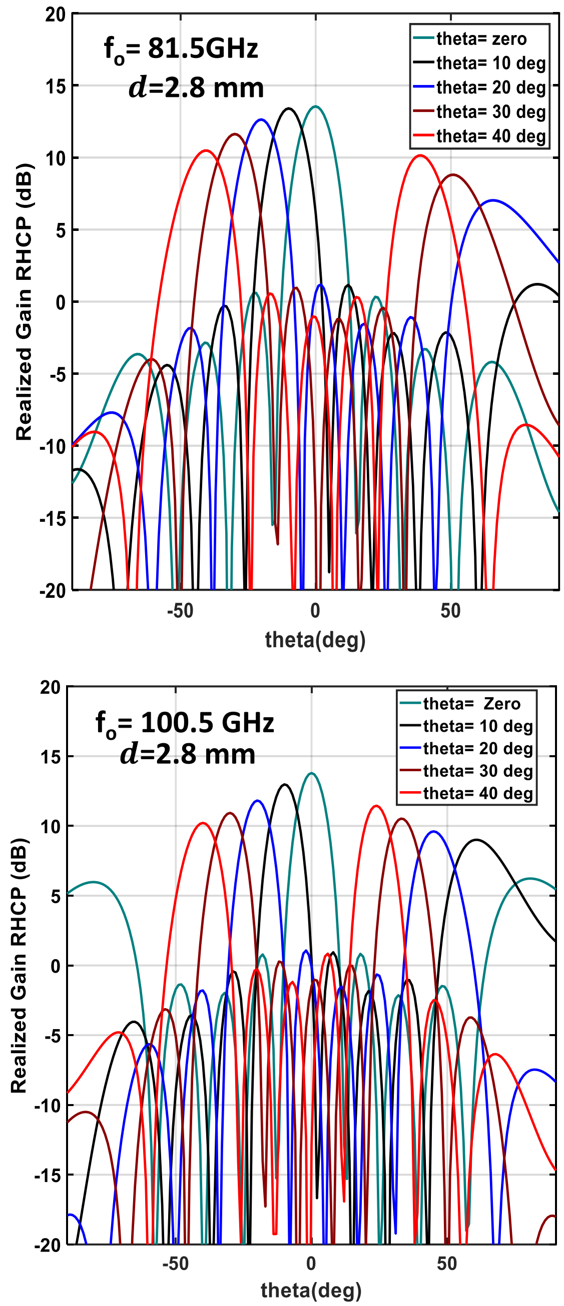

Figure 6.16 Realized gain RHCP vs. theta for $\boldsymbol{d}$= 2.8 mm at f_o= 81.5 and 100.5 GHz.

Figure 6.17 and **Figure** 6.18 present SLL and AR vs. scan angle results at different f_o and d. We observe that the beam steering range is narrow at the large separation distance between the antennas. At d= 2.8 mm and f_o=100.5 GHz, the θ_{s_max}= 0 °. On the other hand, at d=2.2 and f_o= 100.GHz, the θ_{s_max}= ±10 °. This reduction in the maximum san angle is caused either by increasing in SLL (SLL> -10 dB) or increasing in AR (AR > 2 dB). The increase in SLL occurs when the grating lobe moves to the visible region. We expected this observation because as the d increases, the visible region increases as well. Thus, the grating lobe occurs in the visible region and increases the SLL, especially at high frequencies. We can see in **Figure** 6.16 that the grating lobe exists in the visible region at θ_c=0° at d= 2.8 mm and f_0= 100.5 GHz. Thus, the beam steering range is narrow.

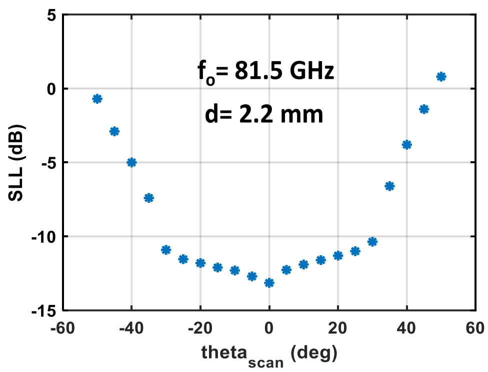

a. SLL vs. scan angle at f_o= 81.5 GHz

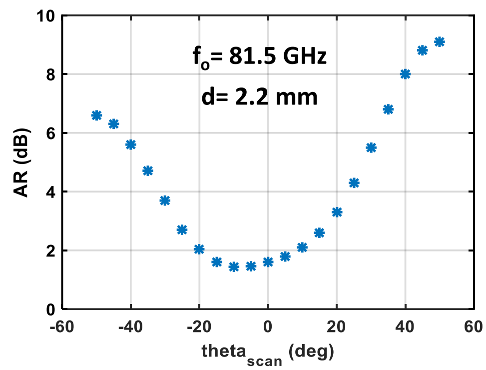

b. AR vs. scan angle at f_o= 81.5 GHz.

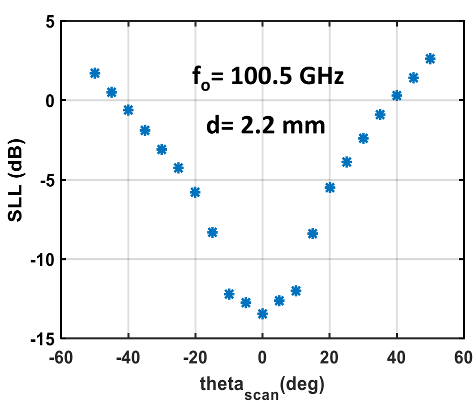

c. SLL vs. scan angle at f_o= 100.5 GHz.

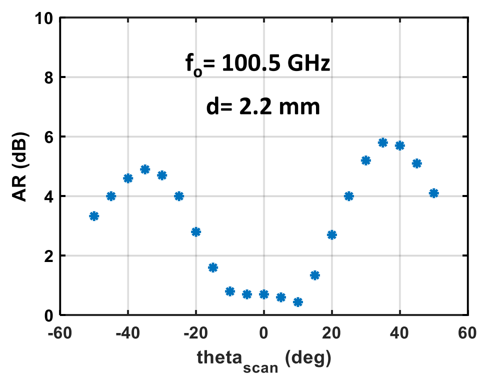

d. AR vs. scan angle at f_o= 100.5 GHz.

Figure 6.17 Beam steering results for $\boldsymbol{d}$= 2.2 mm.

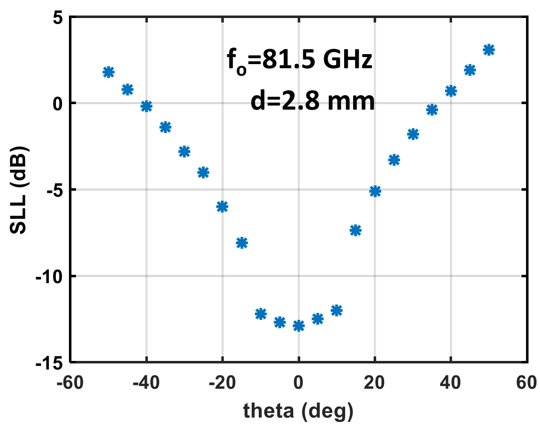

a. SLL vs. scan angle at f_o= 81.5 GHz.

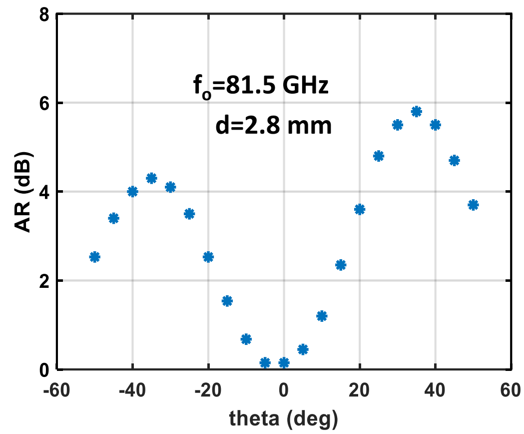

b. AR vs. scan angle at f_o= 81.5 GHz.

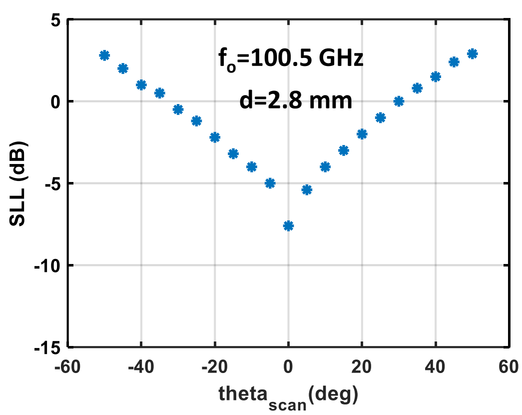

c. SLL vs. scan angle at f_o=100.5 GHz.

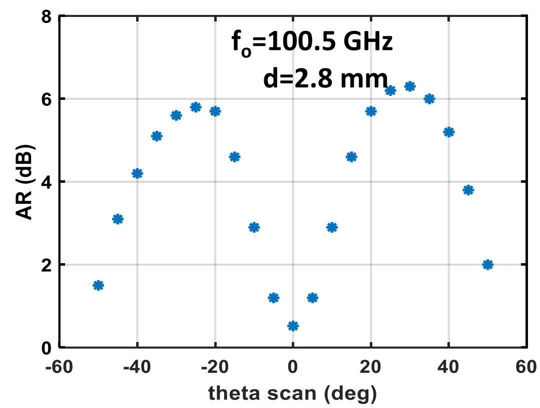

d. AR vs. scan angle at f_o= 100.5GHz.

Figure 6.18 Beam steering results for ***d***= 2.8 mm.

The scan angle range, when the separation distance is 2.2 mm, is between -15° and 5°, and between -10° and 10°, at operating frequencies f_o= 81.5 GHz and f_o= 100.5 GHz, respectively. However, when the separation distance is 2.8 mm, the scan angle range is between -10° and -10°, and is 0° at operating frequencies f_o= 81.5 GHz and f_o=100.5 GHz, respectively. Table 6.2 shows the scan angle range at each d and f_o.

Table 6.2 The comparison between $\boldsymbol{d}$= 2.2 mm and $\boldsymbol{d}$= 2.8 mm

d (mm)	**Scan angle θ_s Range**
2.2	At f_o=81.5 GHz: $-15 < \theta_{s\_} < 5\ ^o$ At f_o=100.5 GHz: $-10<\theta_s< 10\ ^o$
2.8	At f_o=81.5 GHz: $\theta_{s\_max}= \pm 10\ ^o$ At f_o=100.5 GHz: $\theta_{s\_max}= 0\ ^o$

Furthermore, we observed from the AR vs. scan angle plots for both separation distance values (d= 2.2 and 2.8 mm) results in **Figure** 6.17 and **Figure** 6.18 that AR increases as the scan angle increases. At d= 2.2 mm, the AR > 2dB at $-10 \geq \theta_s \geq 10\ ^o$and $-20 \geq \theta_s \geq 20\ ^o$, for f_o= 81.5 GHz and f_o= 100.5 GHz, respectively. Thus, the beam scan angle range is narrow. Also, we observed from these plots that the AR starts to decrease as the scan angle θ_s increases further. AR is not affected by the array factor. Instead, the embedded element antenna polarization determines the array polarization. However, the embedded element is affected by the separation value d. We plot the theta range where AR < 2 dB for an embedded antenna at the broadside case. **Figure** 6.19 shows AR vs. theta for the embedded element at broadside case for d=2.2 mm and d=2.8 mm at the f_o= 81GHz and f_o= 100.5 GHz. We conclude that the theta range where the AR< 2 dB for the embedded antenna element is narrow. Therefore, AR increases as the scan angle increases, and this also narrows the scan angle range.

Moreover, we noticed in these particular cases (d= 2.2 mm and 2.8 mm) that the AR beamwidth is wider at smaller d. We do not know if this observation can true in general. The AR beam width and d have complicated correlations. This opens a new research question for future work: how does the d affect the AB beamwidth, or is there a correlation between the AR beamwidth and d?

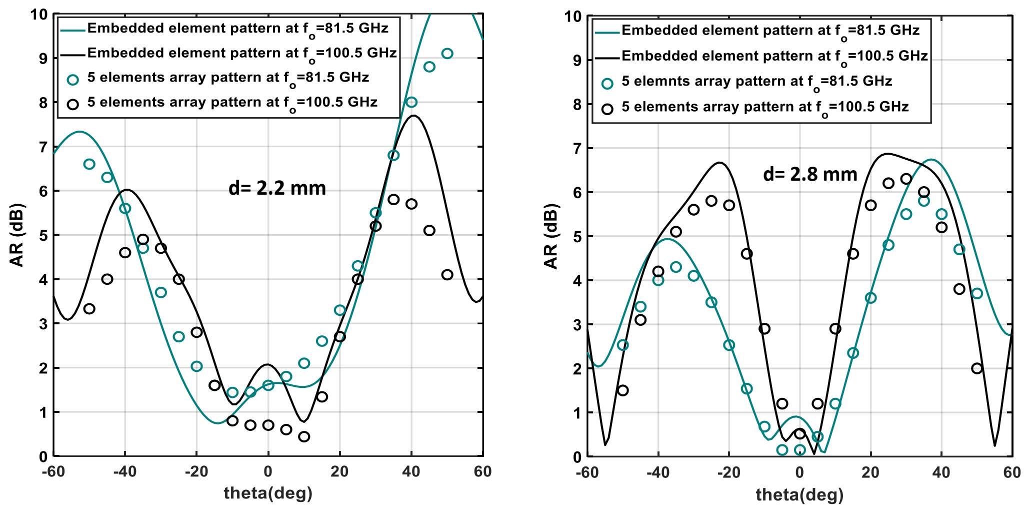

Figure 6.19 AR vs. theta at broadside for embedded antenna and AR vs. θ_s for 5-element antenna array at $\boldsymbol{d}$= 2.2 and 2.8 mm.

We conclude from all the scan angle analysis results that the maximum scan angle (θ_{s_max}) at the shorter spacing d= 2.2 mm is ±10°, and at the larger spacing, d= 2.8 mm, is 0° at high operating frequency (100.5 GHz). Thus, the maximum spacing should be < 2.8 mm to steer the LP or CP phased array's beam away from the broadside. Moreover, we noticed that the scan angle range is narrow at d= 2.2 mm. If we reduce the spacing to 1.8 mm, we may have a more comprehensive scan angle range.

We observed from LP phased array scan performance that the scan angle range is wider at d= 1.8 mm and equals ±30°. But this range would be narrower for CP phased array because the AR bandwidth (where AR<2dB) is narrow and is included in the performance. For example, we noticed that the scan angle range is ±10° at d= 2.2 for CP phased array. In contrast, the scan angle range for LP phased array is ±20°. In conclusion, the CP phased array beam scanning range is narrower than LP phased array bean scanning range.

Additionally, we conclude that generated CP radiation in an array, or single element is not easy compared to LP. Creating CP radiation has many complications because to achieve it, we need to check AR, AR beamwidth, and critical frequency (f_c). Besides, we need to check the impedance matching between the antenna and feed line.

6.5 Research outcome

Based on the primary research questions identified at the beginning of the chapter, the outcomes are listed below:

Question 6.1: How does fixed array lattice impact the circuit parameter of the antenna, such as the mutual coupling and impedance matching, at different f_o for broadside case?

We investigated how the fixed feed spacing impacts the mutual coupling at different operating frequencies and how it affects the beam steering. As we expected**,** a short spacing increases the mutual coupling between the antennas, especially at lower operating frequencies. Thus, The LP 5-element phased array analyses help choose the d_{min}, determined at lower f_o analysis. We found that d_{min} > 1.6 mm.

Question 6.2: How does fixed array lattice affect the antenna's radiation parameter, such as sidelobe level and the grating lobe's existence in the radiation pattern, at different f_o for broadside case?

We explored how the fixed feed spacing affects the grating lobes' existence at different operating frequencies and limits the beam steering. The presence of the grait lobe in the visible region increases the SLL. A large spacing affects the grating lobes' existence, especially at high operating frequencies. Therefore, d_{max} is be defined at the highest f_o in the interested frequency band. In our study cases for LP and CP phased array, we found that d_{max} <2.8 mm. The range of the d is narrower for CP phased array because the AR bandwidth (where AR<2dB) is included in the performance and is narrow.

Question 6.3: **How is the scanning angle limited by the fixed feed spacing at different operating frequencies?**

Choosing the optimum d that will be fixed for a wide range of operating frequencies is challenging. A short spacing increase the mutual coupling between the antennas, and a large spacing affects the existence of the grating lobes. Thus, at high frequency, the grating lobes existed, and at low frequency, the mutual coupling affected the array's performance. As a result, the minimum spacing value was determined at the frequency range's lowest frequency value. The maximum spacing value was evaluated at the highest frequency value of the frequency range. To avoid the grating lobes, the separation between the antennas should not ($d_{max} < \frac{\lambda}{1+|\sin\theta_s|}$) for a large array.

We noticed the scan angle range is ±10° at d= 2.2 for CP phased array. In contrast, the scan angle range for LP phased array is ±20°. In conclusion, the CP phased array beam scanning range is narrower than LP phased array bean scanning range. Additionally, we observed that the presence of the visible region's grating lobes is the main issue that narrows the beam steering range.

As the scan angle increases, the d_{max} decreases ($d_{max} < \frac{\lambda}{1+|\sin\theta_s|}$). We can observe from the LP and CP H-plane phased array analyses that the beam steering range is narrow with fixed feed line spacing over a wide frequency range.

6.6 Summary

The antenna elements' scan performance in an array was studied at different operating frequencies and polarization (LP and CP) in this dissertation. Our study is separate from the standard narrowband antenna array because the feed lines structure is fixed and fabricated on the universal chip's top. However, the antenna elements are changed based on the operating frequencies and polarization requirements. Thus, this study investigated the tradeoffs between the mutual coupling between this type of PCPA and the existence of the grating lobes and how these two factors impact the ability to scan a family of narrowband antennas with fixed separation (d) but different operating frequencies and polarization. This study provides the following contributions for phased patch antenna array coupled to fixed feed lines:

- Understand the impact of the separation distance between the narrowband antennas on the mutual coupling in a phased array for the proposed design. We know how the grating lobes would behave in the narrowband patch antenna, but we are not quite sure about the mutual coupling behavior. Therefore, we evaluated the tradeoff between the presence of grating lobes and mutual coupling in our analysis for the proposed design. This analysis helps to choose the optimum separating distance that works for a wide range of operating frequencies and different polarization.
- Giving knowledge that will help understand the limitation of choosing a fixed d value for a wide range of operating frequencies (f_o) and different polarization (LP and CP). The PCPA is a narrowband antenna, and the spacing for the narrowband antenna is usually chosen to be suitable for that partially narrow bandwidth. Thus, it would be challenging to fix the spacing between the narrowband antennas at different f_o and polarization (LP and CP).

- Giving knowledge that will allow the feed line structure to be optimized from the very beginning and precise analysis of why various factors impact antenna's operating frequencies. Thus, the best feed line design, which includes the separation distance between the feed lines, and material, is chosen and fixed for the universal RFIC chip.

CHAPTER 7: Conclusions and Future Work

7.1 Summary and Contributions

Emerging wireless communication technologies, radar sensors, and fifth-generation wireless telecommunication standard (5G) are being enabled by the mm-wave spectrum, which has a wide bandwidth leading to a higher data rate. Moreover, mm-wave frequencies have a small wavelength; thus, the integrated circuits (ICs) and the antennas integrate within a single package, as the antenna form-factor reduces.

Proximity coupled patch antennas are studied in this dissertation to integrate the antenna and chip within a single package. The antenna is fabricated in the mold material as a separate component mounted on the top of a fixed thin feed line fabricated on a standard packaging chip with a highly integrated mm-wave circuit. Thus, the interconnect loss will be reduced, and the requirement for developing the mm-wave interconnects will be avoided. Also, AiP gives the flexibility to fabricate the antenna on a low permittivity and low loss substrate [1],[14]-[16]. Additionally, AiP provides flexibility in various antenna requirements (bandwidth, directivity, polarization) without making any changes in the designed chip (RFIC). The antenna-lid approach is essential for mm-wave applications where requirements of gain, bandwidth, polarization, and frequency can vary significantly and support a variety of antenna and package solutions.

This dissertation's primary research objective is to understand the range of frequencies and polarization states that can be achieved by only changing the patch antenna's dimensions and height while maintaining the same feed line and underlying RFIC.

This dissertation gives significant contributions in the antenna lid approach for AiP solutions, where a fixed feed-on-chip structure can be coupled to different antenna lids. These contributions are mentioned below:

Single fixed fed patch antenna lid

One of this dissertation's main contributions is that we discovered several essential characteristics of the PCPA antenna with a fixed feed. The analyses that we provided explains the behavior of the antenna's dimensions at different operating frequencies and polarization (linear or circular). It helps in understanding the design space and providing quick estimates of the antenna's dimension. Besides, these studies describe the coupling patch antenna's limitations to the fixed feed line.

The important observations from the PCPA's behavior are listed below:

- We discovered that the feed line underneath the antenna also contributes to radiation and caused the observed “critical frequency” behavior. As a result, the feed line design impacts the behavior of the fixed fed PCPA.
- The critical frequency behavior disappeared when we removed the feed line’s flared part and replaced the flared feed line with a straight feed line.
- The primary limitation in operating frequency is the antenna’s height, although this is not true for the straight feed.
- The second limitation is that CP cannot be generated over a wide range of frequencies. The circular radiation can be generated only operating frequencies around the fc. However, coupling to a straight feed line case, the CP can be created over a wide range of operating frequencies.

- The flared line’s FBW is wider than the straight line’s FBW. This is because of two reasons:
    - the total height of the antenna and the feed line for the flared feed line case is higher
    - The two resonance frequencies behavior exists when the PCPA antenna is coupled to the flared feed line. Thus, the frequency bandwidth is wide, especially at operating frequencies equal to fc and frequencies around it. This PCPA behavior is an advantage that can be used in the case of wide bandwidth applications.

With the straight feed line design, **we can generate circular or linear radiation over a wide range of operating frequencies by only changing the patch antenna's dimensions and mold height without making any changes in the design chip (RFIC).**

Fixed Fed Antenna Array

Moreover, we studied the uniform phased array with a fixed feed line at different operating frequencies. This analysis investigated the effect of the element space on the scanning performance of the phased array. The collected data sets provide design guidelines for selecting the fixed array lattice spacing according to the required scan angle, mutual coupling, and gain for a wide range of operating frequencies.

In conclusion, our generated analyses provide design guidelines for the antenna's dimensions at different polarization and operating frequencies without changing the RFIC chip, including the feed line. Moreover, our created analyses give the knowledge to allow the feed line dimensions to be optimized from the very beginning. Thus, the best feed line design and material are chosen and fixed for the RFIC chip.

7.2 Future Work

In this work, we studied LP and CP uniform linear phased array coupled to a fixed feed line, beside the CP and LP analysis for single patch antenna. However, this work was limited in several ways and suggested some future avenues for study.

7.2.1 Single Antenna

This dissertation gives base guidelines for antenna-lid coupled to a fixed feed line fabricated on a fixed RFIC chip. From the analyses that have been achieved in this work, some exciting research objectives can be investigated for future work. In chapters 3, 4, and 5, we discover an essential characteristic of PCPA coupled to a thin flared fixed feed line, the critical frequency $f_{c,}$ which is a breakpoint in the PCPA's behavior. At operating frequencies above or below this fc, the behavior of the PCPA changes. The main variations in the PCPA's behavior are:

- The critical frequency (f_c) is a breakpoint at which the antenna's optimal dimensions (L_{opt} and h_{opt}) change their behavior
  - The antenna's optimal height reaches a maximum at (f_c), and at frequencies above or below this critical frequency, the h_{opt} decreases.
  - The operating frequency is inversely proportional to the length of the antenna ($f_o \propto 1/L_{opt}$), at $f_o < f_c$. This is expected from the cavity and TL models analysis, as we mention in the introduction section. Although, the optimal length of the patch is almost constant at frequencies higher than the f_c.
- At a frequency higher or lower than $f_{c,}$ there are two resonant frequencies (f_{r1} and f_{r2}), but one of these frequencies has the lowest reflection coefficient (S_{11}< -25 dB).

But, at the f_c, only one resonant frequency is located. In other words, f_c is the frequency where the two resonant frequencies are overlapped.

- The FBW is wide at operating frequency equal to fc and around it. Wide FBW performance can be used for broadband antenna application

Some of these observed behaviors limit our objective goal in this dissertation, which is the antenna-lid approach. There are some applications like a broadband antenna that can use wide FWB when operating at the f_c or around it. As a result, determining the f_c location in the interested frequency range is essential. Thus, the newly opened research question is: **Can we find a model to predict the f_c at giving antenna-lid mold material?**

7.2.2 Array

We studied the linear H-plane uniform phased array, which is a one-D antenna array. The uniformed linear phased array consists of antennas aline in liner line with equal spacing, commonly controlled by a single-phase shifter. This dissertation studied the effect of element spacing (d) on mutual coupling and the grating lobe's existence in the visible region, which affects the SLL value. However, the CP phased array has another characteristic that we have to consider while studying CP radiation, AR beamwidth. We found out AR beamwidth narrows the scan angle range for CP phased array. AR beamwidth is also changing with the d value, but the AR beam width and d have complicated correlations. We observed that the AR beamwidth is wider at smaller d. Thus, we have a newly opened research question: **how does the d affect the AR beamwidth, or is there a correlation between the AR beamwidth and d?**

The linear phase arrays are simply arranged, but their beam steers only in a single plane. However, many applications need a 2D phased array such as radar, wireless communication, and imaging system where the beam steers in two planes. As a result, the newly opened question is:

How to structure the uniform planar phased array coupled with a fixed feed line? The challenge will be:

- **How to design the feed network structure for fixed fed planar phased array?**
- **Can various phased arrays operate at different frequencies and radiation types (linear or circular) coupled to the fixed feed network**

REFERENCES

[1] Y. A. Atesal, B. Cetinoneri, M. Chang, R. Alhalabi, and G. M. Rebeiz, “Millimeter-wave wafer-scale silicon BiCMOS power amplifiers using free-space power combining,” *IEEE Trans. Microw. Theory Tech.*, vol. 59, no. 4 PART 1, pp. 954–965, Apr. 2011, DOI: 10.1109/TMTT.2011.2108313.

[2] U. R. Pfeiffer *et al.*, “A chip-scale packaging technology for 60-GHz wireless chipsets,” *IEEE Trans. Microw. Theory Tech.*, vol. 54, no. 8, pp. 3387–3396, Aug. 2006, DOI: 10.1109/TMTT.2006.877832.

[3] U. Pfeiffer *et al.*, “A 60GHz radio chipset fully-integrated in a low-cost packaging technology,” in *Proceedings - Electronic Components and Technology Conference*, 2006, vol. 2006, pp. 1343–1346, DOI: 10.1109/ECTC.2006.1645830.

[4] T. Mitomo, N. Ono, H. Hoshino, Y. Yoshihara, O. Watanabe, and I. Seto, “A 77 GHz 90 nm CMOS transceiver for FMCW radar applications,” *IEEE J. Solid-State Circuits*, vol. 45, no. 4, pp. 928–937, Apr. 2010, DOI: 10.1109/JSSC.2010.2040234.

[5] E. Laskin *et al.*, “Nanoscale CMOS transceiver design in the 90-170-GHz range,” *IEEE Trans. Microw. Theory Tech.*, vol. 57, no. 12, pp. 3477–3490, Dec. 2009, DOI: 10.1109/TMTT.2009.2034071.

[6] K. Schmalz, W. Winkler, J. Borngräber, W. Debski, B. Heinemann, and J. C. Scheytt, “A subharmonic receiver in SiGe technology for 122 GHz sensor applications,” in *IEEE Journal of Solid-State Circuits*, Sep. 2010, vol. 45, no. 9, pp. 1644–1656, doi: 10.1109/JSSC.2010.2051474.

[7] J. W. May and G. M. Rebeiz, “Design and characterization of W-band SiGe RFICs for passive millimeter-wave imaging,” in *IEEE Transactions on Microwave Theory and*

Techniques, May 2010, vol. 58, no. 5 PART 2, pp. 1420–1430, DOI: 10.1109/TMTT.2010.2042857.

[8] A. Tomkins, P. Garcia, and S. P. Voinigescu, “A passive W-band imager in 65nm bulk CMOS,” 2009, DOI: 10.1109/csics.2009.5315696.

[9] L. Zhou, C. C. Wang, Z. Chen, and P. Heydari, “A W-band CMOS receiver chipset for millimeter-wave radiometer systems,” *IEEE J. Solid-State Circuits*, vol. 46, no. 2, pp. 378–391, Feb. 2011, DOI: 10.1109/JSSC.2010.2092995.

[10] L. Gilreath, V. Jain, H. C. Yao, L. Zheng, and P. Heydari, “A 94-GHz passive imaging receiver using a balanced LNA with embedded Dicke switch,” in *Digest of Papers - IEEE Radio Frequency Integrated Circuits Symposium*, 2010, pp. 79–82, DOI: 10.1109/RFIC.2010.5477289.

[11] S. F. Jilani and A. Alomainy, “Millimeter-wave conformal antenna array for 5G wireless applications,” in *2017 IEEE Antennas and Propagation Society International Symposium, Proceedings*, Oct. 2017, vol. 2017-January, pp. 1439–1440, DOI: 10.1109/APUSNCURSINRSM.2017.8072762.

[12] H. Lee, J. Bang, S. Lee, and J. Choi, “Phased Array Antenna with Whole-Metal-Cover for MM-Wave 5G Mobile Phone Applications,” Nov. 2018, DOI: 10.1109/iWEM.2018.8536690.

[13] S. F. Jilani, Q. H. Abbasi, and A. Alomainy, “Inkjet-Printed Millimetre-Wave PET-Based Flexible Antenna for 5G Wireless Applications,” Oct. 2018, DOI: 10.1109/IMWS-5G.2018.8484603.

[14] M. Stanley, Y. Huang, H. Wang, H. Zhou, A. Alieldin, and S. Joseph, “A novel mm-Wave phased array for 1800 coverage for 5G smartphone applications,” in *IET Conference*

Publications, 2018, vol. 2018, no. CP741, DOI: 10.1049/cp.2018.0802.

[15] F. Wang, L. Zhang, and X. Wu, "An UWB MM-wave phased array antenna for 5G handheld devices applications," in *2017 IEEE 6th Asia-Pacific Conference on Antennas and Propagation, APCAP 2017 - Proceeding*, Jul. 2018, pp. 1–3, DOI: 10.1109/APCAP.2017.8420727.

[16] L. Lianming *et al.*, "The path to 5G: mmWave aspects," DOI: 10.11959/j.issn.2096-1081.2016.032.

[17] D. M. Sheen, D. L. McMakin, and T. E. Hall, "Detection of explosives by millimeter-wave imaging," in *Counterterrorist Detection Techniques of Explosives*, Elsevier, 2007, pp. 237–277.

[18] D. G. Kam, D. Liu, A. Natarajan, S. Reynolds, and B. A. Floyd, "Low-Cost Antenna-in-Package Solutions for 60-GHz Phased-Array Systems," pp. 93–96, 2010.

[19] Y. P. Zhang, M. Sun, K. M. Chua, L. L. Wai, D. Liu, and B. P. Gaucher, "Antenna-in-package in LTCC for 60-GHz radio," in *Conference Proceedings - 2007 IEEE International Workshop on Antenna Technology: Small and Smart Antennas Metamaterials and Applications, iWAT 2007*, 2007, pp. 279–282, DOI: 10.1109/IWAT.2007.370129.

[20] Z. Popovic and A. Mortazawi, "Quasi-optical transmit/receive front ends," *IEEE Trans. Microw. Theory Tech.*, vol. 46, no. 11 PART 2, pp. 1964–1975, 1998, DOI: 10.1109/22.734521.

[21] Y. P. Zhang and D. Liu, "Antenna-on-chip and antenna-in-package solutions to highly integrated millimeter-wave devices for wireless communications," *IEEE Trans. Antennas Propag.*, vol. 57, no. 10 PART 1, pp. 2830–2841, 2009, DOI:

10.1109/TAP.2009.2029295.

[22] N. G. Alexopoulos, P. B. Katehi, and D. B. Rutledge, “Substrate Optimization for Integrated Circuit Antennas,” Mar. 2005, pp. 190–192, DOI: 10.1109/mwsym.1982.1130657.

[23] K. T. Chan *et al.*, “Integrated Antennas on Si With over 100 GHz Performance, Fabricated Using an Optimized Proton Implantation Process,” *IEEE Microw. Wirel. Components Lett.*, vol. 13, no. 11, pp. 487–489, Nov. 2003, DOI: 10.1109/LMWC.2003.817146.

[24] “Ph.D. Thesis by Erik Öjefors | Signals and Systems, Uppsala University.” http://www.signal.uu.se/Publications/abstracts/a061.html (accessed Mar. 07, 2021).

[25] Y. Hwang, Y. P. Zhang, and T. K. Lo, “Aperture-coupled microstrip antennas loaded with very high permittivity ceramics,” *Int. J. RF Microw. Comput. Eng.*, vol. 13, no. 2, pp. 154–160, Mar. 2003, DOI: 10.1002/mmce.10072.

[26] C. S. Wang, J. W. Huang, S. H. Wen, S. H. Yeh, and C. K. Wang, “A CMOS RF front-end with on-chip antenna for V-band broadband wireless communications,” in *ESSCIRC 2007 - Proceedings of the 33rd European Solid-State Circuits Conference*, 2007, pp. 143–146, DOI: 10.1109/ESSCIRC.2007.4430266.

[27] S. Shahramian, M. J. Holyoak, and Y. Baeyens, “A 16-Element W-Band Phased-Array Transceiver Chipset With Flip-Chip PCB Integrated Antennas for Multi-Gigabit Wireless Data Links,” *IEEE Trans. Microw. Theory Tech.*, vol. 66, no. 7, pp. 3389–3402, Jul. 2018, DOI: 10.1109/TMTT.2018.2822304.

[28] D. C. Nascimento and J. C. Da, “Design of Arrays of Linearly Polarized Patch Antennas on an FR4 Substrate: Design of a probe-fed electrically equivalent microstrip radiator,” *IEEE Antennas Propag. Mag.*, vol. 57, no. 4, pp. 12–22, Aug. 2015, DOI:

10.1109/MAP.2015.2453916.

[29] D. C. Nascimento, P. C. Ribeiro Filho, A. F. Tinoco-S, and J. C. D. S. Lacava, “Analysis and Design of Cavity-Backed Probe-Fed Hybrid Microstrip Antennas on FR4 Substrate,” *Int. J. Antennas Propag.*, vol. 2015, 2015, DOI: 10.1155/2015/206967.

[30] B. Rupakula, A. Nafe, S. Zihir, Y. Wang, T. W. Lin, and G. Rebeiz, “63.5-65.5-GHz Transmit/Receive Phased-Array Communication Link with 0.5-2 Gb/s at 100-800 m and ± 50° Scan Angles,” *IEEE Trans. Microw. Theory Tech.*, vol. 66, no. 9, pp. 4108–4120, Sep. 2018, DOI: 10.1109/TMTT.2018.2839185.

[31] D. G. Kam, D. Liu, A. Natarajan, S. Reynolds, and B. A. Floyd, “Low-cost antenna-in-package solutions for 60-GHz phased-array systems,” in *2010 IEEE 19th Conference on Electrical Performance of Electronic Packaging and Systems, EPEPS 2010*, 2010, pp. 93–96, DOI: 10.1109/EPEPS.2010.5642554.

[32] Y. P. Zhang, M. Sun, K. M. Chua, L. L. Wai, and L. Duixian, “Antenna-in-package design for wire-bond interconnection to highly integrated 60-GHz radios,” *IEEE Trans. Antennas Propag.*, vol. 57, no. 10 PART 1, pp. 2842–2852, 2009, DOI: 10.1109/TAP.2009.2029290.

[33] R. Vyas, A. Rida, S. Bhattacharya, and M. M. Tentzeris, “Liquid Crystal Polymer (LCP): The ultimate solution for low-cost RF flexible electronics and antennas,” *IEEE Antennas Propag. Soc. AP-S Int. Symp.*, no. 1, pp. 1729–1732, 2007, DOI: 10.1109/APS.2007.4395848.

[34] Y. P. Zhang, “Enrichment of package antenna approach with dual feeds, guard ring, and fences of vias,” *IEEE Trans. Adv. Package.*, vol. 32, no. 3, pp. 612–618, 2009, DOI: 10.1109/TADVP.2008.2001769.

[35] C. A. Balanis, *Antenna Theory Analysis, and Design*. Wiley.

[36] E. O. Hammerstad, “Equations for Microstrip Circuit Design,” Nov. 2007, pp. 268–272, DOI: 10.1109/euma.1975.332206.

[37] R. P. Parrikar and K. C. Gupta, “Multiport network model for CAD of electromagnetically coupled microstrip patch antennas,” *IEEE Trans. Antennas Propag.*, vol. 46, no. 4, pp. 475–483, 1998, DOI: 10.1109/8.664110.

[38] A. Benalla and K. C. Gupta, “Multiport Network Model and Transmission Characteristics of Two-Port Rectangular Microstrip Patch Antennas,” *IEEE Trans. Antennas Propag.*, vol. 36, no. 10, pp. 1337–1342, 1988, DOI: 10.1109/8.8618.

[39] K. Gupta, “Multiport network approach for modeling and analysis of microstrip patch antennas and arrays,” in *Handbook of Microstrip Antennas, Volume 1*, The Institution of Engineering and Technology, Michael Faraday House, Six Hills Way, Stevenage SG1 2AY, UK: IET, 2011, pp. 455–526.

[40] Q. Zhang, Y. Fukuoka, and T. Itoh, “Analysis of a Suspended Patch Antenna Excited by an Electromagnetically Coupled Inverted Microstrip Feed,” *IEEE Trans. Antennas Propag.*, vol. 33, no. 8, pp. 895–899, 1985, DOI: 10.1109/TAP.1985.1143670.

[41] D. Jaisson, “Simple model for computing the input impedance of a rectangular patch antenna with electromagnetic coupling,” vol. 152, no. 6, pp. 2–6, 2005, DOI: 10.1049/IP-map.

[42] D. C. Chang and J. X. Zheng, “Electromagnetic Modeling of Passive Circuit Elements in MMIC,” *IEEE Trans. Microw. Theory Tech.*, vol. 40, no. 9, pp. 1741–1747, 1992, DOI: 10.1109/22.156600.

[43] Y. T. Lo, D. Solomon, and W. F. Richards, “Theory and Experiment on Microstrip

Antennas," *IEEE Trans. Antennas Propag.*, vol. 27, no. 2, pp. 137–145, 1979, DOI: 10.1109/TAP.1979.1142057.

[44] D. M. Pozar and S. M. Voda, "A rigorous analysis of a micro stripline fed patch antenna," *IEEE Trans. Antennas Propag.*, vol. 35, no. 12, pp. 1343–1350, 1987, DOI: 10.1109/TAP.1987.1144041.

[45] M. Davidovitz and Y. T. Lo, "Rigorous Analysis of a Circular Patch Antenna Excited by a Microstrip Transmission Line," *IEEE Trans. Antennas Propag.*, vol. 37, no. 8, pp. 949–958, 1989, DOI: 10.1109/8.34130.

[46] W. Stutzman and G. Thiele, "Phased Array," in *Antenna Theory and Design*, Third., Wiley, pp. 314–320.

[47] E. Cohen, M. Ruberto, M. Cohen, O. Degani, S. Ravid, and D. Ritter, "A CMOS bidirectional 32-element phased-array transceiver at 60 GHz with LTCC antenna," *IEEE Trans. Microw. Theory Tech.*, vol. 61, no. 3, pp. 1359–1375, 2013, DOI: 10.1109/TMTT.2013.2243749.

[48] T. Zwick, A. Chandrasekhar, C. W. Baks, U. R. Pfeiffer, S. Brebels, and B. P. Gaucher, "Determination of the complex permittivity of packaging materials at millimeter-wave frequencies," *IEEE Trans. Microw. Theory Tech.*, vol. 54, no. 3, pp. 1001–1009, Mar. 2006, DOI: 10.1109/TMTT.2005.864140.

[49] X. Wang, J. Yao, X. Lu, and W. Lu, "Research on phase center stability of circularly polarized patch antennas for GPS applications," in *Proceedings of the 2015 IEEE 4th Asia-Pacific Conference on Antennas and Propagation, APCAP 2015*, Jan. 2016, pp. 362–365, DOI: 10.1109/APCAP.2015.7374405.

[50] K. K. So, H. Wong, K. M. Luk, and C. H. Chan, "Miniaturized Circularly Polarized Patch

Antenna with Low Back Radiation for GPS Satellite Communications," *IEEE Trans. Antennas Propag.*, vol. 63, no. 12, pp. 5934–5938, Dec. 2015, DOI: 10.1109/TAP.2015.2488000.

[51] A. Maria, V. Vishnupriya, K. K. A. John, and T. Mathew, "Dual-band circularly polarized truncated patch antenna for RFID reader and WiMAX applications," in *2nd International Conference on Electronics and Communication Systems, ICECS 2015*, Jun. 2015, pp. 684–687, DOI: 10.1109/ECS.2015.7124996.

[52] S. Arshad, A. Ahmad, Z. Sheikh, A. Rashid, and F. A. Tahir, "A compact dual-band circularly polarized asymmetric patch antenna for WLAN applications," in *Asia-Pacific Microwave Conference Proceedings, APMC*, Jun. 2017, pp. 952–955, DOI: 10.1109/APMC.2017.8251608.

[53] C. Te Liao, Y. F. Lin, C. H. Chen, S. Y. Kao, and H. M. Chen, "A novel aperture-coupled circularly polarized square-ring patch antenna for wireless communication systems," in *APCAP 2016 - 2016 IEEE 5th Asia-Pacific Conference on Antennas and Propagation, Conference Proceedings*, Feb. 2017, pp. 57–58, DOI: 10.1109/APCAP.2016.7843097.

[54] P. C. Sharma and K. C. Gupta, "Analysis and Optimized Design of Single Feed Circularly Polarized Microstrip Antennas," *IEEE Trans. Antennas Propag.*, vol. 31, no. 6, pp. 949–955, 1983, DOI: 10.1109/TAP.1983.1143162.

[55] T. Varum, A. Ramos, and J. N. Matos, "Planar microstrip series-fed array for 5G applications with beamforming capabilities," Oct. 2018, DOI: 10.1109/IMWS-5G.2018.8484697.